Czech Technical University in Prague
Faculty of Electrical Engineering
Department of Microelectronics

Readout electronics of particle detection systems

by

Zdenko Janoška

Doctoral Thesis

Programme: P 2612 Electrical Engineering and Information Technology
Branch of study: 2612V015 Electronics

Prague, December 2019

Supervisor:
doc. Ing. Jiří Jakovenko, Ph.D.
Department of Microelectronics
Faculty of Electrical Engineering
Czech Technical University in Prague
Technická 2
166 27 Prague 6
Czech Republic

Co-Supervisor:
prom. fyz. Václav Vrba, CSc.
Department of Physics
Faculty of Nuclear Sciences and Physical Engineering
Czech Technical University in Prague
Břehová 7
121 35 Prague 2
Czech Republic

Declaration

I hereby declare that I am the sole author of this dissertation and that I have not used any sources other than those listed in the bibliography and identified as references.

I agree with the utilization of the information presented in my thesis pursuant to Copyright Act 121/2000 Coll., Sec. 60.

.....
Zdenko Janoška

in Prague, 31st December 2019

Acknowledgment

I would like to thank my colleagues from Competence Centres Programme at CTU for their work and cooperation they have provided during the research. I also would like to thank my supervisor doc. Ing. Jiří Jakovenko, Ph.D. and co-supervisor prom. fyz. Václav Vrba, CSc., who advised me in the most crucial parts and have managed the project itself. Finally, I would like to thank my family and friends who have provided me a support during my work. Especially great thank to my wife and my 'kindergarten' for their great patience.

I also would like to thank my colleagues from UJP PRAHA a.s., VF a.s. and esc Aerospace for providing their technical resources during radiation measurements.

This research has been supported by the Technology Agency of the Czech Republic under Competence Centres Programme TE01020069 - Advanced Detection Systems of Ionising Radiation Project and CTU SGS grant No. SGS14/195/OHK3/3T/13.

Abstract

This study report deals with a particle detection system suited for the measurement of X–rays, beta radiation and ions including alpha particles which has been developed recently. The detection system consists of silicon n^+–on–p strip sensor connected to the PH32 front-end readout chip which can be used in the dose rate measurement, the basic spectroscopy, particle tracking or ion mass spectroscopy. The PH32 chip was manufactured using a commercial 180 nm CMOS process. It is able to measure the generated charge, the counting hits as well as the time of particle arrival from a silicon sensor in two operation modes. The high gain mode is able to measure generated charge in the range from about 3 ke^- to 40 ke^- for soft X-rays and beta radiation, the low gain mode in the range from about 300 ke^- to 4 Me^- for alpha particles. The electronic noise is about 1100 e^- for the chip calibration charge of 10 ke^- at high gain mode and 2300 ke^- for the chip calibration charge of 2 Me^- at low gain mode. The study is focused on overall chip description, its calibration and measurements of channels response to the injected charge including linearity, gain, channel uniformity, noise and dispersion. The energetic spectra of several radiation sources are presented together with the ability to measure the dose rate in the range of 8-orders of magnitude. The aim of the study includes description of the hardware limitations together with the issues arising throughout the ASIC readout chip development.

Keywords: Silicon radiation detector, Front-end readout chip, 180 nm, CMOS, Energy spectrum, Radiation dose, Particle tracking

Abstrakt

Táto práca sa venuje detekčným systémom častíc vhodných pre meranie röntgenového žiarenia, beta žiarenia a iónov vrátane alfa častíc. Tento detekčný systém pozostáva z kremíkového n^+–on–p stripového senzora, ktorý je pripojený na PH32 front-end vyčítavací čip s možnosťou použitia pri meraní radiačnej dávky, základnej spektroskopie, sledovaní dráhy častíc alebo iónovej hmotnostnej spektroskopii. PH32 čip bol vyrobený s použitím komerčného 180 nm CMOS procesu. Je schopný merať vygenerovaný náboj, počítať zrážky a merať čas príletu častice zo senzora v dvoch operačných módoch. Mód s vysokým zosilnením je schopný merať náboj v rozmedzí od 3 ke^- do 40 ke^- pre nízkoenergetické röntgenové žiarenie a beta radiáciu, mód s nízkym zosilením v rozmedzí od 300 ke^- do 4 Me^- pre meranie alfa častíc. Presnosť merania je okolo 1100 e^- pre čip kalibrovaný na náboj 10 ke^- v móde s vysokým zosilnením a 2300 e^- pre čip kalibrovaný na náboj 2 Me^-v móde s nízkym zosilením. Štúdia je zameraná na celkový opis čipu, jeho kalibráciu a merania odozvy kanálov na injektovaný náboj, ktoré zahŕňajú linearitu, zosilnenie, jednotnosť kanálov, šum a rozptyl. Sú prezentované energetické spektrá viacerých zdrojov žiarenia spolu s možnosťou merania radiačnej dávky v rozsahu osem rádov. Cieľom štúdie je taktiež popis hardvérových obmedzení spolu s problémami, ktoré vznikajú počas vývoja ASIC vyčítacieho čipu.

Kľúčové slová: Kremíkový detektor žiarenia, Front-end vyčítací čip, 180 nm, CMOS, Energetické spektrum, Radiačná dávka, Sledovanie dráhy častic

Contents

List of Acronyms

ASIC	Application–Specific Integrated Circuit
CERN	European Organization for Nuclear Research
CMOS	Complementary Metal–Oxide–Semiconductor
CSA	Charge Sensitive Amplifier
DDR SDRAM	Double Data Rate Synchronous Dynamic Random-Access Memory
DS	Differential Signaling
ENC	Equivalent Noise Charge
FDAC	Feedback DAC
FPGA	Field–Programmable Gate Array
FWHM	Full Width at Half Maximum
HV	High Voltage
LHC	Large Hadron Collider
LSI	Large Scale Integration
LVDS	Low–Voltage Differential Signaling
MAPS	Monolithic Active Pixel Sensor
MCU	Micro Controller Unit

MOSFET	Metal–Oxide–Semiconductor Field–Effect Transistor
MPW	Multi–Project Wafer service
OS	Operating system
OSC	Oscillator
PCB	Printed Circuit Board
SCL	Source–Coupled Logic (Current Mode Logic)
SEU	Single Event Upset
SOI	Silicon On Insulator
SPI	Serial Peripheral Interface
STSCL	Sub–Threshold Source Coupled Logic
TDAC	Threshold DAC
TID	Total Ionizing Dose
ToA	Time–of–Arrival
ToF	Time–of–Flight
ToT	Time–over–Threshold
TSV	Through Silicon Via
USB	Universal Serial Bus

List of Figures

List of Tables

Chapter 1

Introduction

The need for different types of particle detectors continuously grows. Many R&Ds in leading world research centers (Europe, USA, Japan) have developed detectors suited for the particle physics. The principal aim of particle experiments is the investigation of the most fundamental principles of the structure of matter and the entire Universe. For that sophisticated detection systems are used the techniques on the frontier edge of contemporary technologies. At the same time, the systems developed for the basic research may have numerous practical applications.

CERN (Conseil Européen pour la Recherche Nucléaire) is the most advanced laboratory in the world in the field of the particle physics. CERN is not only the major world laboratory in particle physics research but also the world leader in R&D for advanced experiments instrumentation. Concerning the semiconductor detectors it is the Medipix collaboration [1], which already passed several front-end readout chips (Medipix1, Medipix2, Timepix, etc.). It is successor of the RD19 project, which developed the first pixel detectors used in physics experiments.

The radiation hardness is a very important issue for many applications. To this topic the RD50 project is devoted [2], which is a successor of the RD49.

Accumulated expertise at CERN is projected in new detectors at the Large Hadron Collider (LHC), but also in numerous applications. CERN regularly organizes workshops on different topics: e.g. space dosimetry or medical applications.

The detection system described in this study has the intention to enhance the radiation hardness. This means it could be used for a longer time in the radiation ambient than the commercial detection systems used today. Another advantage should be the enhanced sensitivity of the detection system which is correlated to the lower dose rate needed to get the image of the object. This is especially important in order to reduce the X-ray dose delivered to the patient while taking an image of human body organs.

The work on the development of deep sub-micron integrated systems requires a front edge technology and was performed in the framework of international cooperation which means learning and taking inspiration from completely different teams and laboratories. There are very few such projects in eastern Europe and the research in this field in the Czech Republic is quite unique and novel. The cooperation with the leading research

institutes around the world facilitates the exchange of ideas and inspiration and greatly accelerates the R&D process.

Chapter 2

My contributions

This thesis is focused on the recently developed front-end readout chip named PH32. However, the research of the chip itself is just one part of the complex mechanism of the ionizing particles detection. First of all, here is a list of my most important contributions related to the read-out chip development, which are more discussed below:

- Development of a suitable particle counter with low consumption.
- Managing the information about the hit occupancy and synchronization of the measurement startup.
- Elimination of cutting off the first hit interference which leads to more precise energy measurement.
- Internal triggering system.
- Solving the cross-talk issues caused by triggering of the measurement.

The overall detection system consists of the sensor where the ionizing particle deposits its energy and afterward the energy is transfered to the front-end readout chip where it is processed. The information either in analogue or digital form is transferred through a daughter board to the mother PCB with post-processing hardware which can be accompanied by appropriate micro-controller or FPGA. This hardware can provide the information of ionizing radiation for end user or can be further sent and processed by personal computer. The detection module on the PH32 base can operate as stand-alone but also can provide a quantity of the advanced software utilities suited for calibration, detection and evaluation processes through the external operating system.

It is understandable that such complex detection system is developed by a group of closely cooperating people. The list of main contributors is stated in Acknowledgment.

I am the only author of complete digital part of all submitted PH32 chips. I am also co-author of some analog parts and parts required for the chip connectivity. The analog parts which are not my own contribution, are not described in detail and they are the part of this thesis only due to the complexity and clarity of the detection system. These

parts include: CSA, discriminator or proprietary differential driver. Last but not least, I organized the submissions of the PH32 chips with Europractice IC service.

The main scientific contributions can be categorized into these sections:

- The first versions of the PH32 readout chip contain the synchronous pseudo-counter which acts as a pseudo-random counter for data storing and it also enables serial read and write. This solution turned out to be not suitable due to relatively high power consumption which leads to a crosstalk into the analog front-end. This disadvantage have led to replacing the pseudo-random counter by an asynchronous counter which can also act as a shift register. The asynchronous counter gives an advantage with respect to the power consumption not only because of a lower average consumption but with these solution the current peaks are spread out in time compared to the pseudo-counter. The use of this topology is a novel approach in the field of the ionization particle detection.

- The chip contains the information of channel occupation or-ed from all channels. This inquiry is based on the analog signal from the CSA and the discriminator is not affected by any digital processing. The information about the hit occupancy is desirable also before measuring and afterwards, it can be used for hit activity measurement itself without any digital processing inside the chip. Further, the presence of this feature allows the synchronization of the measurement startup. This new approach allows to eliminate the chopping off the first hit occurrence arriving to the digital part for following processing.

- The next novel method is the information of the first accepted hit which is or-ed from all channels in the same way as above described feature. This information is derived besides from the analog part also from the shutter management required for the proper exposure timing. This feature, together with the above one is new approach in the triggering of the external hardware and allows to avoid cutting off the first hit interference which leads to more precise energy measurement.

- The presence of the above described features allow the synchronization of the measurement startup by an external hardware. Furthermore, this information may be also used for the internal triggering itself, where the internal shutter is waiting for no hit occurrence. This feature supports the outer hardware where no addition processing regarding the shutter occurrence is needed.

- The significant cross-talk issue is caused by the signal shutter during the triggering of the measurement. The cross-talk between the digital signal shutter and the output of the CSA is important at the beginning of the measurement mainly in energy measuring mode which can lead to detection of fake hit and to wrong evaluation of the hit energy. These issues led to a development of a new concept for the shutter triggering where the external digital signal shutter, needed for the triggering of the measurement, can be shifted in time and it can trigger the measurement with

an appropriate delay internally. The shutter shifter functionality together with the previous feature is a novel approach in the field of the radiation readout chips.

The development of the PH32 readout chip went through the different ASIC processes provided by several semiconductor foundries. This occurred mainly due to discontinued foundry process or by foundry existence issue. However, the PH32 front-end readout chip is at the end of the development and it is under ongoing engineering run right now.

Chapter 3

Worldwide R&D effort

The main driving force behind the research and development of radiation detectors were experiments in the particle physics. The CERN is playing major coordinating role worldwide. Several key R&D projects have been developed within the CERN: RD19, RD49, RD50, Medipix, RD53 [A.1], [A.2]. The first mentioned developed the first pixel detectors used in physics experiments. The next two projects have been devoted to radiation hardness research program. The Medipix research program is devoted to create a readout chips originally for particle tracking at the CERN LHC. This project demonstrated the great potential for the technology beyond the high-energy physics. The last mentioned RD53 project is devoted to creation of front-end readout chip for the future LHC upgrade. The results of these R&D projects have become the basis of the instrumentation of the large detection systems: ATLAS, CMS, ALICE, LHCb, which have broadened our knowledge of the structure of matter to the most elementary level over the last decade.

The ATLAS experiment, where I participate as a full member of research team, is one of two general-purpose detectors at the LHC (CMS experiment is the second one). The ATLAS detector comprises several concentric cylinders around the interaction point where the proton beams from the LHC collide. The detector which is most close to the interaction point is called *inner detector*. The major aim of the inner detector is to track the particle and to evaluate the particle momentum due to curving the particle by magnetic field that is surrounding the entire inner detector. The inner detector consists of three subdetectors. The innermost part of the inner detector is called *pixel detector* which is a typical representative of hybrid pixel detectors. These detectors consist of read-out electronics and outer detector connected together by wire-bonds or bump-bonds. The read-out electronics, the innermost layer of the pixel detector, is the main subject of this study.

The ATLAS pixel detector (Fig. 3.1) contains three concentric layers and two end-caps with three discs each. All layers are composed of individual modules (Fig. 3.2) which communicate with data acquisition system separately. Our point of interest is placed right on this module.

The pixel detector contains 1,744 modules which consist of sixteen FE–I3 front-end readout chips [4] connected to the silicon sensor by bump–bonding. The silicon n^+–on–n sensor with 250 μm thickness has 47,232 pixel implants that are arranged in 144 columns

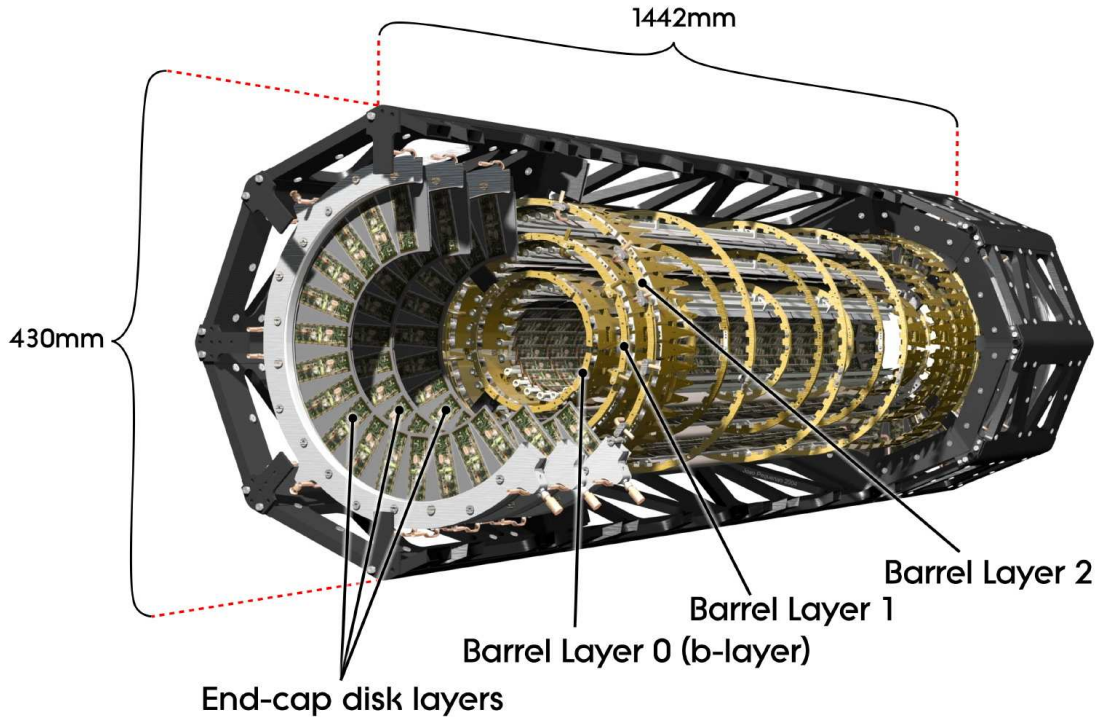

Figure 3.1: Schematic drawing of the active region of the ATLAS pixel detector. The detector consists of three concentric barrel layers and two end-caps [3].

and 328 rows with a pixel pitch corresponding to 400×50 µm^2. The total amount of sensitive area makes ≈ 1.7 m^2 with over 80 million readout channels.

The last generation of the front-end electronics supposed to be used in ATLAS pixel detector is FE–I4 readout chip [A.5] and FE–I4B version for *b–layer* [A.6] fabricated in 130 nm CMOS technology, with smaller pixel size and addition features as the Time–over–Threshold (ToT) and the Time–of–Arrival (ToA) measurements together with higher radiation tolerant compared to its predecessor.

The ATLAS pixel detector is a typical example of State-of-the-art in the particle physics in the presence. It is also worth to mention that the ATLAS experiment together with CMS experiment led to the award of the Nobel Prize in physics (2013) to Francois Englert and Peter Higgs for their theoretical prediction of the mechanism.

The article [5] summarizes the contemporary front-end electronics used in the field of particle detection together with the requirements which derive from the LHC operation:

- Good spatial resolution (in the micrometer range) to distinguish 2 closely separated tracks.

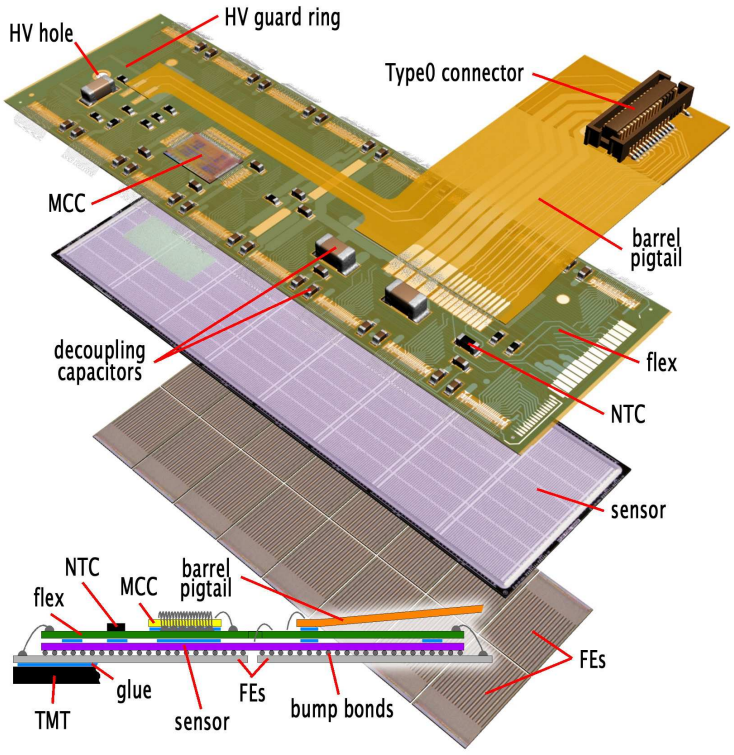

Figure 3.2: The elements of a pixel barrel module. Each module contains sixteen front-end FE-I4 chips, one silicon sensor and flexible printed circuit to route signals and power together with module control chip (MCC) [3].

- The ability to assign hits to single bunch crossings (which are separated by 25 ns).
- Low effective mass in order to not disturb particle identification in the outer detectors.
- Low power consumption to minimize the cooling infrastructure.
- High radiation tolerance for the detectors and readout electronics.
- Short readout time to cope with high event rates.

The development of the readout electronics used for the particle accelerator lead to research in other fields such as medical imaging applications, X-ray scanning, national security and others. One of the leading research projects is Medipix3 ASIC [6] together with the related project Timepix3 [6] manufactured using a commercial 130 nm CMOS process. The current stage of the development is the result of long term development of their predecessors, namely Medipix2 [7] and Timepix [8] manufactured using a 250 nm CMOS process. The Medipix2 chip is a pixel detector readout chip working in single photon counting mode for positive or negative input charge signals. The basic properties of the Medipix2 can be described as follows:

- Square pixel of the size of 55 μm
- Sensitive to positive or negative input charge
- Pixel by pixel detector leakage current compensation

- Window in energy
- 14–bit counter per pixel contains 1-bit overflow control
- Count rates of 1 MHz/pixel (0.33 GHz/mm^2)
- 256 × 256 pixels
- 3-side but-table
- serial or parallel I/O

The Medipix2 can run in the *Hit counting* mode only while with the Timepix (the follower of Medipix2) it is possible to measure the energy of particle by the ToT method as well as the time of particle arrival by the ToA method besides the *Hit counting* mode with the time resolution to around 12.5 ns according the sampling rate [A.11]. The Fig. 3.3 represents the scan done by the quad Medipix2 read-out chip connected to 300 µm silicon sensor.

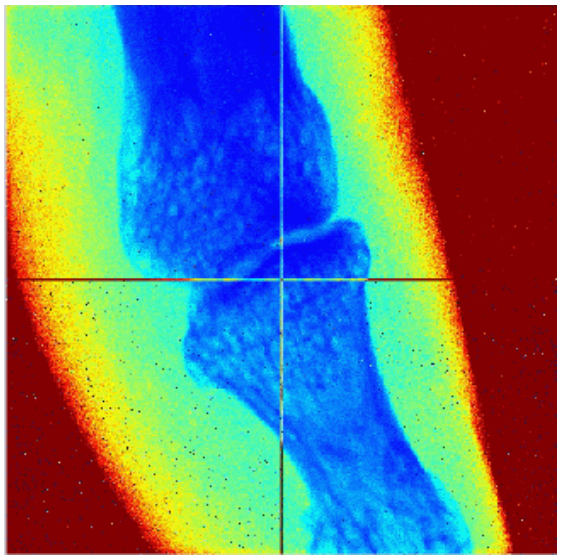

Figure 3.3: Image of a human finger obtained by the quad Medipix2 and 300 µm silicon sensor. W–tube, 35–kV, 2.5 mm Al equivalent prefiltering

For the spectroscopic X–ray imaging at relatively high X–ray fluxes the readout chip Medipix3 (and its Timepix3 variant) has been developed. The main feature of the Medipix3 is the reduction of the charge sharing which originated with very small 55 μm pixel pitch. The Timepix3 chip is able to send data simultaneously for the post-processing together with higher time resolution than its predecessor.

The both chips are also Through Silicon Via (TSV) proven. This feature allows the replacement of the wire-bond pads by the TSV processing and therefore the dead area can be significantly lowered. This advantage may lead to creation of a large detector surface. The Medipix3 and Timepix3 represent the most recent stage of research in the particle detection field.

However, the fact that these solutions are relatively expensive and complicated to use there is an effort for research of the simpler solution together with the same complexity as the chips mentioned above.

Chapter 4

Overview of our approach

In the previous section the most recent front–end readout chips have been described. The development of the FE-I3 read–out chip used in the current ATLAS pixel detector together with the FE-I4 chip which is supposed to be used in the detector upgrade [A.4], [A.5] as well as many others related projects [A.6], [A.7]. [A.3] led to development of new ASICs supposed to be used in the medical imaging applications. Special effort is mainly for the reduction of the X–ray dose delivered to the patient, the most effective X–ray imaging, X–ray inspection, national security and many others. One of the leader between chips developed recently is Medipix3 read–out chip and related project Timepix3 already briefly described earlier. I have had a great opportunity to work on the most recent projects. I have participated at the characterizations of the mentioned readout chips and sensors, at the software development related to the data acquisition system, at he hardware and firmware development of the readout boards and others.

All these ASICs have a large application potential. However these detection systems have enormous complexity that leads to the necessity of complicated hardware with FPGA, DDR memory, Ethernet and others at additional boards together with a high data flow. The concept of hybrid pixel detector used for such detector systems requires complicated bump–bonding for connectivity of the sensor and the readout chip what is technologically demanding and financially non-negligible costly operation. It should be mentioned that bump–bonds with 55 μm pitch is not a common process in the present. The last but not least, the reparation of bump–bond connectivity leads to the strict processes which can cause the degradation of the ASIC manufactured in submicron technology.

The PH32 front-end readout chip [A.9, A.10] presented in this study is designed for connection with the strip silicon sensor. It brings simplicity together with a low price due to relatively simple readout system consisting of the PH32 CMOS readout chip connected to 32 channels of the silicon sensor by more common and low cost wire bonding connectivity technique. The information as number of particles coming across the channel as well as the deposited charge collection or time of particle arrival can be read by very simple additional hardware due to low amount of channels. In generally the simple MCU can be used and together with the low power concept the whole detection system is suitable for the mobile and even for the space applications (high radiation tolerance). In the present the

communication with the PH32 chip is made by SURE (Simple USB Readout Equipment) data acquisition readout card which allows configuration as well as transmission of the measured data from the chip via the USB interface. The hardware and the software are multi–platform that allows to use the entire system at any OS and any hardware platform.

The PH32 chip with this setup has a significantly higher radiation tolerance than the common devices for commercial applications and therefore the PH32 chip is perfectly suited for the dose rate measurement and the basic spectroscopy. This higher radiation tolerance is caused mainly due to appropriate CMOS processing technology. However, the higher integration manufacturing process does not have to lead to the higher radiation tolerant.

With respect to the price of the chip production and the value obtained by higher integration the commercial 150 nm CMOS manufacturing technology was used [A.8]. However, due to complications during the manufacturing caused by the foundry bankruptcy, the chip had to be redesigned into other technology offered by a competitor foundry and subsequently the commercial 180 nm CMOS manufacturing technology has been chosen for following submissions.

The most recent version of the PH32 readout chip is the PH32v7. However, this study includes description of the most produced versions of the chip. It is focused on their differences and novel approaches which were made mainly in the digital part due to certain malfunctions or lower performance compared to the prediction. The basic architecture of the entire system is shown in Fig. 4.1 for silicon sensor with 32 identical channels while the Fig. 4.2 describes the detection system with two silicon sensors with sixteen wide and narrow channels.

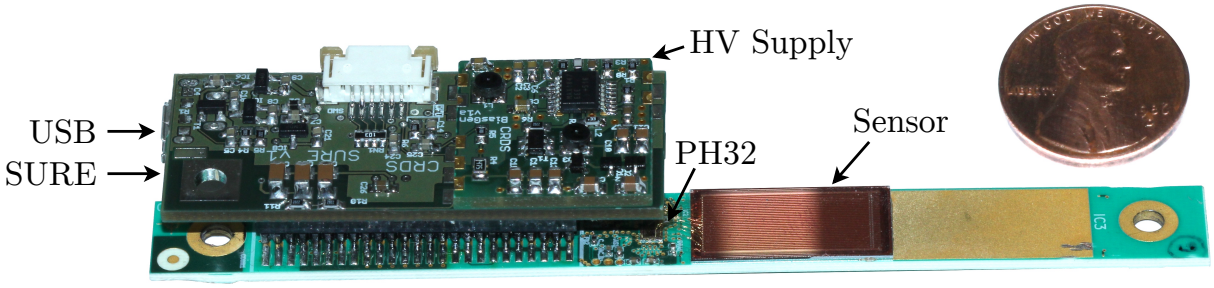

Figure 4.1: Detection module based on the PH32 chip contains silicon sensor with 32 channels, HV power supply and SURE (Simple USB Readout Equipment) data acquisition readout card.

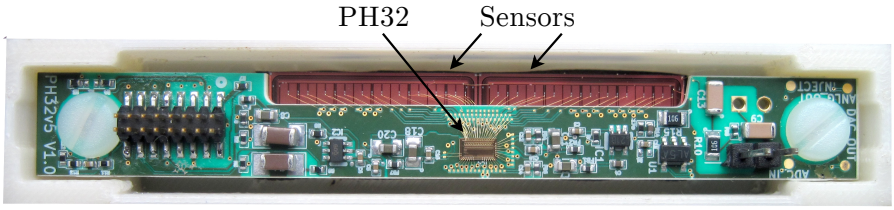

Figure 4.2: Detection module based on the PH32 chip contains two silicon sensors with sixteen wide and narrow channels.

Chapter 5

Detection principles

The principle of all detection systems is to transfer the monitored phenomena to the electrical signals, which can be electronically processed and evaluated by software. The concrete implementation of this concept is determined by the physical properties of the phenomenon being monitored and the nature of the particular application.

In the case of the radiation detection formed by charged particles, the electrical signal is generated by the ionization charge released by the passage of the particle through the sensor material. In the case of neutral particle detection, a suitable converter is used in which the neutral particle generates a charged particle which is then detected by appropriate sensor. In the optimal case, the detector sensor is also a converter.

Ionizing radiation refers to atomic and nuclear processes. Basic division into two groups as *charged particle radiation* and *uncharged radiation* can be further categorized into four subgroups as described below:

Charged particle radiation		Uncharged radiation
Fast electrons	$\Leftarrow$	Electromagnetic radiation
Heavy charged particles	$\Leftarrow$	Neutrons

The charged particles on the left side interact through the coulomb force with the electrons of the atoms contained in the medium. This group contains *fast electrons* which are produced through nuclear reaction known as *beta radiation* (electrons or positrons) or high energetic electrons produced by other processes. To the charged particle radiation belong also *heavy charged particles* which have mass higher or equal to one atomic mass. This charged particle group involves *protons*, *alpha particles*, product of *nuclear fission* or products of many other nuclear reactions. Due to the interaction of the charged particles with the matter through coulomb force the characteristic distance the particles can interact with the matter is much less than the uncharged particles and is in the range from 10^{-4}m to 10^{-2}m for fast electrons according their energy [9] and around 10^{-5}m for heavy charged particles [10].

The second group of uncharged radiation consists of *electromagnetic radiation* and *neutrons*. The electromagnetic radiation can be divided into *X-rays* which is response of rearrangement of electron shells of excited atoms and *gamma rays* that comes from changes

inside nuclei. The neutrons are products of many types of nuclear reactions and can be divided further into *slow neutrons* and *fast neutrons* (described later). In contrast to the charged particles the uncharged radiation does not interact through coulomb force and therefore its penetration ability to travel through the matter is much higher and is around 10^{-1}m.

To detect the uncharged radiation the radiation energy must be transferred to the electrons or nuclei of atoms to perform further nuclear reactions. This transfer is illustrated by arrows in the table above and means that the X-rays and the gamma rays can transfer their energy to the electrons. These electrons are called *secondary electrons* and are similar to the fast electrons related to the beta decay. Similarly the neutrons can transfer their energy for creation of heavy charged particles with energy that can be measured by detector. Due to the high penetration ability of neutrons and high energy gamma rays it is very hard to manage the energy measurement of this kind of radiation by conventional semiconductor detectors and therefore other detector concepts are in use [11].

5.1 Passage of charged particles through matter

From the standpoint of the sensor activity, except for very specific cases, electromagnetic interactions with sensor material are used to detect charged particles. This leads to the ionization of atoms and the release of the charge along the path of the penetrating particles.

5.1.1 Interaction of fast electrons

5.1.1.1 Beta radiation

The most probable source of fast electrons is beta radiation. Beta decay can produce either electrons which is known as *beta minus* (β^-) emission or less common positrons by *beta plus* (β^+) emission.

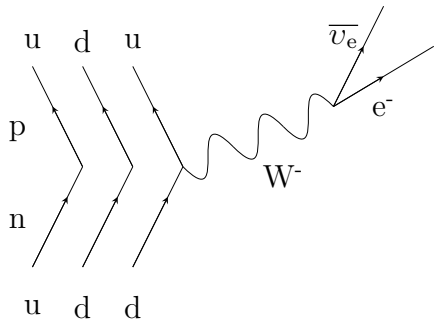

Figure 5.1: Beta minus emission. The weak interaction converts down quark to an up quark changing the neutron to a proton. Beta emission is accompanied by the emission of an electron anti-neutrino ($\overline{\upsilon_e}$) which shares the momentum and energy of the decay.

In beta minus emission (Fig. 5.1) down quark is converted to an up quark by weak interaction and atomic nucleus is converted into a atomic nucleus with higher atomic

number. This conversion is accompanied by emission of an electron (β^-) and an electron antineutrino ($\overline{\upsilon_e}$) which shares the momentum and energy of the decay and is written schematically as

$$ {}^{A}_{Z}X \rightarrow {}_{Z+1}{}^{A}Y + \beta^- + \overline{\upsilon_e} \tag{5.1} $$

where X and Y are initial and final nuclear elements, A and Z are the mass and the atomic number of the decaying nucleus.

In contrast in beta plus emission the weak interaction converts a proton to a neutron inside atomic nucleus and the emitted positron is accompanied by a neutrino. Positrons are emitted with the same kind of energy spectrum as electrons in negative beta decay because of the emission of the neutrino. β^+ decay is written schematically as:

$$ {}^{A}_{Z}X \rightarrow {}_{Z-1}{}^{A}Y + \beta^+ + \upsilon_e \tag{5.2} $$

Each beta decay is characterized by a specific decay of energy called Q-value. This energy is shared between the beta particle and a neutrino or an antineutrino according to the type of the beta decay. Beta particle can carry the energy varying from zero to the maximum Q-value. This assumption is for the beta decay where the initial as well as the final nucleus is in the ground state. If the product nucleus is in the exited state, the de-excitation process has to come accompanied by gamma rays which is common for most beta decays. This radiation is produced during the change in nuclear charge when the beta particle is created and leaves the nucleus [12]. This specific radiation has been called internal bremsstrahlung in contradistinction to the external bremsstrahlung which is electromagnetic radiation produced by the deceleration of an electron by an atomic nucleus. The example of beta radiation energy distribution is shown in Fig. 5.2 [13]. Here the ^{210}Bi decays into ^{210}Po through β^- decay ($\%\beta^- = 99.99$) with the maximum energy (Q-value) 1.16 MeV [14].

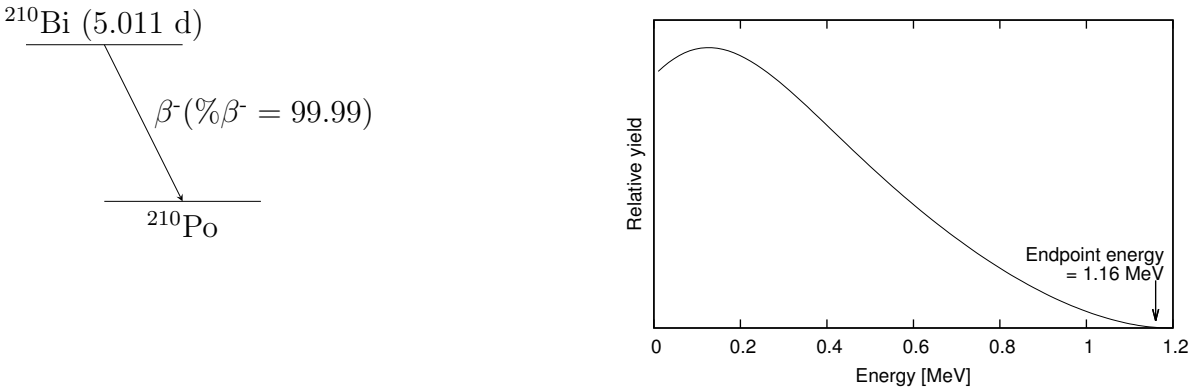

Figure 5.2: The decay scheme and beta radiation energy distribution of ^{210}Bi [13]. ^{210}Bi decays into ^{210}Po through β^- decay ($\%\beta^- = 99.99$) with the maximum energy Q^-=1.16 MeV [14]

5.1.1.2 Internal conversion and auger electrons

For the most beta decays the product nucleus is in the excited state (metastable nuclear isomer) and its energy is transferred to gamma rays. This de-excitation process is sometimes inhibited and the energy is transferred to the internal conversion process where the excitation energy is transferred directly into one of the orbital electrons of the atom with its energy given by

$$E_{e^-} = E_{ex} - E_b \tag{5.3}$$

where E_{ex} is the excitation energy and E_b is binding energy in the original shell. The excitation energy can be transferred into the electron in different shells and therefore the energy spectrum of electrons excited by internal conversion process can contain more groups of electrons with different energies. More excitation states with different excitation energies also contribute to more complicated energy spectrum.

For various measurements with detection system based on PH32 chip the Cesium-137 has been used. This is the example of gamma isotope which decays through β^- decay directly into ground state of isotope Barium-137 ($\%\beta^- = 5.6$) and into a metastable nuclear isomer of Barium-137m through β^- decay ($\%\beta^- = 94.4$) which decays through gamma rays into ground state of Barium-137 with energy 662 keV [15]. Excited Barium-137m in some cases can produce conversion electrons with energy 624 keV resp. 656 keV for K-shell resp. L-shell conversion. The decay scheme of Cesium-137 is shown in Fig. 5.3.

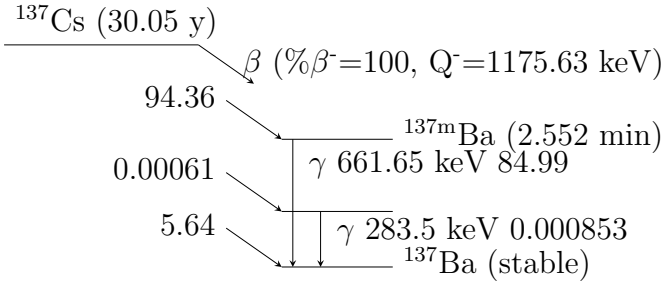

Figure 5.3: The decay scheme of ^{137}Cs.

The nucleus with high number of protons can absorb an inner atomic electron (from the K or L electron shell). This process is called *Electron capture* and is changing a nuclear proton to a neutron and simultaneously emitting an electron neutrino:

$$^A_Z X + e^- \rightarrow {}^A_{Z-1} Y + \upsilon_e \tag{5.4}$$

During this process a vacancy appeared in a electron shell which is then filled by another electron from upper electron shell and characteristic X-ray photon is emitted. This energy can by transferred to the outer electron and then ejected the electron from the atom. This is *Auger electron* and has energy according equation 5.3. Basically it is the same process as internal conversion but excitation energy originates in the atom instead of nucleus itself. Auger electrons are common mainly in low-Z elements where the binding energies are small.

The internal conversion is process which can lead to producing of conversion electrons (and Auger electrons) that can have under specific condition almost monoenergetic spectrum and therefore can be used as source for calibration of detection system.

5.1.1.3 Specific energy loss

The specific energy loss (also called *Linear stopping power*) for charged particles is defined as differential energy loss by the specific differential path length of specific absorption material:

$$S = -\frac{\partial E}{\partial x} \tag{5.5}$$

The main interactions of fast electrons with matter are ionization and excitation. The specific energy loss of collision losses is derived by Bethe

$$-\left(\frac{\partial E}{\partial x}\right)_c = \frac{2\pi e^4 NZ}{m_0\nu^2}\left(\ln\frac{m_0\nu^2 E}{2I^2\left(1-\beta^2\right)} - \left(\ln 2\right)\left(2\sqrt{1-\beta^2}-1+\beta^2\right) + \left(1-\beta^2\right) + \frac{1}{8}\left(1-\sqrt{1-\beta^2}\right)^2\right) \tag{5.6}$$

where ν is the velocity, N and Z are the number density and atomic number of the absorber atom, m_0 is the electron rest mass, e is the electron charge, I represents mean excitation energy and $\beta \equiv \nu/c$.

For the fast charged particles the assumption $\nu \ll c$ is no longer valid and therefore the energy by interactions with the Coulomb field of the nuclei of the traversed medium has to be taken in account. In this case the energy may be lost by radiative processes which are form of *Bremsstrahlung*. The specific energy loss through radiative process is:

$$-\left(\frac{\partial E}{\partial x}\right)_r = \frac{NEZ\left(Z+1\right)e^4}{137 m_0^2 c^4}\left(4\ln\frac{2E}{m_0^2} - \frac{4}{3}\right) \tag{5.7}$$

One can observe that Bremsstrahlung can be significant only for fast electrons and not for heavy particles due to m_0^2 factor in eq. 5.7. The factors E and Z^2 also show that the Bremsstrahlung is significant only for high electron energies and for absorber material of large atomic number.

The total specific energy loss power for fast electrons is the sum of energy loss due to ionization and excitation processes (collision losses) and energy loss due to radiative processes:

$$\frac{\partial E}{\partial x} = \left(\frac{\partial E}{\partial x}\right)_c + \left(\frac{\partial E}{\partial x}\right)_r \tag{5.8}$$

The radiation losses are small fraction of total specific energy loss due to relatively small electron energy obtained through beta decay (few MeV) and begin to be significant only for high-Z materials.

5.1.1.4 Absorption

The scattering of electrons is significant immediately after electrons entrance a detector and therefore even small absorber thickness causes the energy loss of such electrons. Hence

the electrons lose their energy gradually from the detector entrance to the high thickness of absorber where electrons lose all energy to zero.

Fig. 5.4 shows range-energy plot for monoenergetic electrons in silicon. One can observe that for silicon density ρ_{Si}=2.33 g/cm^2 range for high energy electrons (10s MeV) is around 10^{-2}m [16]. The silicon sensor used with the front–end chip described in this study is 525 m thick and therefore usage of other types of sensor with higher atomic number (e.g. CdTe sensor) should be considered for measurement of fast electrons with higher energies. However beta particles in compare with the mono-energetic electrons have continuous energy distribution with significant part of lower energies and therefore the energy is rapidly absorbed in the thin part of the silicon detector.

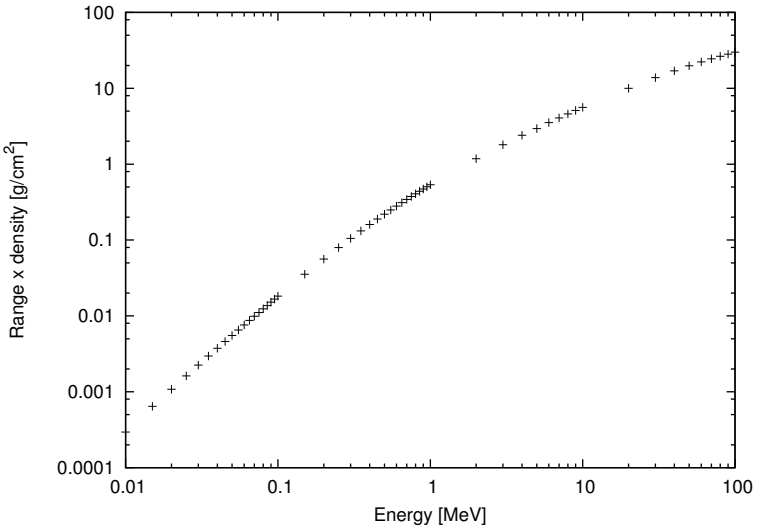

Figure 5.4: Range-energy plot for electrons in silicon. (Data from Ref. [16].)

For materials with high atomic number *Backscattering* process became significant also. If electrons lead to the detector surface under low angle the absorber may undergo notable deflection of electrons. This process is even more significant for low energy electrons and in some cases Backscattering may play even dominant part (e.g. fraction η=0.5 of normally incident electrons with energy to around 100 keV that are reflected by golden absorber [17]).

Most of interactions valid for electrons are valid for positrons as well. However is there one exception in that annihilation of positron with atomic electron when two photons with energy 0.511 MeV are emitted. These photons have great penetration ability and therefore deposition of energy can be in long distance from initial positron track.

5.1.2 Interaction of heavy charged particles

Heavy nuclei are energetically unstable and are subjects to fission nucleus through *Alpha particles* or *Spontaneous fission* to heavy charged particles with mass greater than that of the alpha particles which is however less common.

The alpha particle is a nucleus of the element helium (^{4}He nucleus) which has extremely high binding energy and great mass compared with the beta particle and therefore alpha particle is very stable and with its charge has a very short penetration range (around 10^{-5}m in Silicon [10]). The alpha decay is written schematically as

$$ {}^{A}_{Z}X \rightarrow {}^{A-4}_{Z-2}Y + {}^{4}_{2}\alpha \tag{5.9} $$

where X and Y are the initial and the final nuclear elements, A and Z are the mass and the atomic number of the decaying nucleus.

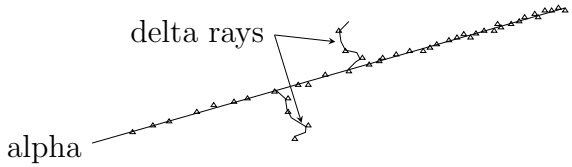

Figure 5.5: Alpha particle decreases its velocity continuously through interactions with orbital electrons of absorber atom until the particle is stopped. Delta rays produced by electrons with sufficient kinetic energy to create further ions are also shown.

The alpha particle that escapes from the heavy nucleus has to overcome high energy barrier. This energy is much higher than the energy of the emitted alpha particle but there is finite probability that the alpha particle could penetrate the wall by quantum mechanical tunneling. This process is called *Barrier penetration* and is responsible for various half-life of radioactive sources which is in range from days to thousand of years. The correlation between the half-life and the energy of the alpha particle is very strong. The energy is in the range from around 4 MeV with the longest half-life to around 6 MeV with the shortest half-life. The radioactive sources with the energy of the alpha particle beyond this range are out of the interest for detection systems due to their very small penetration probability or on the other hand very short half-life below few days. An example of standard alpha source used for calibration of detector systems (also for detector module based on PH32 readout chip shown in section 9.1) is ^{241}Am with energy spectrum shown in Fig. 5.6.

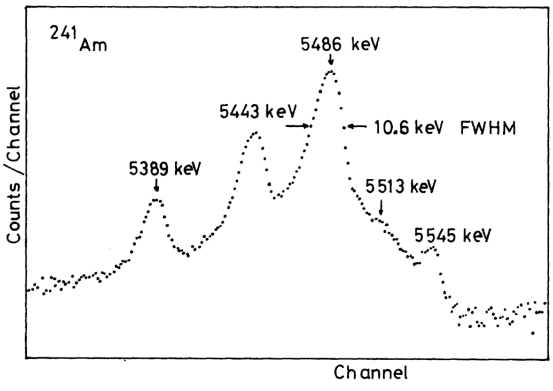

Figure 5.6: Spectrum of a ^{241}Am alpha-particle source (log scale) measured with a silicon detector (25 mm^2 area, 300 m thick) at room temperature. Resolution at 5.486 MeV is 10.6 keV (FWHM) [18].

The nuclei may undergo fission by another process called Spontaneous fission as mentioned earlier when are created heavy charge particles with higher mass than mass of alpha particles. This process is however less probable than emission of alpha particles and very often is accompanied by emission of neutrons and gamma rays.

5.1.2.1 Specific energy loss and range

The alpha particle interact with the matter mainly through coulomb forces between positively charged alpha particle and negative orbital electron of absorber atom. This coulomb force will cause either excitation or ionization of absorber atom. The energy which is transferred to the electron is small fraction of energy belongs to the alpha particle and maximum fraction of energy which can be transferred from charged particle to the electron is $4Em_0/m$ where E and m is kinetic energy and mass of charged particle and m_0 is electron mass. Because of electron mass is much smaller than mass of charged particle the heavy charged particles must lose their energy in many encounters along their path and therefore the collision track is except at very end almost straight (Fig. 5.5). In some cases (e.g. short distance of absorber material to the source and very high kinetic energy) the charged particle can transfer such amount of its energy to the orbital electron that electron itself can ionize other absorber atoms and create *Delta rays*. These delta rays are formed close to the primary track of charged particle due to smaller range than range of charged particle. However majority of energy loss of charged particle is via these delta rays. If such delta rays occur near the surface the electrons may escape from the absorber and produce *Secondary electron emission*.

The specific energy loss is defined similarly as for fast electron (Eq. 5.5) as differential energy loss by the specific differential path length of specific absorption material. This energy loss increases as the particle velocity decreases. This phenomenon is described in Fig. 5.5 when the alpha particle ionizes most absorber atoms at very end of its track. This behavior is derived from Bethe formula [10] and is written as

$$-\frac{\partial E}{\partial x} = \frac{4\pi e^4 z^2 NZ}{m_0 \nu^2}\left(\ln\frac{2m_0\nu^2}{I} - \ln\left(1-\frac{\nu^2}{c^2}\right) - \frac{\nu^2}{c^2}\right) \tag{5.10}$$

where ν and z are the velocity and charge of the primary charged particle, N and Z are the number density and atomic number of the absorber atom, m_0 is the electron rest mass, e is the electron charge, I represents mean excitation and ionization potential of the absorber atom. From Eq. 5.10 one can observe that due to factor z^2 the specific energy loss is greater for particle with the greatest charge. Also the energy loss is higher for high atomic number, high-density materials due to factors N and Z. The velocity ν in denominator describe the earlier mentioned fact that energy loss is increasing with decreasing of velocity. As a result of calculation the specific energy loss for different heavy charged particles in silicon (used with PH32 readout chip) is shown in Fig. 5.7.

The heavy charged particles lose their energy as predicted Eq. 5.10 as they penetrate through absorber while they have enough energy to pass the medium without electron pickup. Almost at the end of the track the charged particles lose their charge by electron pickup and therefore specific energy loss is dramatically reducing. This behavior is illustrated in Fig. 5.8 for alpha particle and proton with energy of several MeV which is known as *Bragg curve*. On other hand this behavior is not valid for very heavy fission fragments where these charged fragments pick up electrons at the very beginning already.

Fig. 5.9 illustrates the particle range. The charged particles pass the absorber while

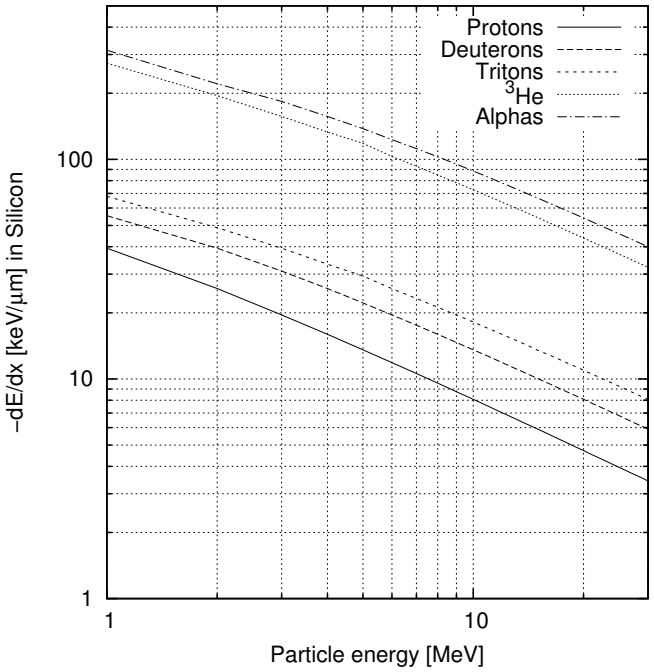

Figure 5.7: The specific energy loss calculated for different heavy charged particles in silicon. (Data from Ref. [10].)

Figure 5.8: The Bragg curve for alpha particle and proton with energy of several MeV. The specific energy loss is increasing as particles are penetrating into the absorber. Near the end of track particles lose the charge by electron picking and specific energy loss drops abruptly. Charged particle with greater number of nuclear protons begin to pick up electron earlier.

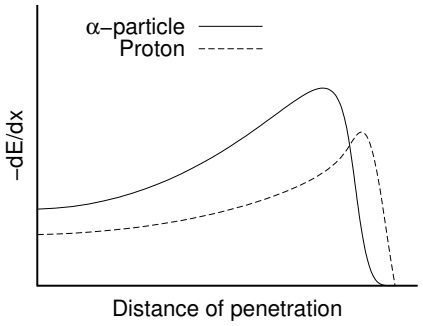

their energy is losing. Without electromagnetic field the particle path is quite straight through all absorber thickness. The number of particles is unchanged while they have enough of energy to travel without picking up the electrons. Near the end of particle track the charge of particle is reduced by electron pickup and number of particles passing through absorber thickness are reducing rapidly. How abrupt is this particle number change represents the *Range straggling*. The range can be defined as *Mean range* R_m when the number of passing particles is exactly one-half of initial number of particles entering the absorber.

In the case of energy measurement of charged particles the detector must have an active thickness greater then mean range of measured particle to allow deposition of full

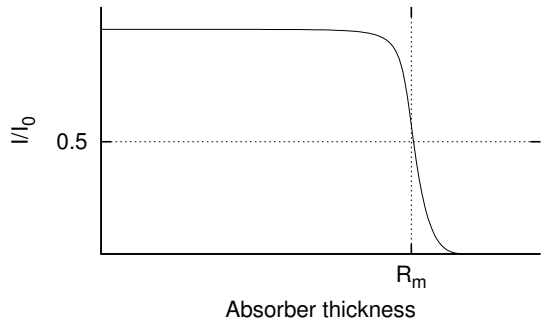

Figure 5.9: The alpha particles penetrate through absorber until they lose the charge by electron pickup. I_0 represents the initial number of alpha particles, I represents the number of alpha particles through an absorber thickness. The mean range R_m represents the distance when the number of alpha particles is exactly one-half of initial amount.

incident particle energy to the absorber. From Fig. 5.10 one can see that the silicon sensor with thickness 525 m (used with PH32 readout chip) can be used for full incident energy measurement of alpha particles with energy up to around 40 MeV or protons with energy up to around 10 MeV.

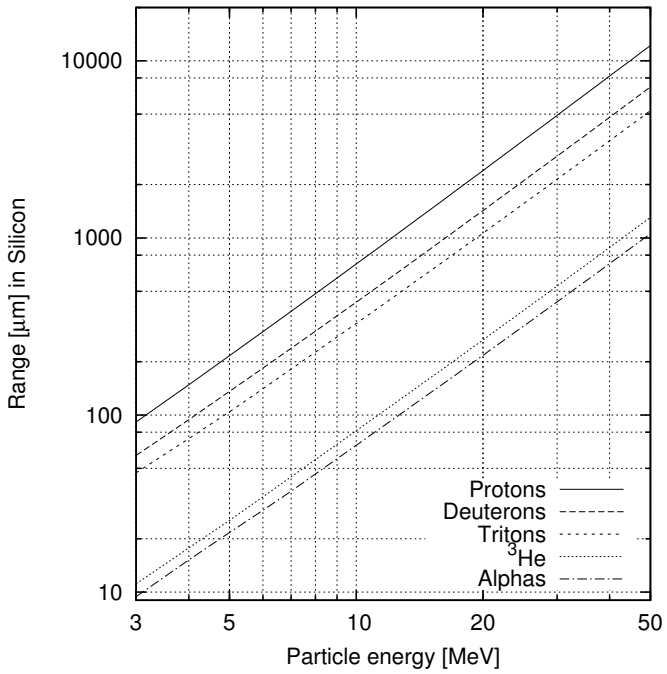

Figure 5.10: The range-energy curve for different charged particles in silicon. (Data from Ref. [10].)

The particle range should be taken in account for shielding purposes as well where the materials with higher atomic number are used. Tables of range and stopping power of chemical elements for charged particles can be found in Ref. [19].

It is worth mentioning that the stopping time for charged particles is few picoseconds in solid and few nanoseconds in gases and therefore the stopping time is neglected for detection purpose by solid (silicon) detectors.

5.2 Passage of neutral particles through matter

The choice of the converter for the generation of the charged particles depends on the type of neutral particle and its energy. This defines the physical process that will be used to register the primary particle, or which physical process will be dominant. The created charged particles are then detected by the process described in 5.1.

5.2.1 Photons and their interaction with matter

When a photon passes through the mass, the following processes may occur depending on the energy of the flying photon: Photoelectric absorption, Compton scattering and Pair production. The energy dominance of each process is determined by the choice of the converter.

The photon is electromagnetic radiation with specifics as zero charge, zero mass and the velocity of speed of light. Because of this properties the photon is penetrating far more than charged particles with the same energy. The photon does not loose its energy via coulombic interaction with electron in the atom because it is neutral. The photons penetrating through material and transfer their energy partially or totally to the electron energy which is deposited in the medium.

5.2.1.1 The nature of electromagnetic radiation

The main sources of electromagnetic radiation can be divided into processes:

- Gamma rays following beta radiation
- Annihilation radiation
- Gamma rays following nuclear reaction
- Bremsstrahlung
- Characteristic X-rays
- Synchrotron radiation

Gamma rays following beta radiation
Many radiation sources do not decay through beta radiation directly into ground state of daughter nuclei but rather decay into a meta-stable nuclear isomers with excited state followed by photon emission. Such example of gamma isotope which decays through β^- decay was shown in Fig. 5.3. In this example parent nucleus decays into ground state of daughter nucleus with low probability (5.64%) only and big amount of decay (94.36%) is into excited state followed by photon emission. The half-life of nucleus is much longer (e.g. years) in compare with lifetime of excited state of daughter nucleus (order of picoseconds) but as the gamma rays is the result of excited state after beta decay this radiation appear with half-life of parent nucleus.

The nuclear states have exactly defined energies and therefore the photon excitation is nearly mono-energetic which is useful for detector calibration. However gamma rays

sources based on beta decay are useful for detector calibration with energies lower than about 2.8 MeV due to limitation of half-life as sources with higher energies have half-life much shorter.

Annihilation radiation
During beta plus radiation a proton in parent nucleus is converted through weak interaction to an neutron. Simultaneously a positron accompanied by a neutrino is emitted (Eq. 5.2). The positrons lose their energy as they pass through the absorber and if the energy is sufficient small (near the end of their range) the positron combines with normal atomic electron in the process of annihilation. The both positron and electron disappear and instead of them two electromagnetic photons are emitted. Both with the same energy 0.511 MeV but oppositely directed. These photons have greater penetration ability and therefore their track and deposition is far away from the original positron track.

Gamma rays following nuclear reaction
One possibility to produce gamma rays with higher energy than is common for gamma rays produced through beta decay is combining the alpha emission with appropriate target material. The example of such reaction is

$$ {}^{4}_{2}\alpha + {}^{13}_{6}C \rightarrow {}^{16}_{8}O^{*} + {}^{1}_{0}n \tag{5.11} $$

where product nucleus ^{16}O is in excited state. To reach the ground state of product nucleus the gamma ray with energy 6.13 MeV is emitted accompanied by neutron. These processes are however useful mainly as neutron sources.

Bremsstrahlung
The electromagnetic radiation in form of Bremsstrahlung is widely used for production of X-rays from standard X-ray tubes where fast electrons are penetrating through target (typically Gold or Tungsten).

Due to deceleration of an electron by atomic nucleus the electromagnetic radiation is produced (according classical theory accelerated charge has to emit electromagnetic radiation). The converting process of electron kinetic energy into the Bremsstrahlung is more significant for materials with higher atomic number as well as higher electron energy leads to the higher portion of converted energy.

Energy spectrum produced by mono-energetic electrons is continuum where low-energy photons predominates and therefore this type of X-rays can not be used for detector calibration unless the additional filtration is used. However beside Bremsstrahlung, characteristic X-rays is also presented when fast electrons are penetrating through target (see next paragraph). The energy spectrum from thick molybdenum anode X-ray tube measured with a Si(Li) detector is shown in Fig. 5.11.

Beside Bremsstrahlung based on deceleration of an electron passing through absorber exists also the *Inner Bremsstrahlung* caused by acceleration of an electron via electron capture process (discussed earlier) which may add continuum energy spectrum based on radioactive nucleus decay.

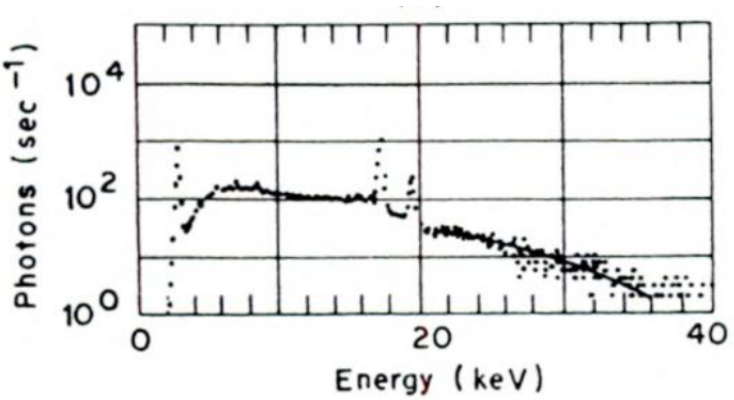

Figure 5.11: The energy spectrum from a thick molybdenum X-ray tube measured with Si(Li) detector (40 kV tube voltage, 90° electron beam incident angle, 32° x-ray takeoff angle). Characteristic X-rays visible at 17.4 keV for K_α lines, 19.8 keV for K_β line and at 2.4 keV for L lines. (Data from Ref. [20].)

Characteristic X-rays

There are several excitation processes which may change the normal configuration of orbital electrons. In some cases the orbital electron may be disrupted and move away from the original electron shell. This excited state takes very short time (nanoseconds or less for solid materials) to rearrange the electron shell and bring the atom to the ground state. During this period the energy is liberated and takes form of a characteristic X-ray photon which represents the difference between original and final state. Fig. 5.12 describes such excitation processes which lead to creation of vacancy in lowest K shell and radiation of characteristic X-ray photon during filling this vacancy by upper electron. The competitive process to the excitation of X-rays is creation of Auger electron. The ration of X-ray photons in its de-excitation process is defined by *Fluorescent yield*.

The excitation processes can be divided to two basic groups according origin:

- Excitation by external radiation
- Excitation by radioactive decay

Excitation by external radiation is due to external source as X-rays, fast electrons, protons or alpha particles which penetrate through specific target and cause the excited state of absorber atom or even create ionized atom. During de-excitation processes the characteristic X-ray photons are emitted (Fig 5.12 a–b).

Excitation by radioactive decay is caused by excited nucleus after nuclear reaction (described earlier). The excited nucleus may emit gamma rays and cause the ejection of orbital electron (most often from K shell). Other possible process is internal conversion when orbital electron (again most probable from K shell) is captured by atomic nucleus and last possibility is ejecting the orbital electron by β^- particle due to beta decay. During all processes the vacancy is created and rearranging processes follow when the characteristic X-ray photon is emitted (Fig 5.12 c–e).

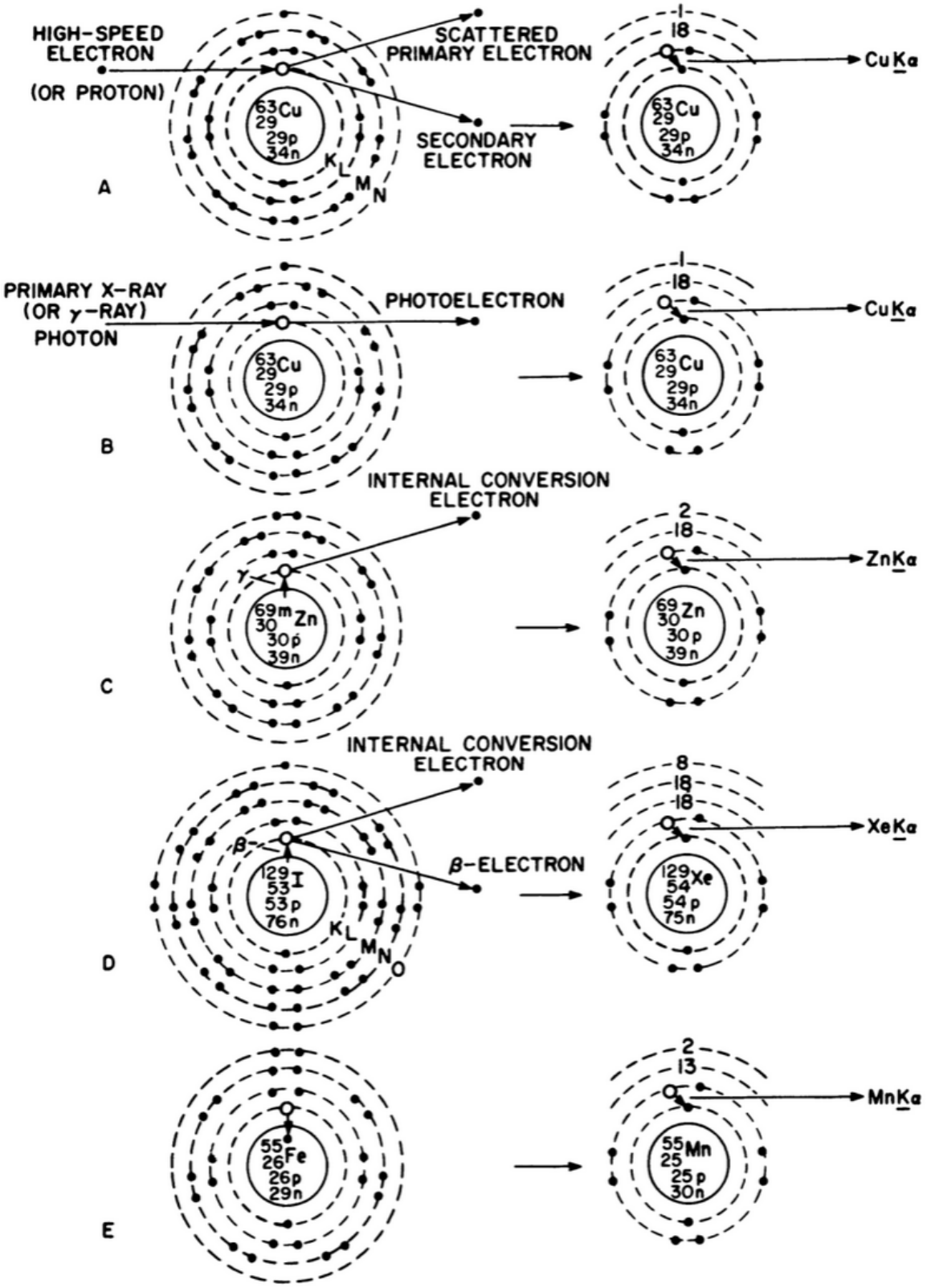

Figure 5.12: The excitation processes responsible for radiation of characteristic X-ray photons. External radiation due to ionized particles (a), Photoelectric absorption (b), Internal gamma conversion (c), Internal beta minus conversion (d), Electron capture (e). (Figure from Ref. [21])

5.2.1.2 Interaction mechanisms

The gamma rays may interact with the matter by three major interaction mechanisms:

- Photoelectric absorption
- Compton scattering
- Pair production

where photon energy is partially or totally transferred to the electron energy of absorber atom.

Photoelectric absorption
During photoelectric absorption the gamma rays interact with the absorber atom and lose their energy entirely. This energy is transferred to the electron energy which is ejected from the atom as *photoelectron* (Fig. 5.12 b). In the most cases photoelectron came from the most bound K shell with energy

$$E_{e^-} = h\nu - E_b \tag{5.12}$$

where E_b represents the binding energy of photoelectron in the absorber atom. The photoelectron leaves behind a vacancy which is immediately filled by electron from other shell or from the medium when the characteristic X-ray photon is emitted from the atom (Fig. 5.12 b). In some cases photon may cause the ejection of auger electron instead of X-rays itself. This absorption process is predominant for materials with high atomic number (gamma rays shields) but probability of absorption decreases with increasing of photon energy.
In Fig. 5.13 the dependence between the mass attenuation coefficient and photon energy in silicon is described. One can see that the attenuation is decreasing with the photon energy and for region with higher energy other processes as *Compton scattering* and *Pair production* are more significant. The *K-edge* peak at 1.839 keV represents the binding energy of the electron in K shell.

Compton scattering
For higher energies the Compton scattering begins to be significant. The photon energy is partially transferred to the electron which is ejected from the atom or shifted to the electron shell with less binding energy. The energy transferred to the electron varies from zero to the high fraction of total photon energy and depends on the angle in which the photon is scattered (Fig. 5.14). Compton scattering process is more significant for materials with higher atomic number (as well as Photoelectric absorption) and for gamma rays produced by radioisotope sources is the most important interaction mechanism.

Pair production
If the energy is higher than twice the rest mass energy of an electron the production of positron electron pair is possible. The probability is higher with increasing the energy and this interaction mechanism become predominant for very high energies exceed tens of MeV.

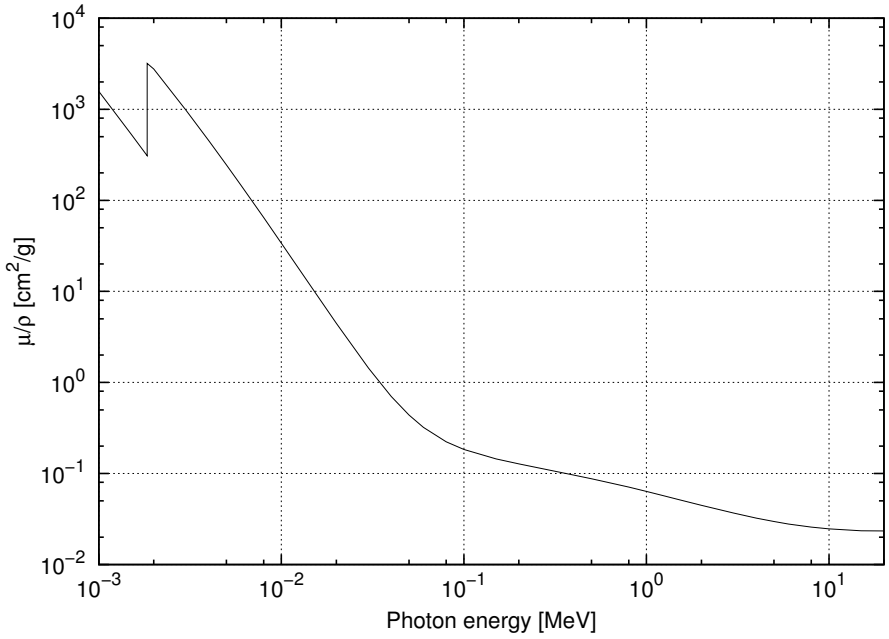

Figure 5.13: The mass attenuation coefficient as a function of photon energy for silicon (Data from Ref. [22]).

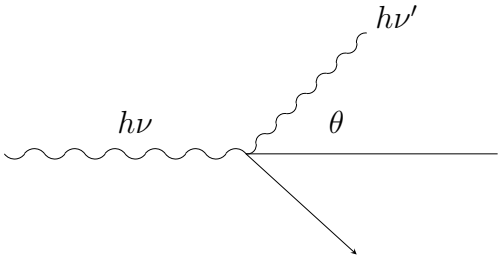

Figure 5.14: Compton scattering.

In addition an *annihilation* process is followed as positron penetrates through the absorber when two photons with energy 0.51 MeV are emitted (Fig. 5.15). The annihilation process contributes to the pair production and may have significant impact on gamma rays energy measurement.

5.2.1.3 Attenuation coefficient

The gamma rays lose their photons exponentially as they pass through an absorber (Fig. 5.16). There is fixed probability of the photon collision called *linear attenuation coefficient* and is defined as sum of the probabilities for each interaction mechanism:

$$\mu = \tau(Photoelectric\ absorption) + \sigma(Compton\ scattering) + \kappa(Pair\ production) \quad (5.13)$$

To take in account the density of the absorber the *mass attenuation coefficient* is also defined as:

$$mass attenuation coefficient = \frac{\mu}{\rho} \quad (5.14)$$

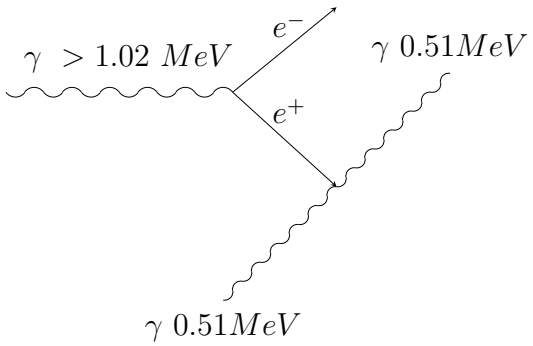

Figure 5.15: Pair production and annihilation process.

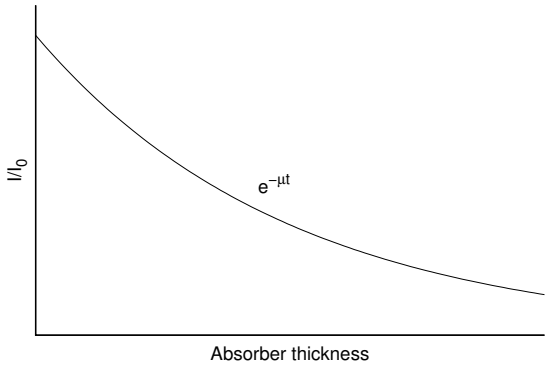

Figure 5.16: Exponential attenuation of the gamma rays. I_0 represents the initial amount of gamma-ray photons, I represents the number of transmitted photons through an absorber thickness.

5.2.2 Neutrons interactions

The neutrons are products of many types of nuclear reactions. In contrast to the charged particles the neutron radiation does not interact through coulomb force and therefore its penetration to the matter is much higher. Consequently, the detection of neutrons is impossible with current semiconductor detectors and therefore the radiation energy must be transferred to the electrons or nuclei of atoms to perform further nuclear reactions. Basically, the neutrons can transfer their energy for creation of heavy charged particles by usage of appropriate converter, which is typically connected to the semiconductor sensor. The energy of heavy charged particles are then measured by the process described above in 5.1.

In principle, the neutron radiography is the same as X-ray radiography. The neutron beam is focussed to the scanned object and subsequently the neutron intensity is measured by a neutron sensitive imaging detector. The main advantage of the neutron radiography is higher sensitivity for plastic materials (light elements). Essentially, the metallic pieces are transparent for the neutrons. In contrary, the X-ray radiography shows very good contrast of metallic materials (Fig. 5.17).

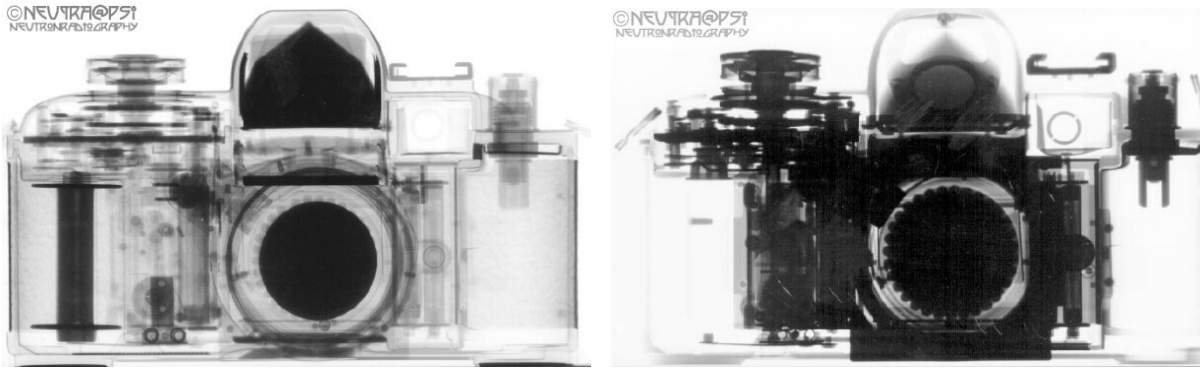

(a) The neutron radiography. (b) The X-ray radiography.

Figure 5.17: The neutron and X-ray radiography image of a film camera. The neutron radiography has higher sensitivity for the plastic materials (left) in compare to the X-ray radiography which has good contrast of metallic parts (right). Both images were taken at the neutron radiography facility (Neutra) at Paul Scherrer Institute (PSI) [23].

5.2.2.1 Thermal neutrons

The principle of the neutron detection by a planar semiconductor detector is shown in Fig. 5.18. The neutron converter ^{6}Li (LiF) is deposited on the silicon surface and allows a nuclear reaction:

$$^6Li + n = {}^3H + \alpha \ (4.78 \ MeV) \tag{5.15}$$

Products of the reaction between ^{6}Li and neutron are heavy charged particles: alpha particle with E = 2.05 MeV and triton (^{3}H) with E = 2.73 MeV.

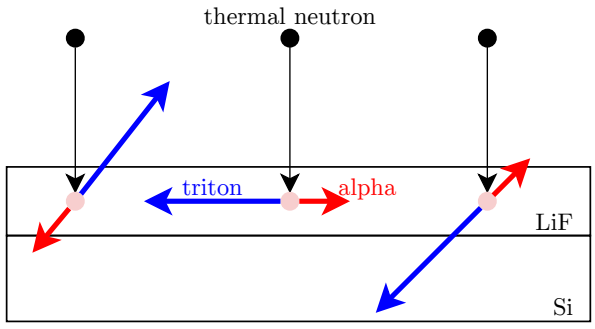

Figure 5.18: Principle of the neutron detection by a silicon planar neutron detector. The neutron converter LiF is deposited on the silicon surface.

The usage of the semiconductor detectors for neutron radiography has numerous advantages. Beside others: a very good spatial resolution, dynamic range and linearity. The detector sensitivity is affected mainly by limited effective thickness. The optimal converter

thickness has to be found with the respect to the neutron capturing possibility in the converter layer and the possibility of the secondary particle capturing in the semiconductor detector.

5.2.2.2 Fast neutrons

The neutron converter ^{6}Li is not suitable for the neutrons with the energy higher than hundreds of keV due to dropping of the neutron capture cross section. More efficient solution brings the detection of protons recoiled by fast neutron. The masses of neutron and proton are almost the same. Therefore, the energy of recoiled proton is nearly same as the neutron energy. As a converter can be used hydrogen-rich material with a nuclear reaction:

$$H + n = p + n \tag{5.16}$$

The principle of the neutron conversion by the polyethylene (PE) layer attached to the silicon shows Fig. 5.19. The polyethylene neutron converter attached to the silicon sensor reports very good spatial resolution which can be used for the fast neutron imaging [24].

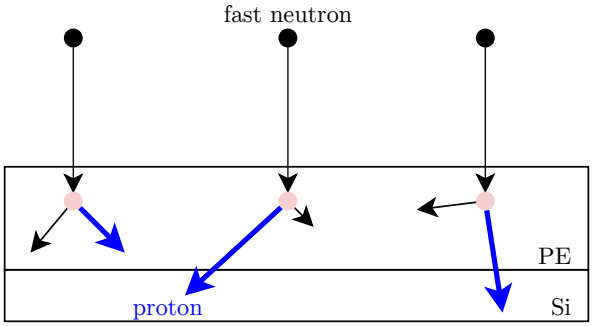

Figure 5.19: Principle of the fast neutron detection by a silicon planar neutron detector. The protons are recoiled by fast neutrons in the polyethylene layer (PE).

5.3 Semiconductor detector

Semiconductor detectors are used in many areas of science and technology due to their unique characteristics which are not available with other type of detectors. Besides others, semiconductor provides the unique spatial resolution, very high readout speed, signal in electric form, possibility to measure energy, position and time of arrival at the same time and availability for integration with front-end readout chip. Compared to gas or scintillation detectors, semiconductor detectors have good energy resolution and are much more compact.

Silicon detectors are the best known semiconductor detector with the most advanced technology available. The best knowledge of material characteristic is due to wide use in

electronics. Silicon detectors are fabricated from slices of a silicon single crystal and can have much less thickness and spatial dimensions in compare with most other semiconductor materials. For instance, silicon detectors can be operated at room temperature in contrast with germanium detector (higher leakage current) without any need of cryogenic cooling.

Produced silicon sensors used in this thesis are p-type which means higher radiation tolerance than n-type detector. Worth mentioning, the production of p-type silicon was not trivial some years ago. Last but not least, the creation of SiO_2 passivation on the top of the Si layer is relatively easy process that allows the creation of complex connectivity with AC coupling capacitors or development of the monolithic detectors.

To obtain the path information of ionizing particle the diode as a detector may be split to the strips or the pixels. The basic principle of the silicon strip detector is shown in Fig. 5.20. The ionizing particle is penetrating to the fully depleted silicon sensor. The electron–hole pairs generated along the particle path drift along electric field to the sensor plates. The holes drift to the back-plane while the electrons are collected at the $n+$ implant where they are induced by AC–coupling capacitor (or directly) to the Charge Sensitive Amplifier. AC–coupling capacitor can be put outside the sensor, however, to produce sufficiently large capacitor on the LSI electronics it is almost impossible. The main aim of the AC–coupling is to shield the electronics from the dark current which can lead to the shifts of operation point and subsequent changes of the thresholds can lead to the reduction of the dynamic range or even to the saturation.

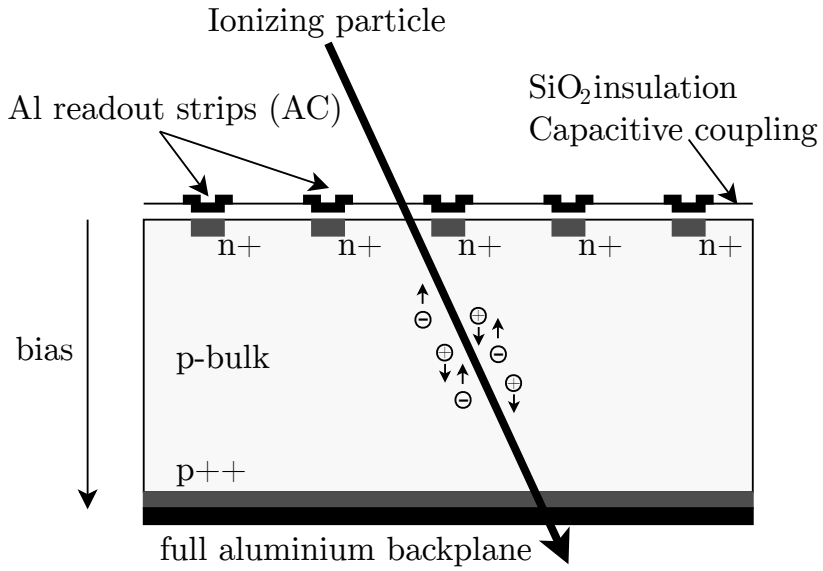

Figure 5.20: AC–coupled silicon strip detector. Ionizing particle creates electron–hole pairs inside depleted sensor. The electrons and the holes travel to the sensor plates and through AC–coupling capacitor to the readout electronics where the signal is amplified and shaped.

The elements contributing to the noise originating in the silicon sensor are shown in Fig. 5.21. The main contributors are leakage current I_L, load capacity C_D, serial and parallel resistances R_S and R_P while load capacitance is mainly caused by inter–strip capacitance and the capacitance between the strip and the back-plane.

The Charge Sensitive Amplifier (CSA) shown in Fig. 5.22 consists of inverting amplifying circuit that in the ideal case is defined as $U_{OUT} = -AU_{IN}$ and feedback capacitor

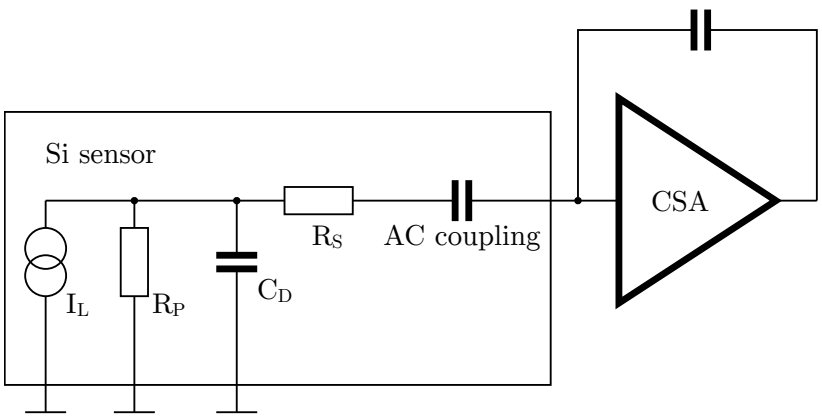

Figure 5.21: Simplified schematic of a sensor with its CSA amplifier. The main noise contributions are leakage current I_L, parallel and serial resistance R_P, R_S and load capacitance C_D.

C_F. To achieve the operational condition, the feedback capacitor has to be discharged by high–ohmic resistor or by current source since high–ohmic resistors are very complicated to produce in LSI electronics. The input capacitance C_{IN} is mainly caused by gate capacitance of the input MOSFET while C_D represents the sensor capacitive load at the input.

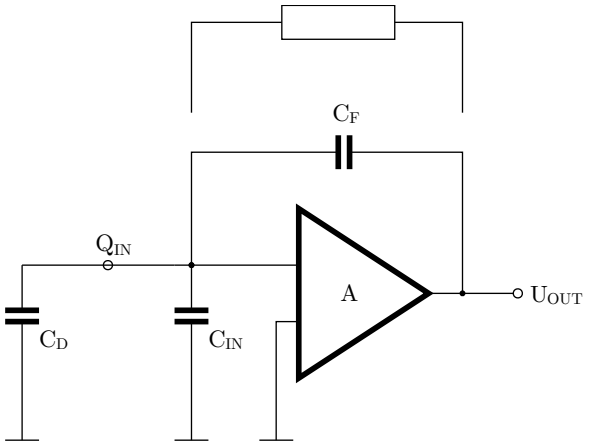

Figure 5.22: Principle of a Charge Sensitive Amplifier with its capacitive feedback. The system has to be initialized to operating condition by high–ohmic resistor or by current source.

Any charge at the input will cause the output change according equation:

$$U_{out} = -\frac{Q_{IN}}{C_F + \frac{C_D + C_{IN} + C_F}{A}} \rightarrow -\frac{Q_{IN}}{C_F} \tag{5.17}$$

The equation 5.17 is valid for large amplification when the output is given by ratio of injected charge over feedback capacitor. In this case all injected charge is transferred from the sensor to the feedback capacitor. In the case of lower amplification or large capacitive load of the detector the charge is transferred from the detector to the feedback capacitor only partially.

Chapter 6

The architecture of the detection system

Several chip versions of the PH32 chip have been developed. The last fabricated chip PH32v7 is supposed to be the final prototype before ongoing engineering run. Because this version of the chip is not tested by the time of this study, the following description of the detection system is dedicated to the last most tested PH32v6 chip version. The current chapter is dedicated to the overall description of the detection system which is the basis for the following chapters that present the main focus of this study.

A block schematic of the detection system is shown in Fig. 6.1. The PH32v6 front-end readout chip has been manufactured in a commercial 180 nm CMOS technology by its dimensions 3.5×2 mm^2. The chip contains 32 identical readout channels which are connected through the AC coupling to the strips of silicon n$^+$–on–p sensor of 525 µm thickness with the p-stops between each individual strips. The use of the high resistivity silicon (>10 kOhm·cm) ensures for the sensor thickness of 525 µm the full depletion of the sensing volume at −150 V.

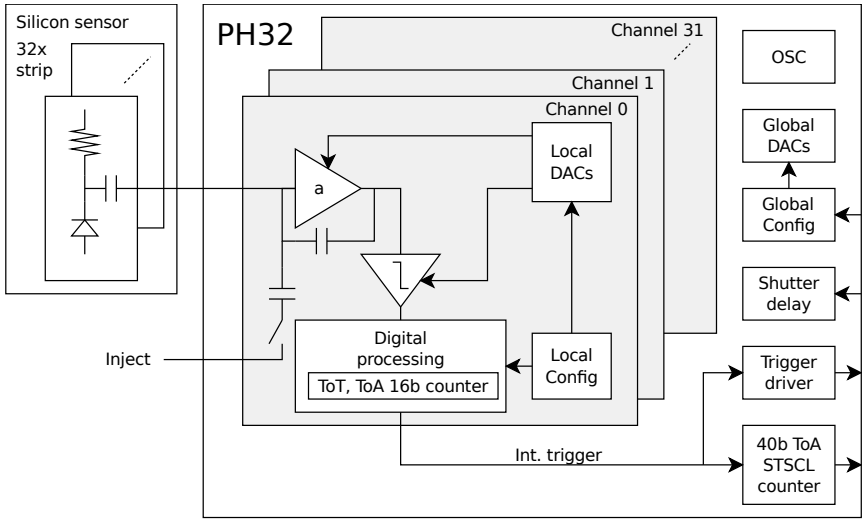

Figure 6.1: Block schematic of the detection system with the PH32v6 chip and the silicon sensor with 32 channels.

In the next section, the silicon sensor will be described briefly as it is not the point of interest of this study. The afterward section is dedicated to the PH32 chip itself with more detailed description of the digital part of the chip, which is my contribution in complete.

6.1 The silicon sensor

Fig. 6.2 shows two variants of the silicon strip sensor of 525 µm thickness. The first one contains 32 identical channels with dimensions of 250 µm × 18 mm and the capacitance ≈ 4.6 pF per channel. The second one contains only 16 channels with the various width size. The wide size strips have dimensions 1680 µm × 8 mm and the capacitance ≈ 5 pF and narrow strips with dimensions of 200 µm × 8 mm and capacitance ≈ 1.5 pF per channel. The area ratio of wide and narrow strips is around one to eight. This is together with the charge collection scale of the PH32 useful for the dose rate measurement in few orders of magnitude as well as for the energy measurement of particles with the energy difference in range of ≈ 10 keV to ≈ 30 MeV - typical for soft X-rays, β radiation and charged ions. The size of the sensor was chosen in respect of the fact that the device is developed mainly for the dose rate measurements. The strip capacitance values are our best approximation, which includes fully depleted strip to the back plane (bias at -150 V), side capacity to the back plane, inter-strip capacity and AC coupling capacity. The measured strip AC coupling capacity (SiO_2 layer of 320 nm) between the metal and the silicon is 290 pF. The new ongoing production of the sensors will produce the sensor of 60 nm SiO_2 thickness which allows to increase the AC coupling capacity. The production itself is provided by the ON Semiconductor foundry in Czech Republic.

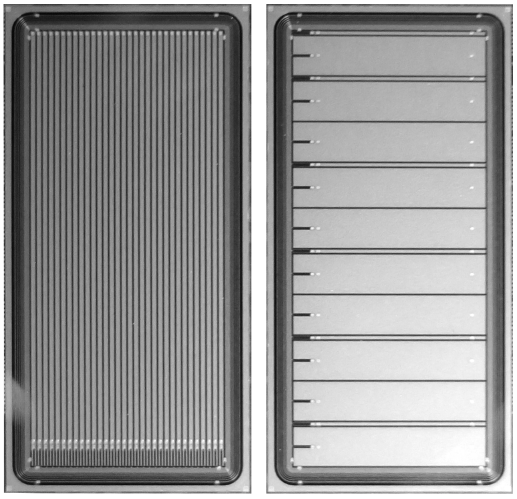

Figure 6.2: Two variants of n^+–on–p silicon strip sensors of 525 µm thickness produced on high resistivity silicon (>10 kOhm·cm) with the p-stops between individual strips. The sensor on the left side contains 32 identical strips while the right type contains 10 wide and 6 narrow strips.

6.2 The Ph32 readout chip

At the present time, there are several versions of the PH32 chip fabricated during the last five years. These versions were gradually developed according to the measurements of the previous versions what led to several changes in both analog and digital parts. However, this section is focused on the last well tested PH32v6 chip and the main intention is on the digital part which is my prime contribution. The complete specification of the PH32v6 chip is summarized in appendix A.

At this point, I would like to mention the serious troubles we have encountered during the development, which I believe, were not on our side. During the last years, we were forced to change both the foundry and the manufacturing process several times. Table 6.1 shows all versions of the chip and the appropriate processes. The first complication came by unreliability of the Lfoundry which have gone bankrupt. Lfoundry moved its production and is now operating again, but it took time. Meanwhile we have chosen AMS for our future MPW submissions. During the development, AMS foundry once updated the process because of moving the production (Metalization changes increase the antenna effects). At the end of development the question about the engineering run arose. At this point, AMS foundry announced the end of the process lifetime which led to serious issue (MPW in a C18 process is still available, while engineering run not). Hopefully, we found the solution in TSI foundry which offers the old C18 process. We redesigned our design into the old process once more and the engineering run is ongoing just now.

Fig. 6.3 shows the top layout of the PH32v6 readout integrated circuit with the all basic analog and digital blocks, several test structures (STSCL, time counter) as well as the transistor test structures which were be used at a radiation hardness evaluation [A.18]. The radiation hardness was also evaluated for earlier version of the PH32 chip which has been manufactured in a commercial 150 nm CMOS technology [A.8].

6.2.1 The analog part

Fig. 6.1 describes the basic concept of the channel analog part. The signal from the sensor is transferred through the AC coupling capacitor (sensor side) to the input of the Charge Sensitive Amplifier (CSA) where the signal is amplified. Thereafter, the signal is compared to the threshold of the discriminator. The output of the discriminator is processed by the digital part. The CSA sensitivity can be adjusted in two operation modes by changing the feedback capacitance between 10 fF and 1 pF into the High Gain (HG) mode for low energy X-rays and beta radiation and the Low Gain (LG) mode for charged ions such as alpha particles. Each channel contains the Digital to Analog Converters (DACs) to adjust a feedback current of the CSA as well as the threshold of the discriminator during the calibration process for each channel separately. The aim is to obtain an equal output of the CSA in all channels for different injected charges and for both gain modes to ensure a high dynamic range. The comparison between the post-layout simulation of the CSA response to various injected charge and the real response to injected charge in HG mode is shown in the Fig. 6.5.

Chip version	CMOS technology	Major changes
PH16	Lfoundry 150 nm	first prototype 16 channels
PH32v2	Lfoundry 150 nm	32 channel
PH32v3	AMS 180 nm (C18)	redesigned to new technology
PH32v4	AMS 180 nm (C18)	sensor switch linearity improvement lowering input noise hit triggering hit occurrence synchronized with shutter
PH32v5	AMS 180 nm (aC18)	redesigned to new technology pseudo-counter → asynchronous counter lowering input noise lowering threshold level of discriminator shutter delay global STSCL counter
PH32v6	AMS 180 nm (aC18)	hit_global not synchronized SPI compatibility
PH32v7	AMS 180 nm (aC18)	redesigned for engineering run input capacitors changed
PH32v8	TSI 180 nm (C18)	engineering run redesigned to previous technology

Table 6.1: The PH32 versions and significant differences.

In overall, the HG mode is able to measure generated charge in the range from about 3 ke$^-$ to 40 ke$^-$ and the LG mode in the range from about 300 ke$^-$ to 4 Me$^-$. The electronic noise is about 1100 e$^-$ for the chip calibration charge of 10 ke$^-$ at HG mode and 2300 ke$^-$ for the chip calibration charge of 2 Me$^-$ at LG mode.

For completeness, Fig.6.6 shows the layout of one channel. The layout contains the input pad prepared for the wire-bonding which is connected directly to the CSA input. Besides the analog part, the digital part is visible on the right side of the channel.

6.2.2 The digital part

The digital part of all produced PH32 chips is my own contribution. This section describes step-by-step all digital blocks and new approaches that have been applied during the development.

The digital part of the PH32v6 chip contains channel digital part (Fig. 6.6), global part (Fig. 6.7(a)) and shutter shifter (Fig. 6.7(b)). The global part contains except the global configuration also the sampling frequency management circuit, triggering and I/O signals management. Global connectivity between the individual blocks is shown in Fig. 6.8.

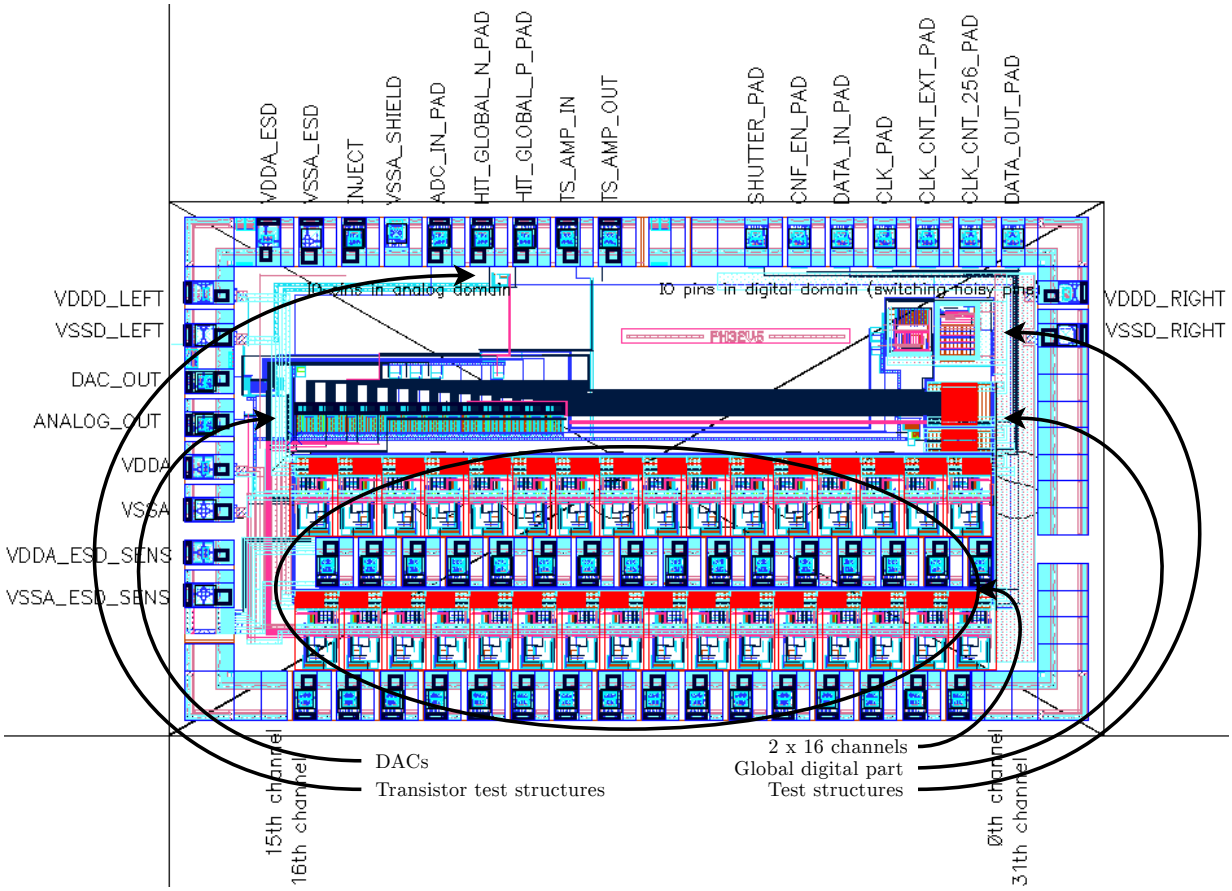

Figure 6.3: Top layout of the PH32v6.

6.2.2.1 Clock signals

For the chip operation two clock signals are needed: *clk* and *clk_cnt*. The *clk* is used for loading the configuration data into the configuration register and for reading measured data from the chip. The *clk* is supplied from outside of the chip and the frequency should be in the range of 10s MHz. The *clk_cnt* is a reference signal for the ToT and the ToA measurement. Besides this purpose, the clk_cnt is used for the synchronization of the asynchronous output of the discriminator, which is the input to the digital part. Its frequency range is 100s MHz and it is asynchronous to the *clk*. This signal can be provided either externally (*clk_cnt_ext*) or from an internal Voltage Controlled Oscillator (VCO). The source of this clock signal can be switched by 127^{th} global configuration bit (*clk_cnt_sel*, table A.2). Nominal frequency of the VCO is ≈ 250 MHz and it can be further adjusted by the *VBIAS* DAC (table A.2). The frequency from the internal oscillator can be further divided by appropriate settings of 125^{th} and 126^{th} global configuration bits (*clk_cnt_div*, table A.2).

The usage of the external source of the sampling frequency is only for specific applications due to its single ended input port limitation which allows the frequency in the range

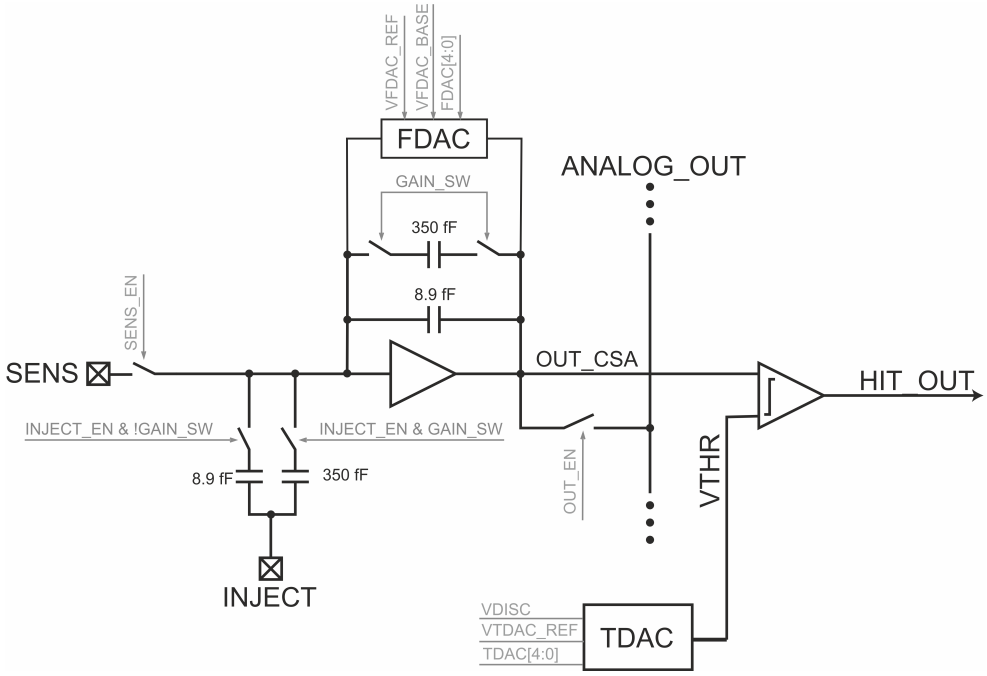

Figure 6.4: Block schematic of the channel analog part of the PH32v7 chip. The channel contains charge sensitive amplifier with feedback capacitors, switches for mode operation changing, Feedback DAC (FDAC) for feedback current tuning and Threshold DAC (TDAC) for discriminator threshold tuning. The PH32v6 chip disposes with the same arrangement except the capacitance values which are 10 fF (HG) and 1 pF (LG).

of 10s MHz only. The low sampling frequency is inappropriate for the ToT and the ToA measurements due to low resolution. Another important note is that the input is synchronized and low frequency causes the higher dead-time. Due to these facts, the external source of the sampling frequency is obsolete and it is not applied in the last PH32v7 chip version.

However, the input synchronization is probably not necessary, because we have not observed any metastable state during the PHpix chip operation. The PHpix chip is the simplified PH32 chip and it is primarily used only for the radiation imaging where only the hit-counting mode is required. The PHpix chip has no sampling frequency at all. The chip is described briefly at the end of the study (section 10.2). This is one of possible upgrade which should be applied to the potential future development of the PH32 chip. Among other things, it would lead to the large drop in power consumption in the hit-counting mode.

The VCO operation is described in more detail in section 7.3 which is dedicated to the cross-talk between the digital activity and the internal oscillator. From the described observation, the VCO should work at the maximum frequency due to minimal dependency on the VBIAS.

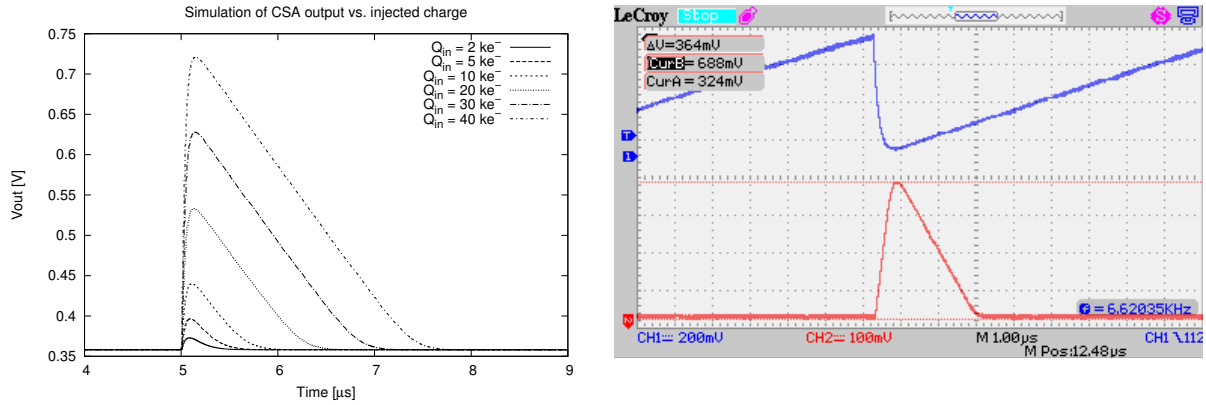

(a) Simulation of the CSA output vs. injected charge.

(b) Measurement of the CSA output (CH2) for charge injection of 40 ke⁻ (CH1).

Figure 6.5: Simulation and measurement of the CSA output of the PH32v6 chip. The output of the CSA is relatively linear for a wide range of injected charge (6.5(a)). The output of the CSA was measured for injected charge 40 ke⁻ which corresponds to the injection of 640 mV peak-peak with respect to injection capacitor 10 fF (6.5(b)). The CSA behavior is strongly dependent on the DACs settings.

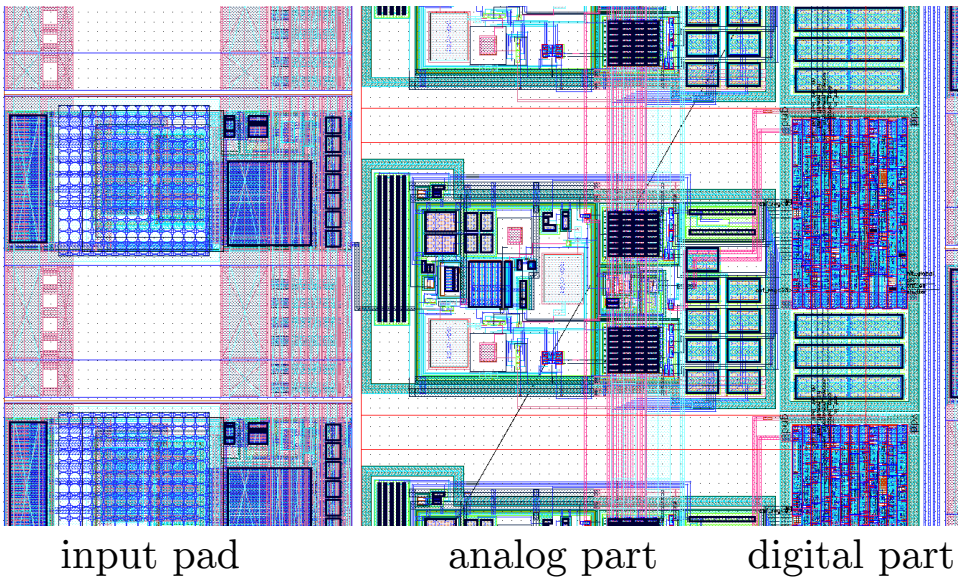

Figure 6.6: Layout of one channel, PH32v6 chip.

6.2.2.2 Operation modes

All versions of the PH32 chip can operate in four operation modes (table 6.2) according to the local configuration. Every mode is used for a different measurement purpose and subtly varies in synchronization. A simplified description of the operation modes is shown

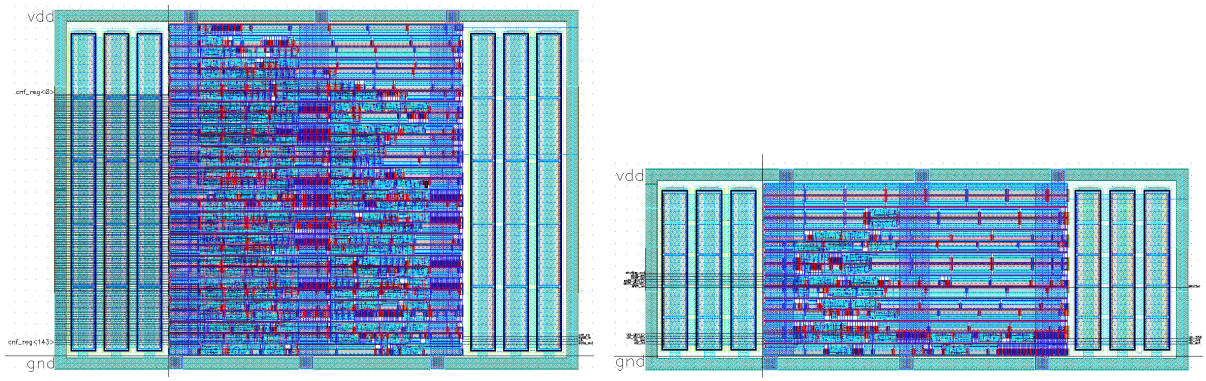

(a) (b)

Figure 6.7: Layout of global configuration part (6.7(a)) and layout of shutter shifter (6.7(b)), PH32v6 chip.

in Fig. 6.9. The hit-counting mode is supposed to be used for the dose rate measurement which is in more detail described in section 9.2. The energy of first hit mode is used for measurements related to the evaluation of the energy spectrum. Various energy spectra have been measured by different chip versions (section 9.1). The energy integrated during the measurement is used to evaluate overall energy exposed by any radioactive sources. Finally, the time of arrival of the first hit is supposed to be used for the measurement of the time when the particle arrives to the sensor which has huge potential in the particle tracking or ion mass spectroscopy [25].

MODE_1	MODE_0	Selected mode
0	0	Hit-counting
0	1	Energy of first hit
1	0	Energy integrated during measurement
1	1	Time of arrival of the first hit

Table 6.2: Mode configuration.

6.2.2.3 The communication with the PH32v6 chip

The PH32v6 chip consists of 32 identical channels connected in series with the global part (Fig. 6.8). The data from the measurement of each channel are stored in a 16-bit asynchronous counter which can be switched to the shift-register to enable serial data read and write. However, till the PH32v4 chip version, the chip contains 13-bit pseudo-counter. The counter was redesigned due to relatively high power consumption which led to the crosstalk to the analog front-end. The wide treatise devoted to this issue is in section 7.1. The usage of asynchronous counter is new approach in the readout chips associated with the radiation detectors.

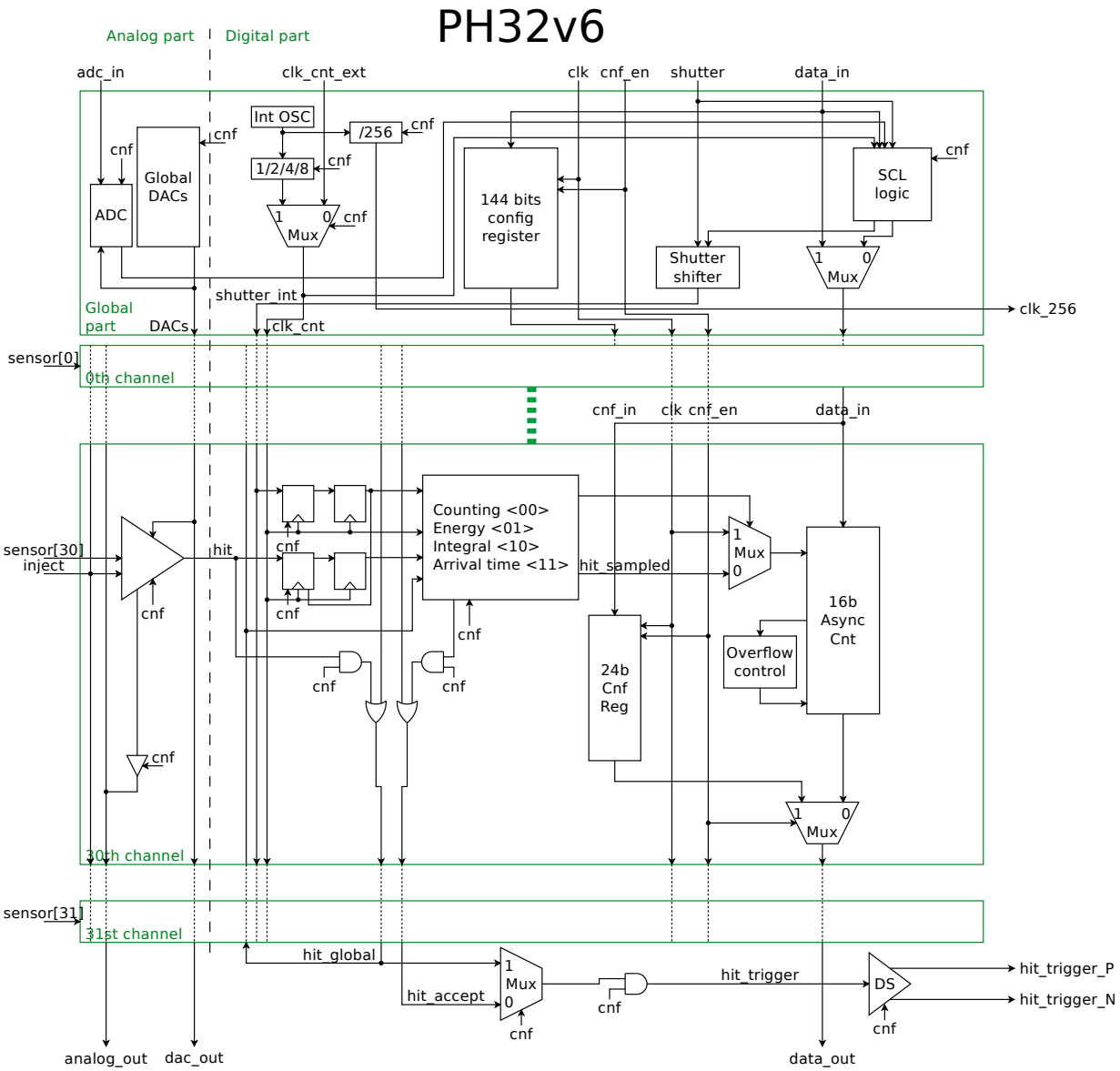

Figure 6.8: Block schematic design of digital part of PH32v6 readout integrated circuit.

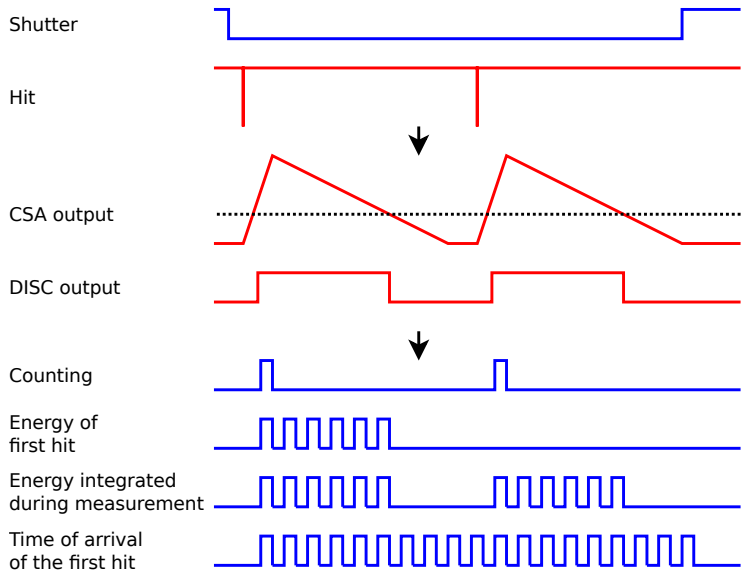

Figure 6.9: Simplified description of the operation modes.

The communication with the chip is done by a single serial data line which shifts data to the on-chip configuration registers and reads data from the channel data registers. In both cases the data can pass through the chip from the *data_in* signal to the *data_out* signal. Layout of the registers depends on the operation which is performed with the chip. While the chip configuration, the registers consist of the global configuration register (144 bits) and 32 local configuration registers (each 24 bits) as shown in Fig. 6.10.

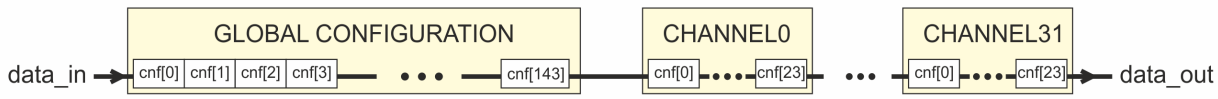

Figure 6.10: Layout of configuration registers in the PH32v6 chip.

In the reading mode, the chip register is shortened to read only the measured data (32 × 16 bits). Layout of the register in the readout mode is shown in Fig. 6.11.

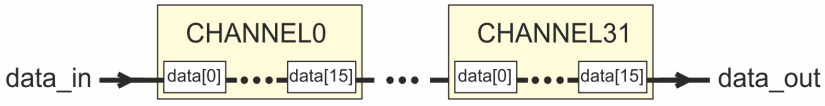

Figure 6.11: Layout of data registers in readout mode in the PH32v6 chip.

For a proper function the asynchronous counter must be initialized to 65535 (16'b1111_1111_1111_1111). After that, the asynchronous counter reacts as a sub-tractor by one with a positive edge of the reference clock and therefore, the value of the counter obtained by additional hardware must be inverted to obtain the correct information of the counts. However, the additional information of correct startup is presented in the results also, and therefore, additional step has to be done for proper readout as will be describe afterwards.

Hit_global

The chip contains the information of channel occupation or-ed from all channels by signal called *hit_global* (Fig. 6.8). This feature, together with the signal *hit_accept* (described afterwards) is new approach in the triggering of the external hardware and allows to avoid cutting off the first hit interference.

The signal *hit_global* is enabled by 17th local configuration bit (*hit_global_out*, table A.3) for every channel separately and is independent of the sampling clock *clk_cnt* (timing diagram 6.1). Till the chip version PH32v5, the signal *hit_global* is presented only during measurement when the signal *shutter* is in a low state and synchronized by sampling clock. However, it turned out that the information about the hit occupancy is desirable also before measuring and afterwards, it can be used for hit activity measurement itself without any digital processing inside the chip.

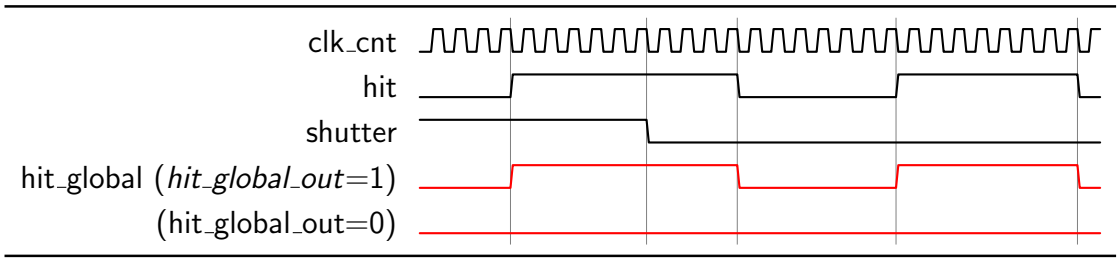

Timing diagram 6.1: Demonstration of the *hit_global* functionality according to 17th local configuration bit (*hit_global_out*, table A.3) in chip version PH32v6.

Shutter_wait

The presence of above described feature allows the synchronization of the measurement startup. This new approach allows to eliminate the chopping off the first hit occurrence arrive to the digital part for following processing. This feature is useful mainly for the energy measuring of the first arrive particle, where without this possibility, the energy would be lowered by certain part according the *shutter* occurrence. In this context, the measurement can start only if there is no occupation at all (timing diagram 6.2).

This feature, called *shutter_wait*, can be enabled by 16th local configuration bit (*shutter_wait*, table A.3) for every channel separately. Note that this feature can run properly only if the *hit_global* feature is enable as well. From timing diagram 6.2 one can see that the *shutter* is sampled by negative edge of sampling clock and has phase shift of two sampling periods as well as signal *hit*. This is because the signals *hit* and *shutter* are asynchronous to each other and without synchronization the meta-stable state can occur (the necessity for synchronization will still be discussed). The synchronized signal derived from the signal *shutter* is called *shutter_sync*. Also has to be mention, that the signal *hit* is synchronized only when the signal *shutter_sync* is in a LOW state. To be complete, one has to know, that the signal *shutter* can be also shifted in global part and is derived as the signal *shitter_int*

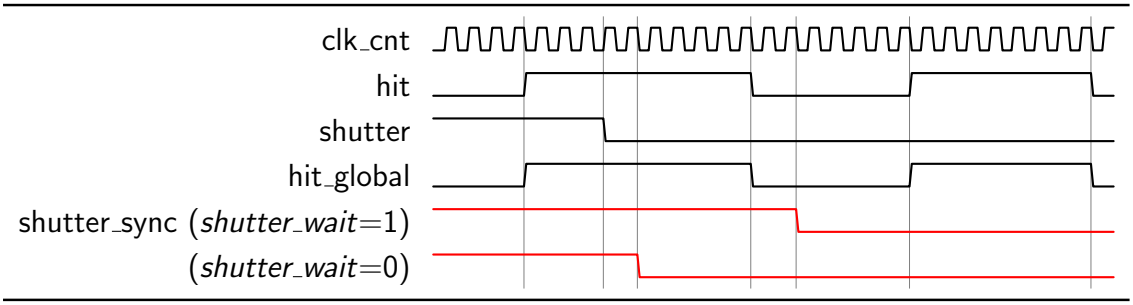

Timing diagram 6.2: Demonstration of the *shutter_wait* functionality. Waiting for unoccupied chip vs. direct shutter according to 16$^{\text{th}}$ local configuration bit (*shutter_wait*, table A.3) in chip version PH32v6.

in Fig. 6.8. Also this shutter shifter functionality is novel approach to the readout chips of our focus and will be described afterwards.

Immediately after beginning of the measurement with no occupation presented at all channels, the counter is subtracted by one. Otherwise, we read the initial value 65535 which means, that the system was occupied and successful start-up was halted. The sub-tractor can not overflow due the control mechanism implemented and therefore the maximum value of counter (after inverting and subtracted by one due to the correct start-up information) is 65534. For correct running of asynchronous counter and results see table 6.3. The configuration of the *hit_global* and *shutter_wait* functionality has no effect on the subtracting. The concept of the addition of the chip occupation information to the measured data is another new approach used in radiation measurement technique.

Asynchronous counter	Result	Description
"1111_1111_1111_1111"	-1	The system was occupied and no data was taking.
"1111_1111_1111_1110"	0	The startup was correct, no hit presented.
"1111_1111_1111_1101"	1	The startup was correct, 1 hit presented.
"1111_1111_1111_1100"	2	The startup was correct, 2 hits presented.
"1111_1111_1111_1011"	3	The startup was correct, 3 hits presented.
	.	
	.	
	.	
"0000_0000_0000_0010"	65532	The startup was correct, 65532 hits presented.
"0000_0000_0000_0001"	65533	The startup was correct, 65533 hits presented.
"0000_0000_0000_0000"	65534	Counter reached maximum value of 65534.

Table 6.3: Running of asynchronous counter and the results of data after inverting and subtracting by one. The PH32v6 chip.

Hit_accept

The next novel method is the information of the first accepted hit which is or-ed from all channels in the same way as signal hit_global *hit_global*. This feature is called *hit_accept* (Fig. 6.8). The signal *hit_accept* will change the state from '0' to '1' if the first hit arrived to the digital part after successful start-up (the counter tilt the value to 16'b1111_1111_1111_1101). Afterwards, the signal will be erased by reading the asynchronous counter (timing diagram 6.3). The signal *hit_accept* can be enabled by 18$^{\text{th}}$ local configuration bit (*accept_out*, table A.3) for every channel separately. Note that the *hit_accept* functionality depends on the *shutter_wait* functionality also and that the signal is triggered by signal *hit* which is synchronized by negative edge of sampling clock only when the signal *shutter_sync* is in a LOW state.

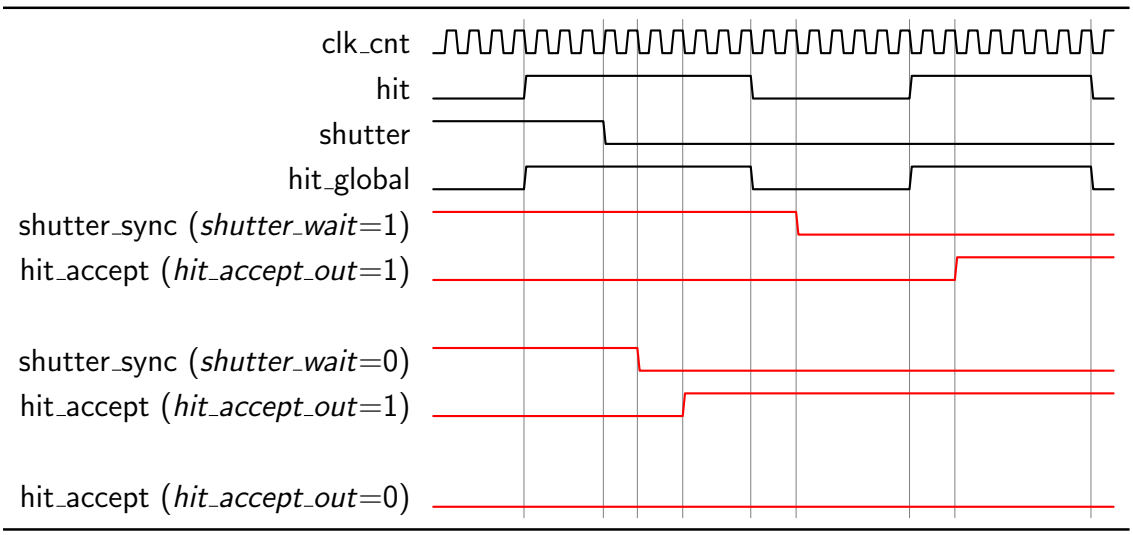

Timing diagram 6.3: Demonstration of *hit_accept* functionality. The signal *hit_accept* is triggered by signal *hit* synchronized by negative edge of sampling clock along with *shutter_sync* is in a LOW state. The functionality depends on 18$^{\text{th}}$ and 16$^{\text{th}}$ local configuration bits (*hit_accept_out* and *shutter_wait*, table A.3). The PH32v6 chip.

Hit_trigger

Both signals, the *hit_global* and the *hit_accept*, can be used except the triggering also for the debugging. This has become particularly useful during the development of the chip. So that we can use both functions at one output, both signals are merged together into one signal named *hit_trigger* (Fig. 6.8). The *hit_trigger* can be activated by 117$^{\text{th}}$ global configuration bit (*hit_trigger_en*, table A.2) as well as choosing the functionality between the *hit_global* or the *hit_accept* feature by 118$^{\text{th}}$ global configuration bit (*hit_trigger_sel*, table A.2). The exact behavioral of described features is shown in timing diagram 6.4. Keep in mind that the *hit* is sampled by sampling frequency with the phase shift of two

sampling clocks and therefore the signal *hit_trigger* has the same phase shift if the *hit_accept* feature is selected due to derivation from the synchronized signal. On other hand, if the *hit_global* feature is selected, there is no phase shift, because the signal *hit_global* is derived from asynchronous signal *hit* only.

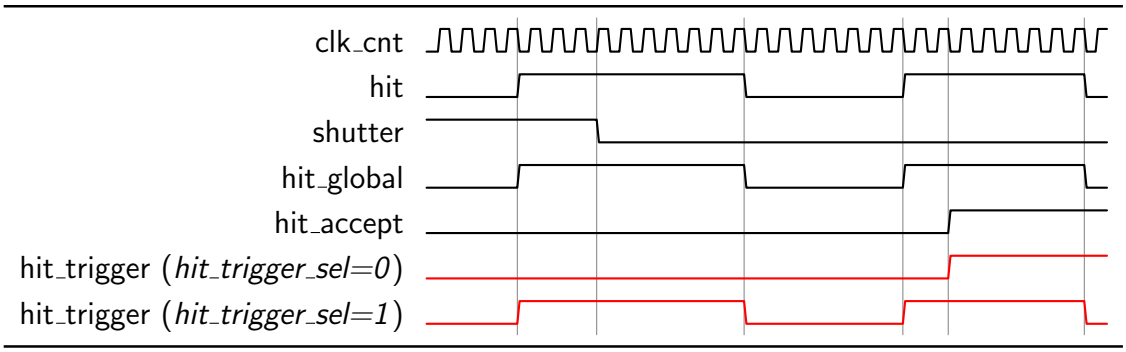

Timing diagram 6.4: Demonstration of the *hit_trigger* functionality which can be enabled by 117th global configuration bit and selecting between two operational modes (hit_global or hit_accept) by 118th global configuration bit (*hit_trigger_en* and *hit_trigger_sel*, table A.3). The PH32v6 chip.

This novel approach about the triggering itself has two main useful advantages. Firstly, the information about the first arrival hit is useful for the energy measuring when the exposition may be immediately stopped followed by data capturing and finished by the next exposition run. In this sense the energy measurement can be more effective, especially if a medium with low radiative decay is in use. Secondly, trigger is used for the ToA measurement, either only by the trigger output or together with the ToT measurement for the time-walk effect correction eventually. Both approaches with the measurement results are discussed afterwards (Chapter 8).

Differential driver

To avoid the cross-talk between the analog and the digital part, the signal *hit_trigger* is driven by the proprietary differential driver which is fully configurable by the global configuration register (table A.2). The configuration of the differential driver is summarized in table 6.4. The *lvds_range* (80th – 87th configuration bits) sets the lower (higher) voltage level of the positive (negative) output approximately in the range from 600 mV to 1.1 V (Fig. 6.12). Analogously, the *lvds_rising* (72th – 79th configuration bits) sets the rising edge of differential driver. The basic description of the differential driver is due the fact that it is not my own contribution and will not be described in more details further.

STSCL periphery

Tha last part related to the digital circuits of the PH32v6 chip belongs to the STSCL

Bit number	functionality	Part	Default value	Description
87:80	lvds_range	analog	1.8 V	0000 0000
79:72	lvds_rising	analog	0 V	1111 1111

Table 6.4: The global configuration bits related to the proprietary differential driver settings in the PH32v6 chip.

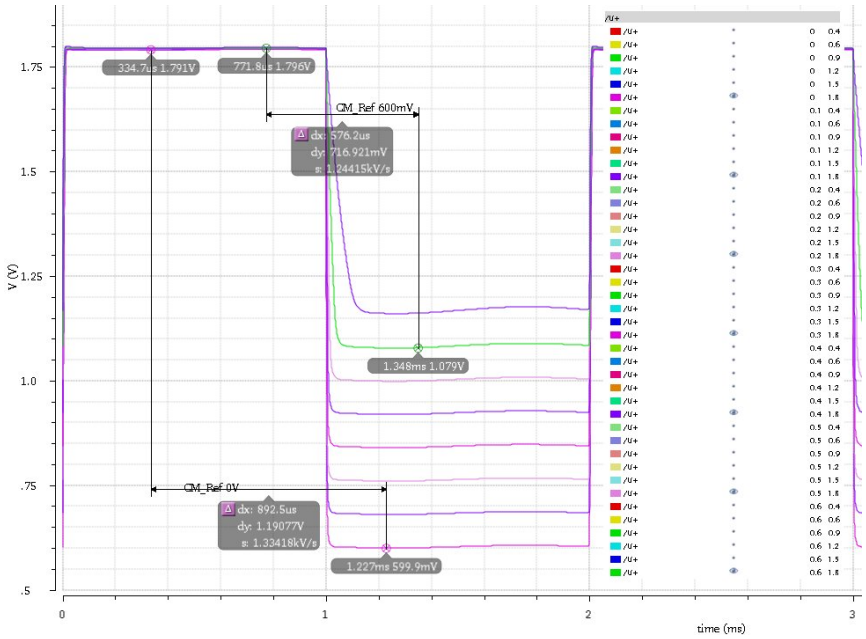

Figure 6.12: The simulation of the positive output of the proprietary differential driver according the *lvds_range* global configuration (80^{th} – 87^{th} configuration bits). The PH32v6 chip.

periphery. This circuit was developed (it is not my own contribution) from the need to reduce the cross-talk between the digital and the analogue part during digital activity while the chip is running in the exposition run. The STSCL circuit contains the 40-bit synchronous counter which is successfully used for the ToA measurement together with the measurement of the sampling frequency. This allows to reduce the fluctuation of the sampling frequency which is a significant source of the error. Secondly, lowering the sensitivity of Charge Sensitive Amplifier (CSA) to the fluctuation of digital power rails is also very important. The huge potential for this approach is in the ToA measurement provided by global STSCL counter in parallel with the ToT energy measurement. This allow the time-walk effect correction which will be described afterwards (Chapter 8). All STSCL part can be bypassed by proper setting of 119^{th} global configuration bit (*SCL TIME EN*, table A.2).

Configuration

At the beginning of any operation, the chip has to be proper configured. For this purpose, each channel contains a 24-bit configuration register (table A.3.) for the configuration of the analog and the digital channel part. Besides this, the chip contains a 144-bit global

configuration register (table A.2) for the settings of the global chip behavioral as well as the output peripheries. All configuration registers are connecting all together and act as one shift register. Therefore, to avoid the configuration bits having an undefined value during the configuration process, the default values are set while the *cnf_en* input is in active state. For both the global and the channel part all default values are set to the zero state. For the future development, it would be more appropriate to latch the previous configuration bits during the configuration to avoid the changes during and after configuration for the unchanging bits.

The input and the output data for the global and the channel shift registers are loaded by *data_in* serving as input and *data_out* as output. The data is loaded on the positive edge of the signal *clk* and the active *cnf_en* input. The configuration is described in timing diagram 6.5. After the configuration, the initialization sequence follows.

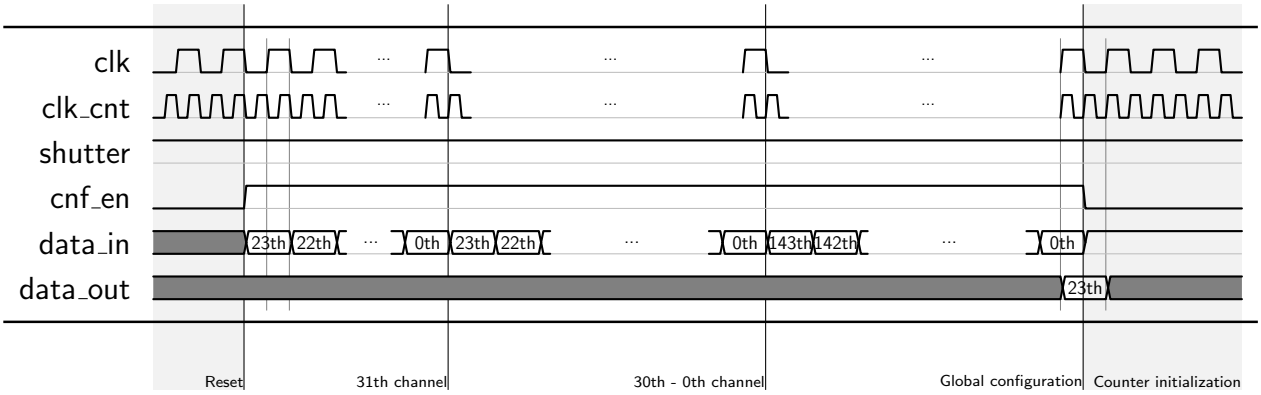

Timing diagram 6.5: The configuration of the PH32v6 chip.

Initialization

The counting register operates as an asynchronous counter, therefore it has to be initialized to the high state. Immediately after the chip configuration, the initialization of the counting registers can start. One channel contains a 16-bit shift register. All 32 channels in series contain 32×16 bits of the shift register, therefore 512 bits have to be initialized to the high state. Bits from 511^{th} to 0^{th} in timing diagram 6.6 are in the state '1'. After the initialization of the last 0^{th} bit, the *data_out* output drives '1' and the counting mode can follow.

Counting mode

The PH32 chip can operate in four operation modes which were already described (table 6.2). The one channel can process either the hit occupancy information, the charge deposited by the arrival particle, or count the particle arrival time. All information is store

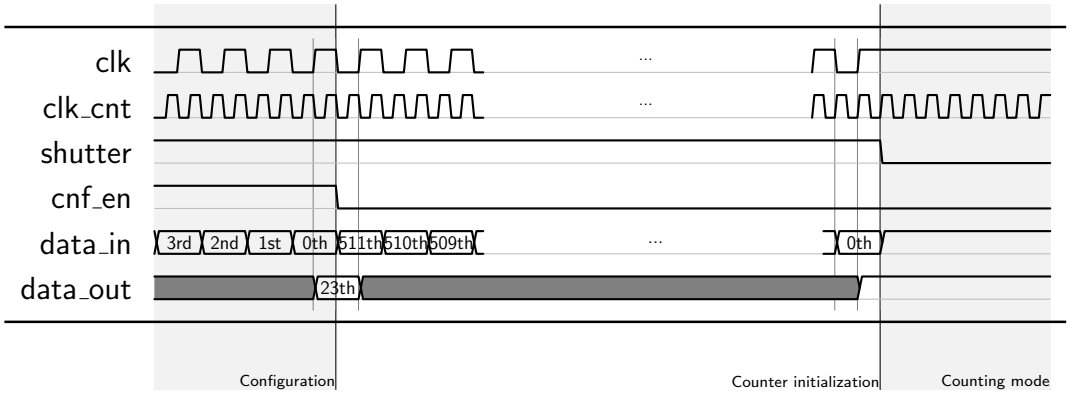

Timing diagram 6.6: The counter initialization in the PH32v6 chip.

in the 16-bit asynchronous counter inside the digital part of each channel. The processing of that digital part is triggered by a signal *shutter* while signal *clk* is in a high state (timing diagram 6.7). To prevent the lost of the energy information during the energy measurement of the first arrival hit, the internal signal *shutter_sync* can wait until there is no occupation at any channel as was already described above.

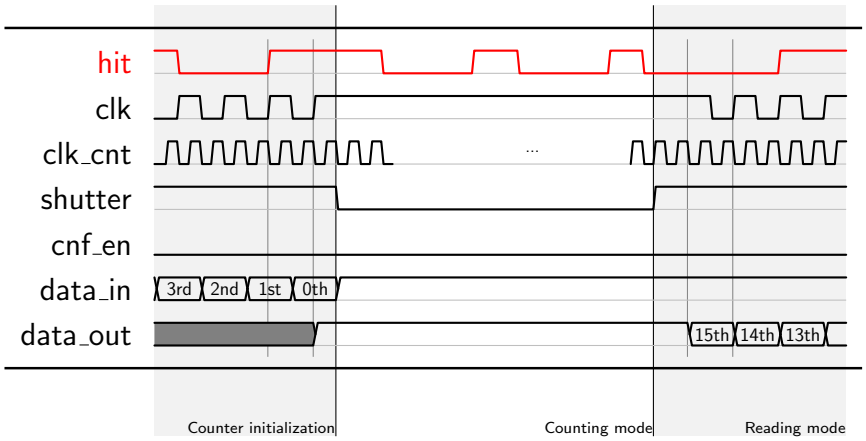

Timing diagram 6.7: Counting mode in the PH32v6 chip.

A description of the functionality of the signal shutter should be extended at this point about a shutter shifter feature which brings a novel approach for avoiding the cross-talk which come from the digital activity at the PCB during the measurement. Exactly, the source of the cross-talk is in the signal *shutter*, which affects the CSA input in the analog part of the channel. To avoid the cross-talk, the programmable delay for the internal shutter (*shutter_int*) can be applied. The shutter delay is organized by 121^{th}–122^{th} global configuration bits (*shift_div*) together with the 123^{th} enable bit (*shift_en*, table A.2). The programmable delay is derived from the clock period of the signal *clk_cnt* which is multiplied by values {2048, 4096, 8192, 16535} according the configuration bits. The mechanism of the mentioned crosstalk is described afterwards in following chapter.

Reading mode

Immediately after the finish of the counting mode, the reading mode follows (timing diagram 6.8). The data from the shift register of all channels is read by the *data_out* output on the positive edge of the clock signal *clk*. The PH32v6 chip is SPI compatible.

In the reading mode, the *data_in* input signal has to be in a high state, due to the initialization of the asynchronous counter to a high state. This process ensures the readiness of the next measuring period described above.

The first bit presented on the signal *data_out* immediately after the signal *shutter* has swapped into a high state (finishing of the counting mode), is the last 15^{th} bit from the last 31^{th} channel. Then, all the other bits from all channels in the total amount of 32×16 bits follow. Right after the reading of the 0^{th} bit of the 0^{th} channel, the counting mode can start again by forcing the signal *shutter* into a low state.

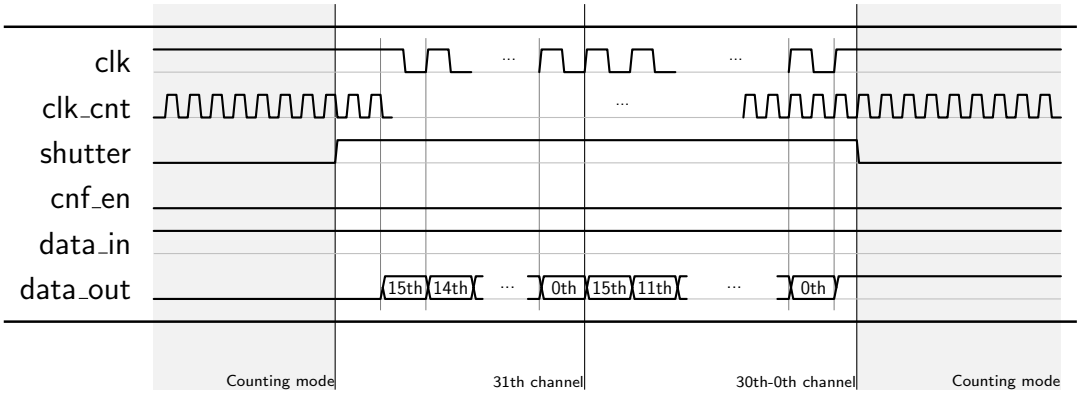

Timing diagram 6.8: Reading mode in the PH32v6 chip.

The above discussion is a complete description of the chip itself, which gives us an overview of the possible use of the PH32 chip when measuring the radiation dose or the energy of the deposited radiation particles or the arrival time of the flight. The following chapter discusses the main issues that ASIC designer had to challenged and which led to many iterations during the chip development.

Chapter 7

Hardware limitations

This section describes the major changes applied into the chips produced during the chip development period due to certain malfunctions, lower performance in compare with prediction or due to new demands. However there are hardware issues or some limitations still actual for last produced PH32v7 chip which are described below as well.

7.1 Cross-talk between digital activity of counters and the CSA output

The first important change came with a revision of the channel counter. Since the PH32v5 chip contains the asynchronous counter that is described in previous sections, the PH32v4 contains the 13-bit pseudo-counter (Fig. 7.1). In this case, data from measurement for each

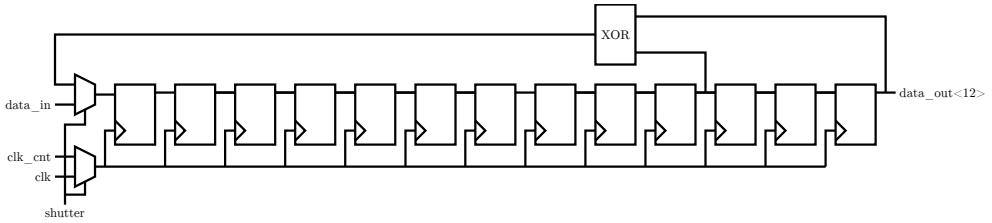

Figure 7.1: 13-bit pseudo counter.

channel are stored in 13-bit shift register which acts as a pseudo-random counter to enable serial read and write. An exclusive-OR operation is performed between 9^{th} and 12^{th} bit and the result is sent again as input to the first bit. For the proper functionality of the pseudo-random counter it has to be initialized to 8191 ("1_1111_1111_1111"). After that pseudo-counter changes its value pseudo-randomly to maximum value 8000 ("0_1111_1111_1111") with positive edge of reference clock. The maximum value represents a overflow which is controlled by appropriate circuit in every channel separately. In summary the ToT conversion resolution is 8000. The conversion table is not included in this thesis due to large amount of values.

The major issue is cross-talk between digital power rails and a substrate which is common for analog part also. For that purpose the power rails for analog and digital part are separated, however this effect is still presented and strongly significant. The CMOS 180 nm technology offered by AMS foundry for MPW used for PH32 chips does not allow more sophisticated partitioning. The triple-well option is available only for engineering run but for step-by-step development is not possible to think about it.

The measurement describing the cross-talk between digital activity of the pseudo-random counters and the output of CSA in analog part is shown in Fig. 7.2. The chip was

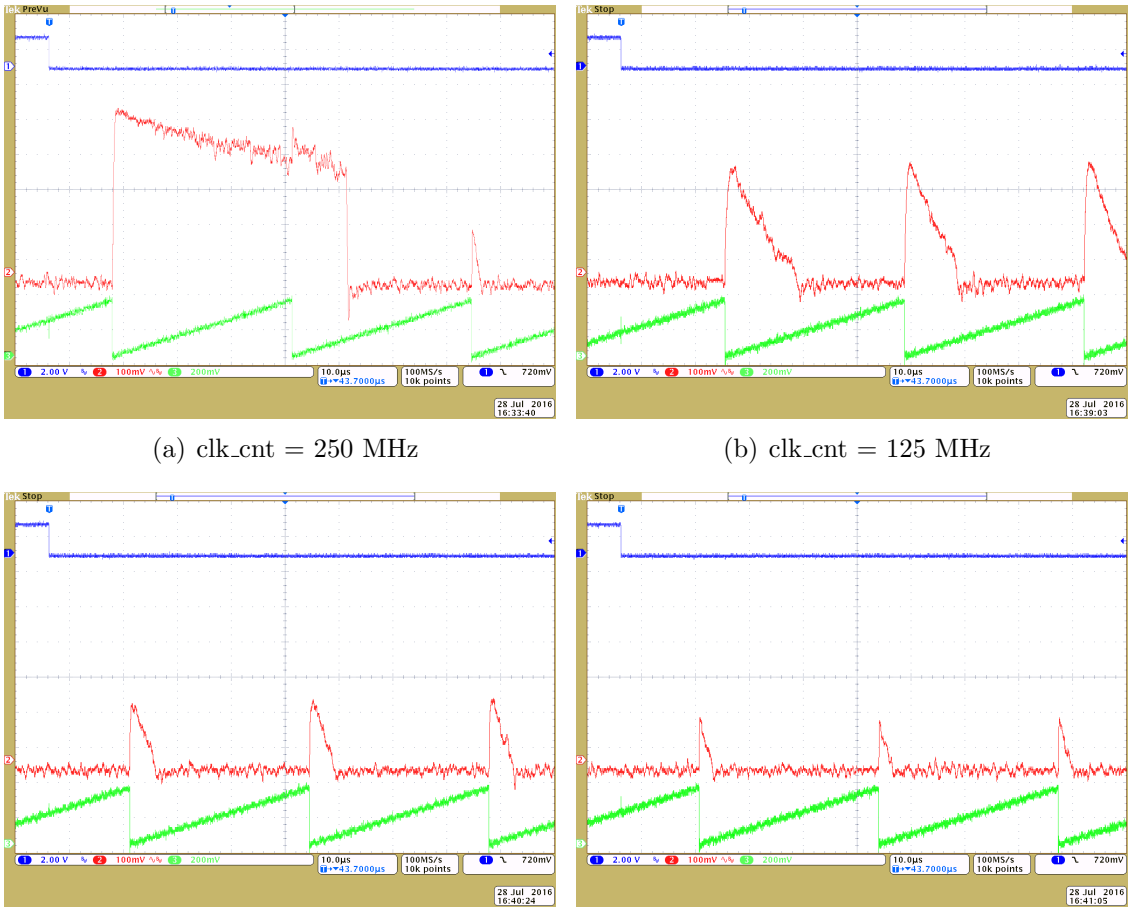

(a) clk_cnt = 250 MHz

(b) clk_cnt = 125 MHz

(c) clk_cnt = 62.5 MHz

(d) clk_cnt = 31.25 MHz

Figure 7.2: The cross-talk between digital and analog part. The PH32v4 chip is operated in HG and *energy integration* mode with sampling frequency 250 MHz. Channel one represents the *shutter*, channel two represents the output of CSA and channel three represents the injection of charge 18.7 ke$^-$ (300 mV). The cross-talk is most significant for not divided internal clock frequency and is less significant by lowering the frequency by internal divider.

operated in HG and *energy integration* mode with internal sampling frequency 250 MHz. The main issue for the recovering of the CSA circuit consists with not-resuming the output

of the CSA by feedback capacitor. The cross-talk is most significant for not divided internal clock frequency and is less significant by lowering the frequency by internal divider. One can observe that second peak of CSA output at sampling frequency 250 MHz (7.2(a)) is not affected. It is due to internally finished measurement due to overflow control which acted for high sampling rate. This specific peak of the CSA output is the only one which is not affected by described cross-talk and can be used as ideal output for comparison purpose.

The pseudo-counter register is great solution mainly of area limited design but its power consumption is relatively high. If very high integrity is required then the use of pseudo-random counter is one of the best solution. The lowering of sampling frequency inside the PH32 chip causes the lowering resolution which lead to worse resolution of energy spectrum and to less precise measurement of arrival time of particle. The hit-counting mode is affected by lowering of the clock frequency as well because PH32 chip contains the synchronization at the input to the digital part to avoid metastable state and can increase the deadtime. However this functionality seems to be not required as was not implemented for the PHpix chip (see section 10.2) [A.13] with no internal oscillator and this chip is working without any observed metastable issues till now.

All these disadvantages have led for replacing the pseudo-random counter by asynchronous counter which can act as shift register as well and was described in detail earlier. The use of this topology is novel approach for the detector of ionization particle. The schematic of asynchronous counter is shown in Fig. 7.3.

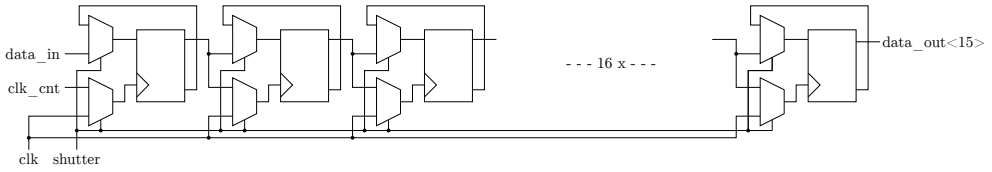

Figure 7.3: 16-bit asynchronous counter which can react as shift register as well.

The asynchronous counter with 16 registers has been used for first time in the PH32v5 chip what allows to count till maximum value of 65535. That means much greater possibilities for the PH32v5 chip in compare with its predecessors. The one reason why the greater counter has been designed was not space limited design also. The asynchronous counter offers advantage with respect to the power consumption not only because of lower average consumption but the current peaks are spread out in time also with these solution in compare with pseudo-counter. The measurement in HG and *Energy integral* mode with sampling frequency at 250 MHz by the PH32v5 chip does not indicate the same cross-talk behavior as the measurement by the PH32v4 chip (Fig.7.2).

The simulation results of the power consumption of the pseudo-random and asynchronous counter are more described in appendix B. From that results one can summarize that the average power consumption of 13-bit pseudo-random counter for *configuration* is 140 uW and for hit-counting mode is even slightly higher 170 uW. From the simulation of the 13-bit asynchronous counter (Note that 16-bit counter is used in the PH32v5 chip and its followers) is visible that the power consumption is much lower than for pseudo-random

counter. The average power consumption for *configuration* is 180 uW which is even higher in compare with pseudo-counter but for our requirement it is not relevant. For hit-counting mode the power consumption is 60 uW what is almost one third of the power consumption of the pseudo-counter. This novel solution solved the issue about cross-talk between digital activity of channel counter and the output of CSA in the analog part of the chip and has been proven even for higher sampling frequencies. However, as is described later, the digital activity of the channel counter still causes other several problems related into the cross-talk to the analog part as well.

7.2 Cross-talk between daughter board and the analog inputs

The PH32 chip is placed at daughter board PCB to allow communication with the chip and connect silicon sensor to the chip by wire-bonds (Fig. 4.1, Fig. 4.2, Section 4). Any digital activity at the daughter board during hit-counting mode (during measurement) may cause the cross-talk between external activity and the analog part of the chip due to infiltration of the signal originate from digital signaling to the output of the CSA.

7.2.1 Shutter

The most significant issue is caused by the signal *shutter* during triggering of measurement. The hit-counting mode starts on the negative edge of the *shutter* and finishes on the positive edge of this signal. The cross-talk between the signal *shutter* and the output of the CSA is more important at the beginning of the measurement mainly in *Energy of first hit* mode which can lead to detection of fake hit and to wrong evaluation of the hit energy. However the error is important for other operational modes but this behavior can be predictable and reflected during the post-processing.

Fig. 7.4 shows the measurement which represents the cross-talk between the signal *shutter* and the analog output of CSA. The chip was operated in HG and *Energy integration* mode with internal sampling frequency at 250 MHz. The waveform clearly shows the fake output response which is originated in the signal *shutter*.

These issues led to development of the novel concept for shutter triggering where the external digital signal *shutter*, needed for triggering of measurement, can be shifted in time and trigger the measurement with appropriate delay internally. The block called *Shutter shifter* contains the programmable delay block (Fig. 6.8, Section 6.2.2). The programmable delay is related to clock period of sampling frequency (the signal *clk_cnt*) which is multiplied by values {2048, 4096, 8192, 16535} according configuration bits. The behavior of programmable delay block and its impact on elimination of the specific cross-talk has been proven during a number of measurements with the PH32v5 chip and its followers.

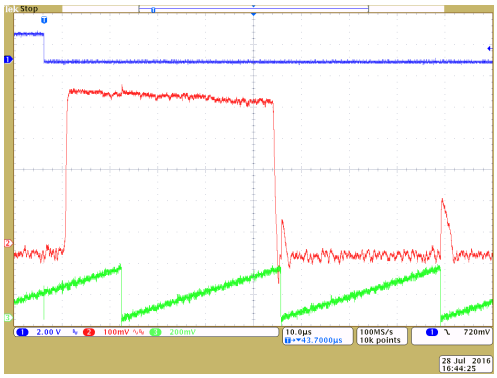

Figure 7.4: The cross-talk between the signal *shutter* and the analog output of the CSA. The PH32v4 chip is operated in HG and *energy integration* mode with sampling frequency at 250 MHz. Channel one represents the *shutter*, channel two represents the output of the CSA and channel three represents the injection of charge 18.7 ke$^-$ (300 mV).

7.2.2 Trigger

Some measurements of energy spectra or dose rate require the information about hit activity. This information can be used for triggering of external additional hardware to assist to the post-processing. However, any digital activity during measurement is very undesirable. For this purpose, the proprietary LVDS driver has been developed to drive the signal *hit_trigger* to avoid the cross-talk between digital activity at the daughter board during the measurement which caused the same issue related to the output of CSA as the signal *shutter* described above. The proprietary differential driver is fully configurable by global configuration register and is described in more detail in section 6.2.2.3. The trigger output is especially useful for the ToA measurement which is detaily described in later section 8.3 [A.19].

Besides these two digital communications are several other possibilities for the analog degradation. One of them is inappropriate possibility to use the PLL driving the internal clock from an external one or directly an external clock due to strong sensitivity of any digital signaling during the exposure caused by crosstalk to the CSA input through wirebonds, what is described in following sections as well.

7.3 Cross-talk between digital activity and the internal oscillator

The PH32 chip has report some hardware limitations and issues, which were resolved during the chip development. However, as usual, the solution of any difficulty leads to arising of new ones. Searching for any possibility how to improve the resolution and the stability of the detection system, led me to investigate the stability of the sampling frequency. The PH32 chip allows two relevant option how to measure the internal oscillator. One is usage of internal channel counter or global STSCL counter to evaluate the time of current exposure. There should be one fulfilled condition which is the threshold set under the baseline of the CSA output. The issue is, that during measurement several dependencies as shutter uncertainty or quantization error are apply to the result. The

second way is usage of clk_256 output which provides divided sampling frequency. The measurement of the sampling frequency by this feature allows to know frequency of the internal oscillator not distorted by surrounding hardware. However, one has to know that this measured frequency is average frequency for the period of 256 clocks. As will be seen at appropriate measurement the internal oscillator is strongly dependent on its power (Fig. 7.5). Therefore, all measurements belonging to the VCO behaviour are done with maximum value of VBIAS (1.8 V) which has the lowest frequency derivative to the oscillator power.

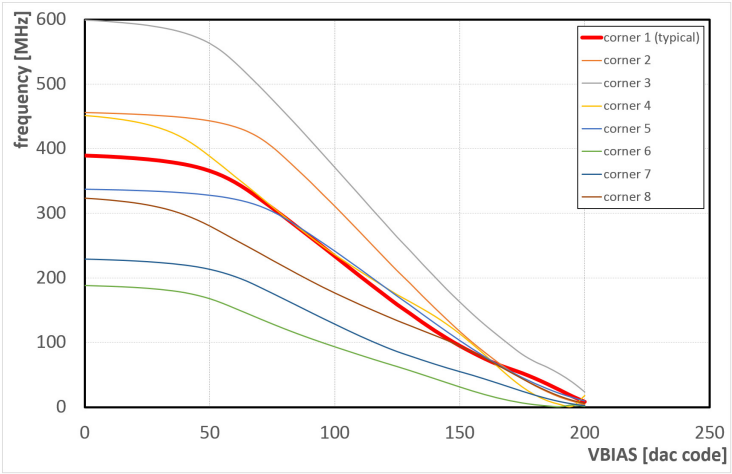

Figure 7.5: Transfer function of the voltage controlled oscillator at several process corners.

Fig. 7.6 shows the internal oscillator response on various clock divider and operational modes measured by PH32v6 chip with maximum frequency at 333 MHz. For all measurements, the injection of charge 1.9 Me^- was applied in the time 4 ms after exposure start. The measurement represents various dependencies to the consequent sampling frequency:

Shutter As was described above, the signal *shutter* is important source of the cross-talk to analog part. Presented measurement shows other type of influence - on the voltage controlled oscillator. It is obvious that the concept with the shutter shifter which allows to implement internally delayed shutter is important part of the chip.

Hit-counting mode This mode represents the lowest power consumption as the internal oscillator is used only for synchronization. The cross-talk is stronger for not divided frequency and is almost invisible for frequency divided by eight.

Time of arrival The ToA mode represents the highest power consumption what is clearly presented. The counter starts its activity 4 ms after exposure start and counts till the overflow. The overflow occurs around 200 µs after injection arrives for non divided sampling frequency. For the frequency divided by two the counter stops its activity after double time, etc. From the attached waveforms is visible that the strongest cross-talk is for non divided sampling frequency.

Static frequency It is obvious that the static power consumption leads to the changing of the sampling frequency indirectly in proportion.

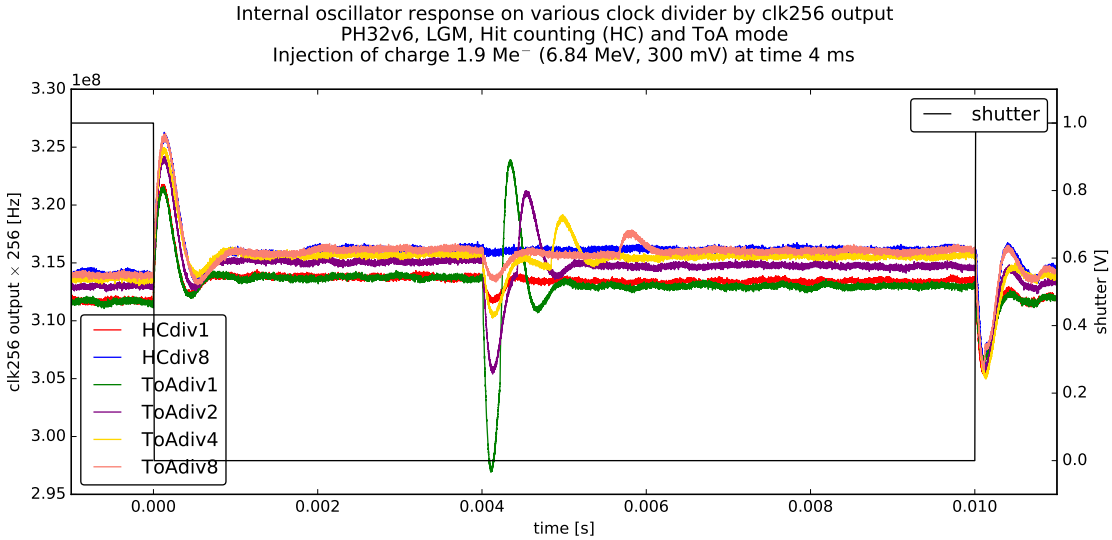

Figure 7.6: The internal oscillator response on various clock divider and operational mode by clk_256 output.

From these possible dependencies follows that the sampling frequency is related to the power consumption of the channel counters, to the digital activity of the external signals and to the injection itself. Last but not least the internal oscillator depends on *VCO_VBIAS* level as described in follows.

7.4 Cross-talk between digital activity and the global DACs

The PH32v6 chip contains the DAC_OUT output for direct measurement of the DAC level. The labor around the measurement of the sampling frequency described above, led to check the VCO_BIAS level. I found that the dependencies related to the changing of the sampling frequency is also related not only to the VCO_BIAS level, but also for all other DAC outputs. The following plots (Fig. 7.7, Fig. 7.8) present the measurement of the DAC output in the same meaning as the previous measurement of the sampling frequency. For both measurements, the injection of charge 3.7 Me$^-$ was applied 4 ms after the exposure start in the hit-counting and the ToA mode. Both measurements give the relatively similar results with one significant difference - the digital power has much longer transition phenomenon.

For both plots the one point is interesting. Some DAC outputs are connected directly to the transistor gates inside the channel and some are connected to the input of the transconductor which is represented by only one gate. From the plots is visible that the

DAC output which is connected to the more (tens) gates is much more stable than the output connected only to one gate. From the presented results it is evident that the DAC outputs have weak driver and even relatively strong capacity coupling is not enough to eliminate the relatively strong cross-talk.

The most important result from the presented measurements is the shifting of the digital power (VDDD) in the ToA mode. This shift (20 mV) causes the sampling frequency error of 2 % and it should be taken into consideration when measuring the energy of deposited charge or time of arrival.

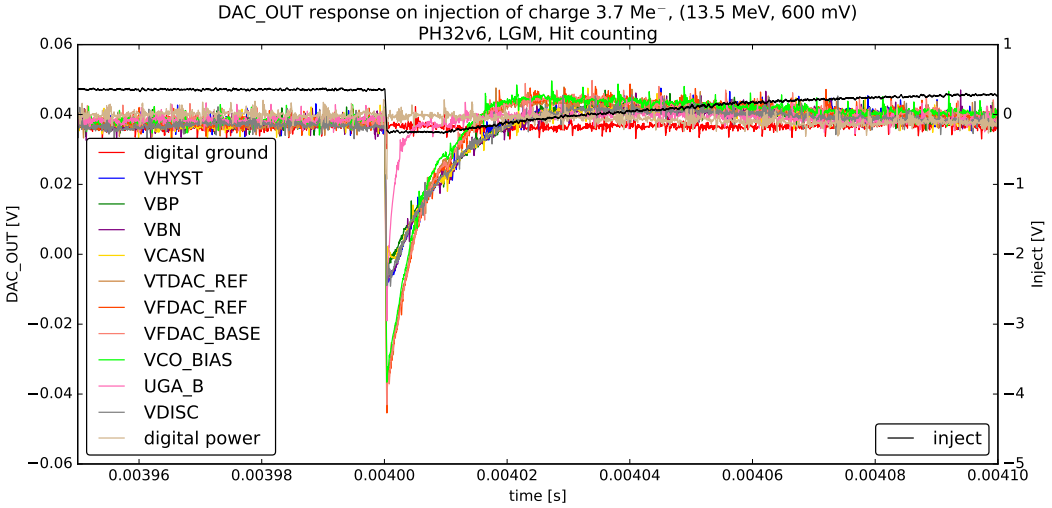

Figure 7.7: DAC_OUT response on injection of charge 3.7 Me-, i.e. 13.5 MeV (600 mV) for the PH32v6 chip operated in the LG and the hit-counting mode.

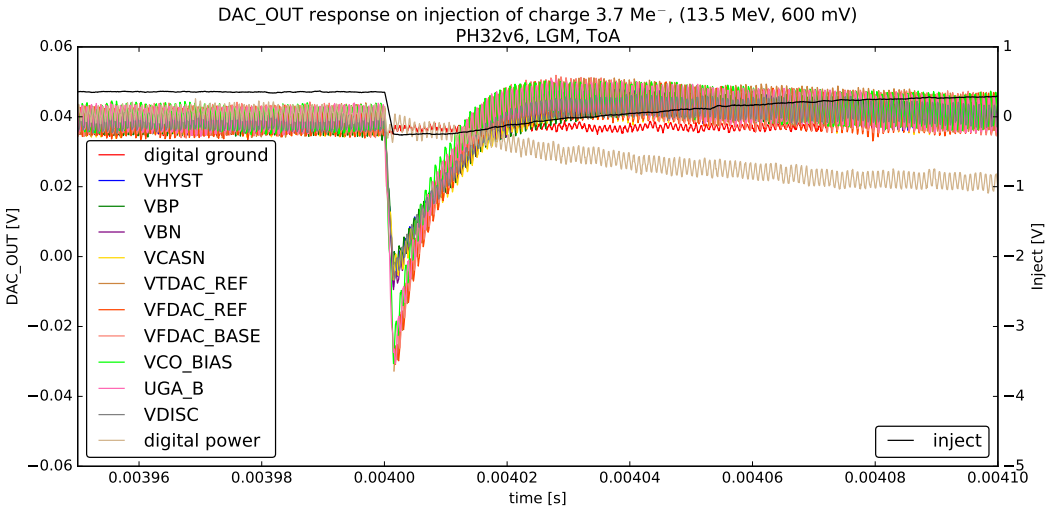

Figure 7.8: DAC_OUT response on injection of charge 3.7 Me-, i.e. 13.5 MeV (600 mV) for the PH32v6 chip operated in the LG and the ToA mode.

Chapter 8

Calibration and performance of detection system

8.1 Threshold tuning

The detection performance is closely related to the analog part of the chip. To obtain relevant data with respect to the noise, linearity, gain, dispersion between individual channels, etc., the analog part has to be calibrated. First, the threshold of discriminator for every channel has to be set closely over the noise. This is done by appropriate setting of the global Threshold DAC (TDAC) for all channels together with the local TDAC for every channel separately.

As a source of charge one can use a laboratory radiation source of known energy spectrum or injection of specific charge from an external injection circuit. For this reason the chips of the PH32 series contain the inject input with couple of AC coupling capacitors for both gain modes configured from local configuration as seen in Fig. 6.1.

At this point we encountered a serious issue. Since the chip version PH32v3 has the sensor connected to the chip with no possibility of electronic disconnection, the strong crosstalk between two neighboring sensor strips caused by inject signal was observed. More precisely, the inject signal is going through the input AC coupling capacitor to the CSA input and also through the sensor AC coupling capacitor to the strip. Thereafter, through the silicon to the neighbor strips and back through the AC coupling capacitors to the CSA input of another channel (Fig. 6.1). Actually, this disadvantage can not be eliminated by successive equalization when the chip tuning is running for every channel separately even. Besides the much longer equalization time during the step by step equalization, there is a dispersion results from the leakage of the injection signal to the sensor strip itself and also to the adjacent strips. Because of this the new feature of electronic disconnection of the sensor strip came with the chip version PH32v4. This section describes the threshold tuning provided by the chip version PH32v5, also focusing on the mentioned crosstalk.

Fig. 8.1 shows the threshold scan as a response to 1000 injections of charge 1 Me^-, i.e. 3.6 MeV for PH32v5 chip operated in LG mode, *Hit counting* mode and connected

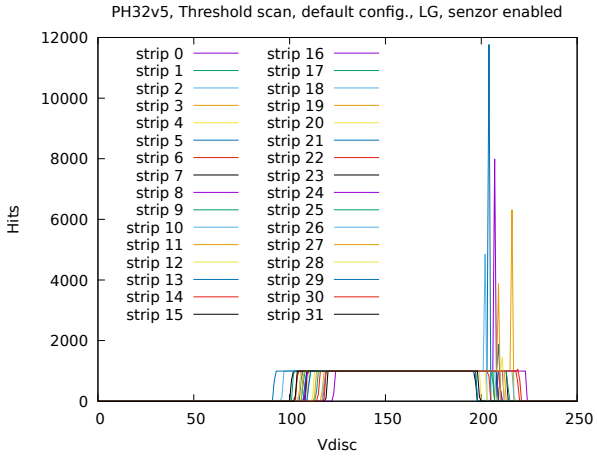

(a) The threshold scan with the default configuration

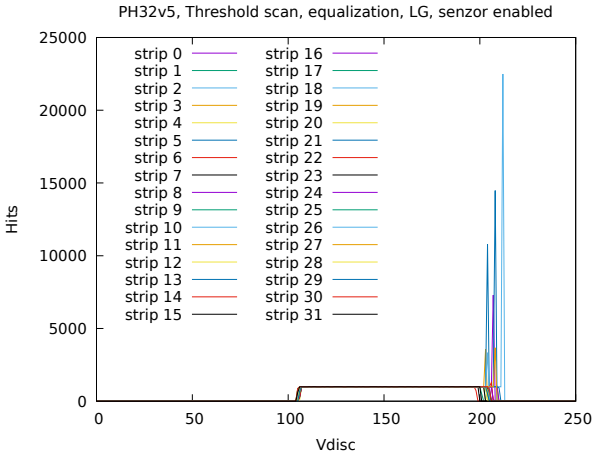

(b) The threshold scan after the equalization

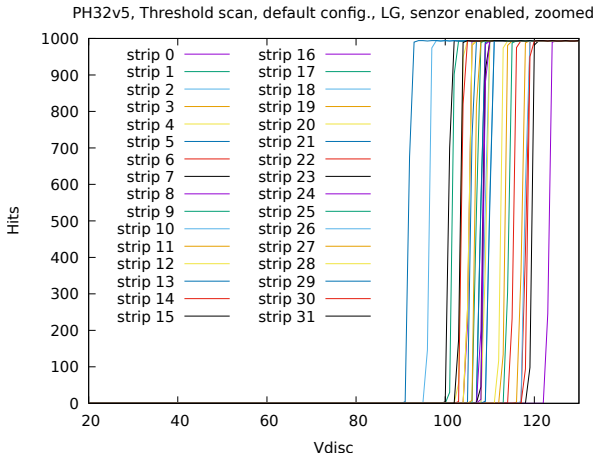

(c) The threshold scan with the default configuration. Selected area.

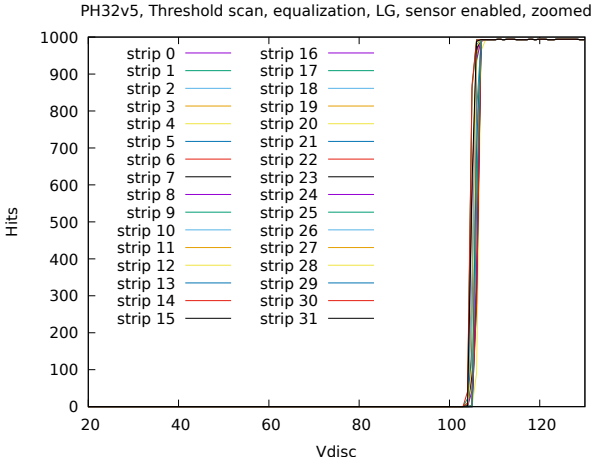

(d) The threshold scan after the equalization. Selected area.

Figure 8.1: Threshold scan shows the response to 1000 injections of charge 1 Me^-, i.e. 3.6 MeV for PH32v5 chip operated in LG mode, *Hit counting* mode and connected (enabled) to fully depleted sensor (bias = −150 V, 47 nA). Fig. 8.1(a) shows the response to injection for the chip operated with default TDAC configuration ($\mu = 109.38$, $\sigma = 6.85$, $\sigma/\mu = 6.28$ %). Fig. 8.1(b) shows the response to injection for the chip calibrated for a charge of 1 Me ($\mu = 106.06$, $\sigma = 0.61$, $\sigma/\mu = 0.57$ %). Figures 8.1(c) and 8.1(d) represent the selected area of interest.

to fully depleted sensor (bias = −150 V). The threshold scan was made before threshold equalization with default TDAC values. One can observe relatively high dispersion of the response to the injected charge (μ = 109.38, σ = 6.85, σ/μ = 6.28 %). The threshold calibration consists of finding the ideal local TDAC values to minimize the dispersion of the response to injection charge.

Fig. 8.1(b) shows the same threshold scan as Fig. 8.1(a) but after threshold equalization where the individual local TDAC values were used for each channel separately. One can observe that the dispersion of the response to the injected charge is much smaller than for not calibrated chip with default TDAC values (μ = 106.06, σ = 0.61, σ/μ = 0.57 %).

The LG mode due to its relatively low voltage gain is not as much sensitive as HG mode which has voltage gain higher by two orders (See Table A.1) and therefore the threshold scan is not as much different with respect to connected and disconnected sensor as threshold scan in HG mode.

Fig. 8.2 shows the differences between the threshold scan for HG mode with the PH32v5 chip without the sensor (internally disconnected by local configuration) and with the sensor connected to the chip and calibrated for a charge of 10 ke$^-$. Threshold scan shows the response to 1000 injections of charge 10 ke$^-$, i.e. 36 keV. Fig. 8.2(a) shows the response to injection for the chip with disconnected sensor and with relatively low dispersion (μ = 109.84, σ = 0.67, σ/μ = 0.61 %). In contrast Fig. 8.2(b) shows the same threshold scan but with sensor connected to the chip where one can observe the higher dispersion (μ = 114.00, σ = 1.64, σ/μ = 1.44 %).

One should know that the described crosstalk was not totally resolved by sensor disconnecting ability which came with the PH32v4 chip. Even with disconnected channel one can observe the signal coming to the CSA input during the injection. The signal was observed by analog_out output (Fig. 6.8). Just two possible explanation came: first, the analog switch not provide sufficient resistivity to block path, or more likely there is another kind of crosstalk between each individual chip channels during the charge injection. However this is not as big issue as other observed occurrences. Following section describes the second step during the chip equalization. All discussed results are for the sensor disconnected or disabled from the CSA input.

8.2 CSA output tuning

The second step contains the feedback current tuning to obtain linear output of the CSA for the wide range of charge. This is done by appropriate setting of the global Feedback DAC (TDAC) for all channels together with the local FDAC for every channel separately.

The previous section explained distinctions between connected and disconnected sensor to the CSA input. Is clear that any tuning or equalization processes inside the chip should be make with the chip separated from outer world. For this reason the PH32v4 chip contains the analog switch which enable the electric disconnection of the sensor strip from the CSA input. And therefore, the following presented results regarding to the CSA output tuning are with disconnected or disabled sensor only.

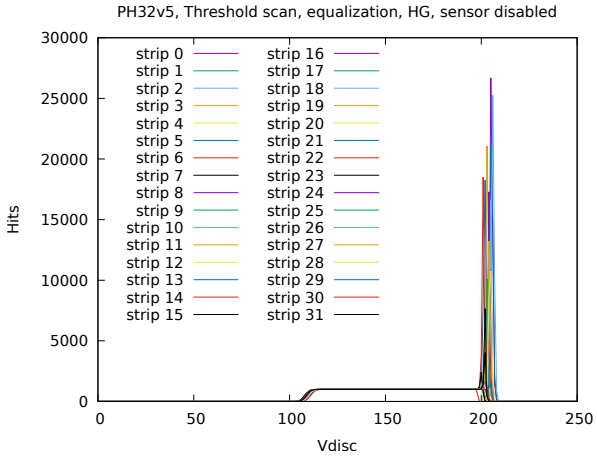

(a) The threshold scan after the equalization without a sensor

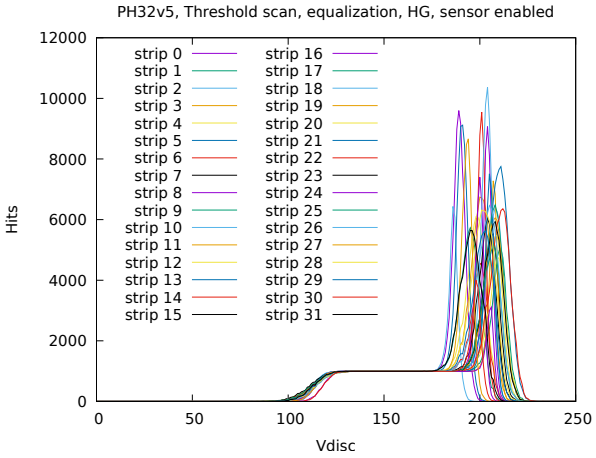

(b) The threshold scan after the equalization with a connected sensor

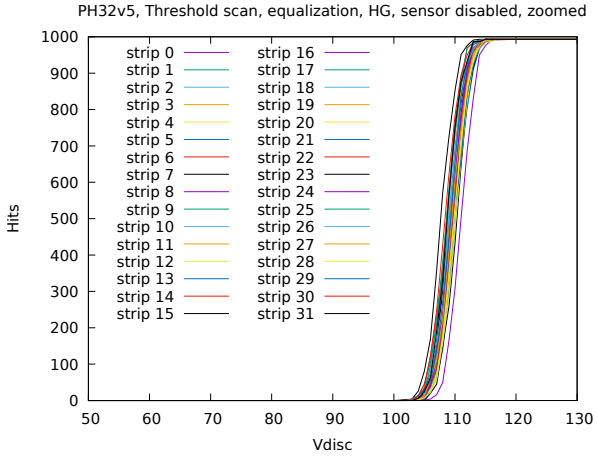

(c) The threshold scan after the equalization without a sensor. Selected area.

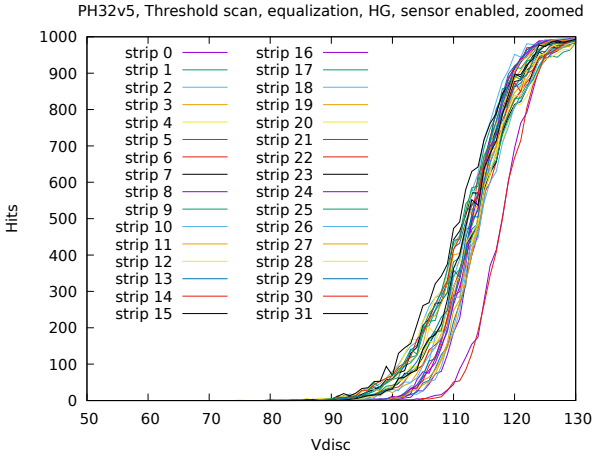

(d) The threshold scan after the equalization with a connected sensor. Selected area.

Figure 8.2: Comparison between disabled and enabled sensor (fully depleted, bias −150 V, 47 nA) to the PH32v5 chip operated in HG mode, *Hit counting* mode and calibrated for a charge of 10 ke$^-$. Threshold scan shows the response to 1000 injections of charge 10 ke$^-$, i.e. 36 keV. Fig. 8.2(a) shows the response to injection for the chip with disconnected sensor ($\mu = 109.84$, $\sigma = 0.67$, $\sigma/\mu = 0.61$ %). Fig. 8.2(b) shows the response to injection for the chip with connected sensor ($\mu = 114.00$, $\sigma = 1.64$, $\sigma/\mu = 1.44$ %). Figures 8.2(c) and 8.2(d) represent the selected area of interest.

A relevant evaluation of the equalization is provided by ToT measurement. Fig. 8.3 demonstrates the ToT measurements as a result of 1000 injections of the charge 30 ke$^-$ to all channels at the same time. The PH32v4 chip with disabled sensor was operated in HG mode and the sum of the ToT values from all channels are for the chip calibrated at 30 ke$^-$. Firstly, by threshold tuning only and secondly, by threshold and feedback calibration. Is

clearly visible that the channel dispersion causes the significant error and therefore the feedback current calibration is necessary for appropriate energy measurement also.

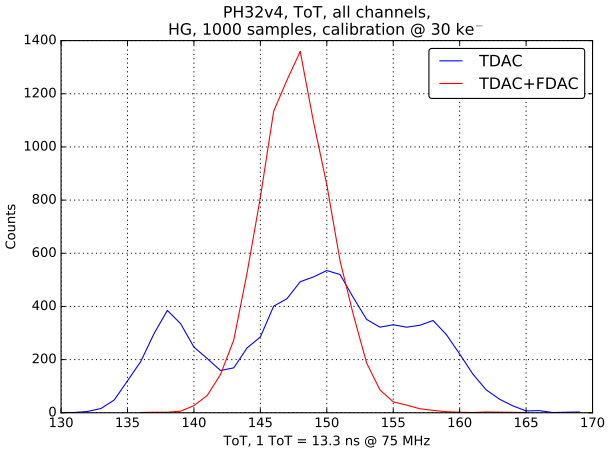

Figure 8.3: The ToT response to 1000 injections of the charge 30 ke$^-$ in HG mode. The PH32v4 chip was calibrated at the same injected charge. Each individual mean value of the ToT represents the sum of the signals from all channels. Shown results are for the chip calibrated to the discriminator threshold and to the threshold together with the feedback current tuning. The channel dispersion causes the significant error and therefore the feedback current calibration is necessary for the energy measurement.

All following graphs in this section are for the chip already calibrated to the threshold and the feedback current.

Fig. 8.4 represents the comparison between disconnected sensor (PH32v3, [A.9]) and connected but disabled fully depleted sensor (PH32v4, [A.10]) for the chips operated in HG and LG modes and *First hit energy* mode. Is clearly visible that the resolution for HG mode is much lower with the newer version of the chip with connected but disabled sensor. As was described in previous section, the switch for disconnecting the sensor from the chip is not totally separating the sensor connectivity to the CSA input. Other problem arose, as the minimum discriminator threshold can not be reduced under the noise, and therefore the charge is not applied under 7 ke$^-$ for the PH32v4 in HG mode. This disadvantage was removed by newer PH32v5 chip version. Besides those attributes the newer PH32v4 chip demonstrates the higher linearity for both operational modes as well as the higher resolution, specially for LG mode. This applies also for HG mode but this demonstration is the comparison between disconnected and disabled sensor and therefore the results have to be taken relatively.

The description of the ToT measurement would not be completed without the demonstration of the performance belonged to the last measured version of the chip PH32v6 [A.19]. Fig. 8.5 represents the ToT response to 1000 injections of charge varying from 3.1 ke$^-$ to 37.5 ke$^-$ (HG) and from 310 ke$^-$ to 3.75 Me$^-$ (LG) for the PH32v6 chip. From the stated results is evident that the last measured version of the chip has significantly more linear and higher precision results compared to its predecessors. This is done mainly due to the improvement of the analog part and the reduction of the digital crosstalk implemented into the chip version PH32v5. All significant differences between the chip versions are described above (section 6.2, table 6.1). Besides all mentioned improvements, the significant noise lowering from ≈2.2 ke$^-$ (PH32v3) and ≈5.8 ke$^-$ (PH32v4) to ≈970 e$^-$ is presented also.

At this point should be mentioned once again that the thesis is focused on the performance of the chip PH32 and one should be conscious that all presented results are very

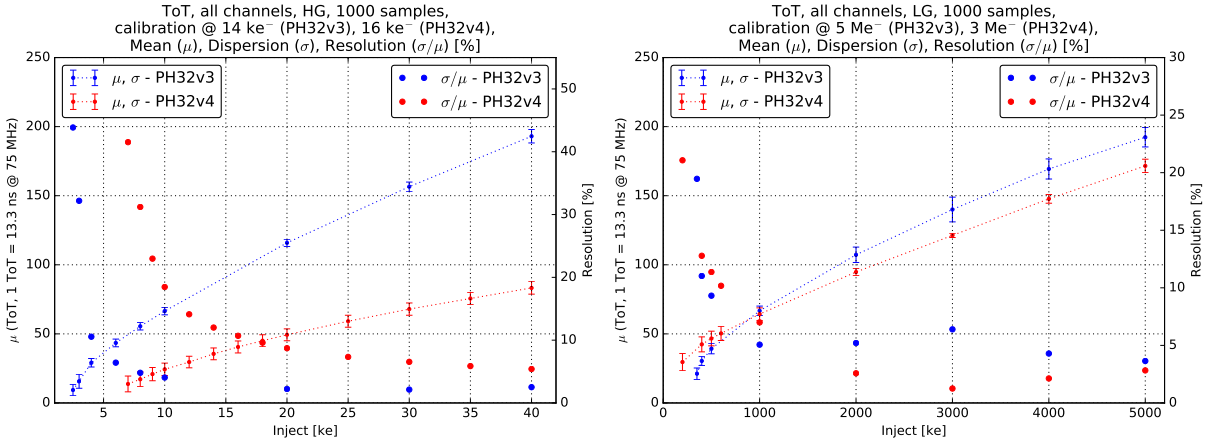

(a) HG mode (b) LG mode

Figure 8.4: Comparison between disconnected sensor (PH32v3, [A.9]) and connected but disabled fully depleted sensor (PH32v4, [A.10]) for the chips operated in HG and LG modes and *First hit energy* mode. Fig. 8.4(a) shows the response to 1000 injections of charge varying from 2.5 ke⁻ (PH32v3) and 7 ke⁻ (PH32v4) to 40 ke⁻ for the chip calibrated for a charge of 14 ke⁻ (PH32v3) and 16 ke⁻ (PH32v4) in HG mode. Fig. 8.4(b) shows the response to 1000 injections of charge varying from 0.35 Me⁻ (PH32v3) and 0.2 Me⁻ (PH32v4) to 5 Me⁻ for the chip calibrated for a charge of 5 Me⁻ (PH32v3) and 3 Me⁻ (PH32v4) in LG mode. Each individual mean value of ToT represents the sum of signals from all channels.

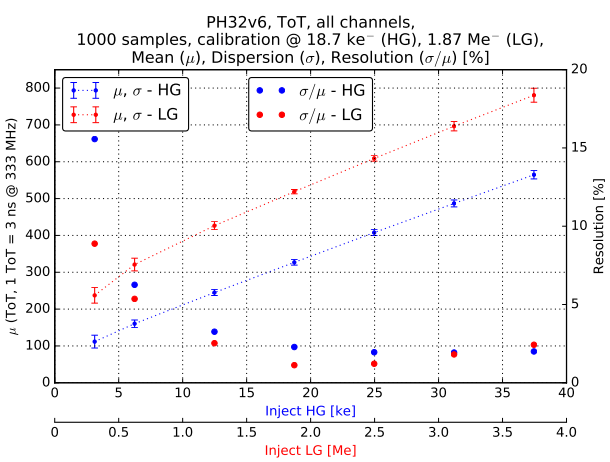

Figure 8.5: ToT response to 1000 injections of charge varying from 3.1 ke⁻ to 37.5 ke⁻ (HG) and from 310 ke⁻ to 3.75 Me⁻ (LG). The PH32v6 chip was calibrated at two different injection charge. Each individual mean value of ToT represents the sum of signals from all channels. The PH32v6 reports significantly more linear and higher precision results compared to its predecessor. Besides, significant noise lowering from ≈2.2 ke⁻ (PH32v3) and ≈5.8 ke⁻ (PH32v4) to ≈970 e⁻ is presented also.

tightly connected to total detection system. Therefore the family of the PH32 chips should be at least the subject to evaluation also with other types of the sensor (lower capacitance, higher detection performance for lower energies, etc.).

8.3 Time of Arrival mode

The above described calibrations were done in *First hit energy* mode by Time–over–threshold (ToT) method. To fully understand the performance of the PH32 chip, one has to be familiarized with the Time–of–Arrival (ToA) and Time–of–Flight (ToF) mode which is measured by last operational mode called *Time of arrival of the first hit* (section 6.2.2.2, table 6.2). This functionality allows use the chip for particle tracking or ion mass spectroscopy measured by individual channel, trigger output and global STSCL counter. These functional approaches are detaily described in section 6.2.2.

The aim of discussion in this part is fully understand detection performance of the PH32 chip not only in ToA (ToF). The following presented results (refer in [A.19]) are greatly important for other operation modes as well and present an addition to hardware limitations which are already described above in section 7.

Fig. 8.6 shows the measurement setup dedicated to examine the ToA and the ToF functionality. There are two approaches for testing. First, the ToA is measured by charge injection, to examine the chip functionality only. For this purpose sensor is disabled as well as no light emitter is needed. Second, the ToF is measured by laser diode, to demonstrate the ability of realistic time–of–flight measurement.

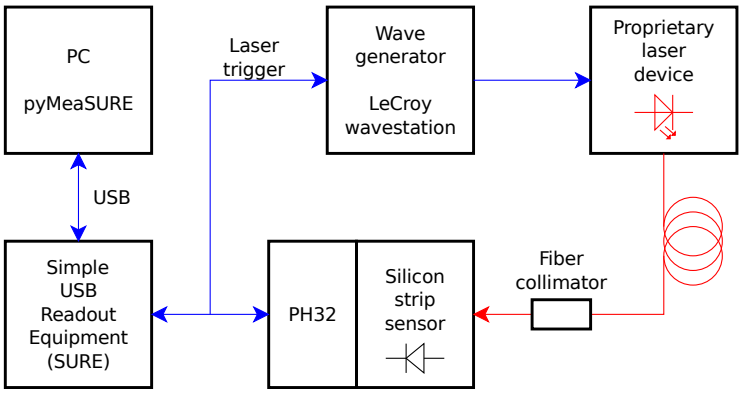

Figure 8.6: The measurement setup to examine the ToA functionality by charge injection and the ToF functionality by laser equipment.

For both methods, the time information is derived from an adjustable internal voltage controlled oscillator which can be set in the range from tens to hundreds of MHz. A time-stamp is stored in a 16-bit asynchronous counter for every channel separately, which can be read as a shift register from all channels after exposition. The internal oscillator is a significant source of the dispersion between hit occurrences as it varies in time mainly due to the crosstalk caused by digital activity of the channel counter and the shutter toggling. Since the chip version PH32v5, the chip contains also a 40-bit synchronous counter designed in STSCL which can be used for the time measurement triggered by an internal trigger

derived from all channels. This method of the time measurement can be efficient only for low dose rate, because only the first hit from all channels is detected. However, the chip using this functionality can operate in Energy measuring mode instead of Time of arrival mode and the time-walk effect may be corrected. The following sections present correlation between the time functionality measured by all channels with the channel counter, by one 40-bit synchronous counter and the energy measurement for every channel separately. The internal trigger used for triggering of STSCL logic is also propagated to the output for triggering the external hardware (The triggering is described in section 6.2.2.3). The output is realized as proprietary differential signaling to avoid crosstalk between the digital output at PCB and the wire-bonding between the sensor and the chip. Therefore, the next sections also compares the time measurement results provided by the individual channel counter with the trigger output.

8.3.1 Time of arrival by charge injection

Before any measurement, the equalization of the chip has to be performed to obtain relevant data with respect to the noise, linearity, gain, etc and therefore the calibration of the chip should be done in the same meaning as was described above. The measurements presented in this section are focused on the channel response to the injected charge including channel dispersion and the time-walk effect measured with variety of the injected charge. All measurements were done with the sensor connected to the chip, but disabled by local channel configuration in the same meaning as during the equalization process.

8.3.1.1 16-bit asynchronous counter

Fig. 8.7 represents the ToA measurement for already calibrated chip as a response to 1000 injections of charge varying from 3.1 ke$^-$ to 37.5 ke$^-$ (HG) and from 310 ke$^-$ to 3.75 Me$^-$ (LG). This measurement shows the expected time-walk effect for both operational modes. The overall ToA resolution (σ/μ) is 0.2% for HG mode and 0.18% for LG mode and includes the time-walk effect, the channel dispersion, the fluctuation of sampling frequency and the shutter time uncertainty.

As was described above in section related to the hardware limitations (section 7), the fluctuation of sampling frequency is significant source of the error. To minimize the frequency influence, the biasing of the internal oscillator should be set to maximum value (section 7.3). Therefore, all ToA and ToF measurements were done with maximum frequency at around 333 Mhz. Fig. 8.8 demonstrates specifically the fluctuation of the sampling frequency during eight consecutive frames. One can observe that the error for one frame is caused mainly by quantization error only. However, the error for more consecutive frames is caused mainly by frequency fluctuation. In absolute terms the sigma for one frame is around 1, whereas for eight consecutive frames is around 7 (0.4%).

We can state that longer exposition time leads to the more precision results due to averaging the sampling frequency. The following table 8.1 demonstrates the higher resolution for longer exposition time. These results were made by ToA measurements for two different

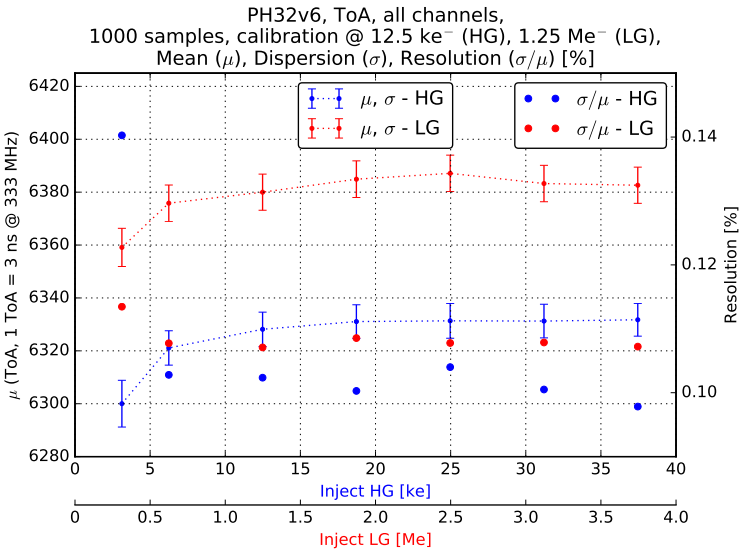

Figure 8.7: ToA response to 1000 injections of charge varying from 3.1 ke⁻ to 37.5 ke⁻ (HG) and from 310 ke⁻ to 3.75 Me⁻ (LG). The chip was calibrated at two different injection charge. Each individual mean value of ToA represents the sum of signals from all channels.

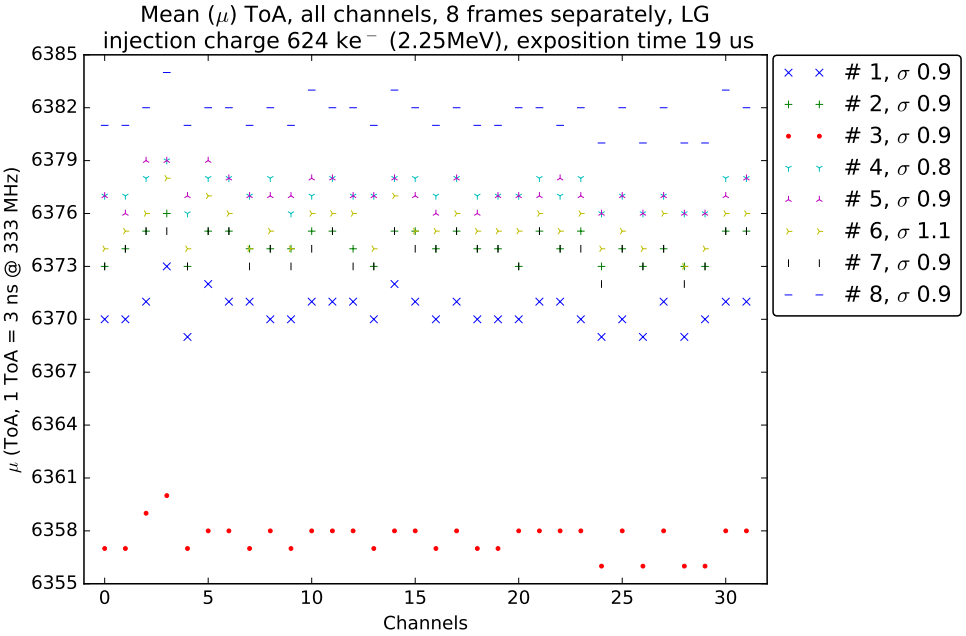

Figure 8.8: The fluctuation of the sampling frequency during eight consecutive frames in the ToA measurement. The error for one frame is caused mainly by quantization error only, but the error for more consecutive frames is caused mainly by frequency fluctuation.

exposure times by injected charge of 624 ke$^-$ in LG mode and for the chip calibrated at the same injection charge.

Exposure time [us]	Mean (μ)	Sigma (σ)	Resolution [%]
19	6379	11	0.18
190	62490	52	0.08

Table 8.1: The ToA measurements for various exposition times. Injected charge of 624 ke$^-$ was applied for the chip calibrated at the same injection charge and operated in LG mode. The mean and sigma values of ToA represent the sum of signals from all channels during 1000 exposures.

From these results is clear that internal oscillator causes the significant error and is the task for future chip development. The issue is even more important for the ToT measurement, where one can not apply the averaging the sampling frequency by prolonging the exposition time. The measurement related to this issue is also demonstrates in following plot.

Figure 8.9 represents the ToA measurement as a response to 1000 injections for various exposition time after inject arrival. One injection charge per both operation mode was chosen and as a result is linear response for all exposition times in a wide range for both operation modes. The precision is increasing by prolonging of the counting time due to averaging the sampling frequency which is the significant source of the error.

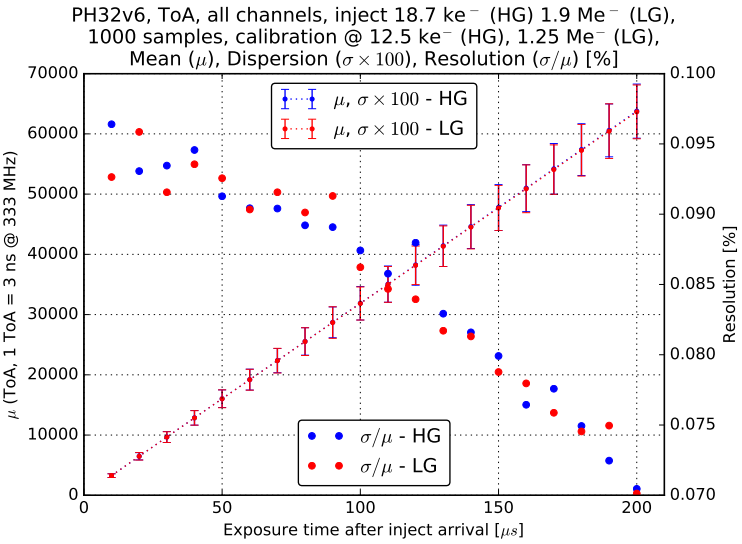

Figure 8.9: ToA response to 1000 injections for various exposition time after inject arrival. The injection charge is 18.7 ke$^-$ (HG) and 1.9 Me$^-$ (LG) and the chip was calibrated at 12.5 ke$^-$ (HG) and 1.25 Me$^-$ (LG). Be aware that the ToA values for HG and LG mode are lay over each other.

It is clear that the sampling frequency causes several problems. This issues comes from the cross-talk to the power of the VCO itself. One could object, why not to use external source of the sampling frequency or the PLL itself. The possibility to use the PLL driving the internal clock from an external one or directly an external clock is inappropriate due to strong sensitivity of any digital signaling during the exposure caused by crosstalk to the

CSA input through wire-bonds. In this state, usage of the internal oscillator seems to be adequate option.

8.3.1.2 Trigger driver

Figure 8.10 demonstrates the trigger functionality (described in section 6.2.2.3) which has two main useful advantages. Firstly, the information about the first arrival hit is useful for energy measuring when the exposition may be immediately stopped followed by data capturing and finished by the next exposition run. In this sense the energy measurement can be more effective, especially if a medium with low radiative decay is in use. Secondly, trigger is used for the ToA measurement, either only by the trigger output or together with the ToT measurement for the time-walk effect correction eventually. The plots represent a response to 10 injections of charge varying from 3.1 ke$^-$ to 37.5 ke$^-$ for HG mode and from 310 ke$^-$ to 3.75 Me$^-$ for LG mode. The dispersion is relatively low for both operation modes. Be aware that for the presentation purpose the dispersion is multiplied by 10^6 with an overall resolution (σ/μ) of time measurement for HG mode 0.024 % and for LG mode 0.026 %. The overall resolution includes clearly visible time-walk effect, the fluctuation of the sampling frequency and the shutter time uncertainty. The channel dispersion is excluded because only one channel was enabled during this measurement.

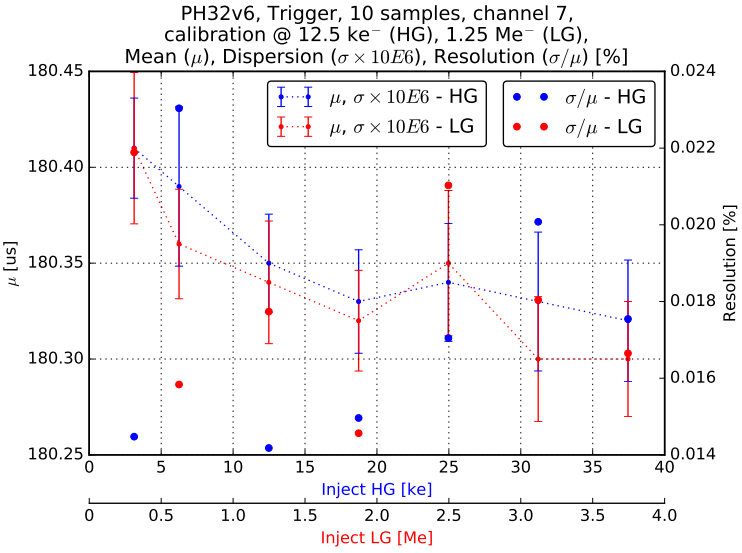

Figure 8.10: The trigger output response to 10 injections of charge varying from 3.1 ke$^-$ to 37.5 ke$^-$ (HG) and from 310 ke$^-$ to 3.75 Me$^-$ (LG) injected to the one channel. The mean value (μ) represents the time between exposure start and the trigger driver response measured by oscilloscope.

8.3.1.3 40-bit synchronous counter

Figure 8.11 demonstrates the ToA measurement provided by the 40-bit synchronous global STSCL counter in parallel with the ToT energy measurement (Fig. 8.12) with only one allowed channel. The aim of using the global ToA counter in STSCL technology is the reduction of the crosstalk between digital and analog part during digital activity while the chip is running in the exposition run. This allows to reduce the fluctuation of the sampling

frequency which is a significant source of the error. Secondly, lowering the sensitivity of Charge Sensitive Amplifier (CSA) to the fluctuation of digital power rails is also very important. The dispersion of the ToA measurement is relatively low, however it is about ten times higher than dispersion of the ToA measurement provided by the trigger output. In this sense the usage of the trigger output is more convenient. However, the trigger output needs additional processing by the external hardware while the global ToA counter provides final time-of-arrival information. Last but not least, the global counter may be reliably used also for determining the sampling frequency which is needed for accurate specifying of the time arrival. The sampling frequency can be measured also by digital output (used internal divider) simultaneously during the measurement, however this method causes the source of the crosstalk between PCB and wire-bonds connecting the chip with the silicon sensor. The overall resolution (σ/μ) of time measurement by the global ToA counter is around 0.11 % for both operational modes and includes the time-walk effect, the fluctuation of the sampling frequency and the shutter time uncertainty. The channel dispersion is excluded in the same sense as for the trigger measurement above.

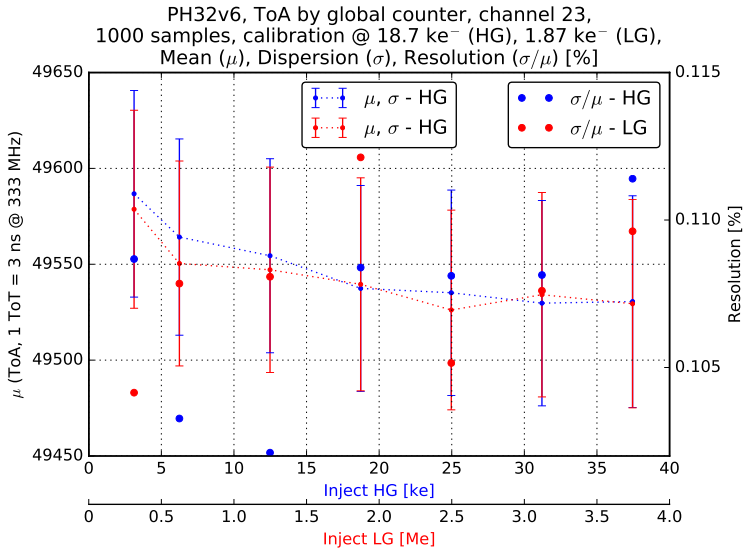

Figure 8.11: ToA response (measured by global ToA counter) to 1000 injections of charge varying from 3.1 ke$^-$ to 37.5 ke$^-$ (HG) and from 310 ke$^-$ to 3.75 Me$^-$ (LG). The chip was calibrated for a charge of 18.7 ke$^-$, i.e. 67.3 keV (HG) and 1.87 Me$^-$, i.e. 6.7 MeV (LG). Each individual mean value of ToA represents the sum of signals for global counter. The shutter time is 100 µs and delay time for inject arrive is 80 µs.

The ToT measurement provided together with the ToA measurement may be used for correction of clearly visible time-walk effect. However, the dispersion of the ToT measurement has to be taken in account. One can also observe that the ToT measurement with only one channel provides two times better resolution than the ToT measurement by all channels. It means that the channel dispersion contributes to the half of the overall ToT dispersion measured by all channels.

8.3.2 Time of flight by laser diode

The possibility of the ToF functionality is determined by the measurement with proprietary laser equipment placed to the readout chain according Fig. 8.6. The measurement setup consists of a proprietary laser device itself with characteristics described in table 8.2. The

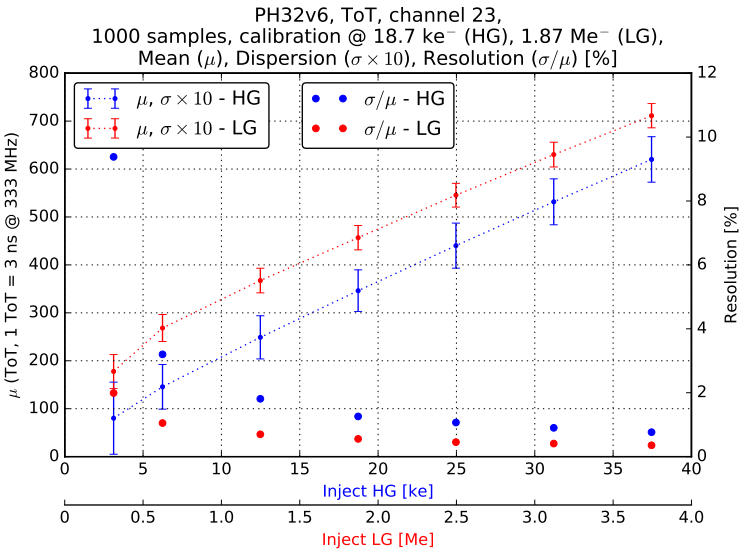

Figure 8.12: ToT response to 1000 injections of charge varying from 3.1 ke$^-$ to 37.5 ke$^-$ (HG) and from 310 ke$^-$ to 3.75 Me$^-$ (LG). The chip was calibrated for a charge of 18.7 ke$^-$, i.e. 67.3 keV (HG) and 1.87 Me$^-$, i.e. 6.7 MeV (LG). Each individual mean value of ToT represents the sum of signals for channel 23 only. The shutter time is 100 µs and delay time for inject arrive is 80 µs.

laser diode is emitting a wavelength of 1060 nm at 1 mW which is in the close infra-red. The diode is triggered by a programmable wave generator and emitted light travels through the fiber collimator directly to the silicon strip sensor. The trigger of the laser diode is derived and delayed from the shutter signal used for determining of an exposition window. The data from the PH32v6 chip is captured by SURE (Simple USB Readout Equipment) readout card. The SURE allows configuration as well as transmission of the measured data from the chip via the USB interface to the computer with pyMeaSURE software (written in python scripts). All following measurements were done with the sensor enabled by local channel configuration with sensor bias set to -150 V.

Table 8.2: Laser characteristics.

Center wavelength	1060 [nm]
Maximum power	1 [mW]
Forward current @ 1 mW	33.4 [mA]
Threshold current	16 [mA]
Transconductance [GM]	15.74 [mA/V]
Level of emission for aperture of 7 mm	26 [W/m^2]

8.3.2.1 Various exposition times

Figure 8.13 represents the ToF measurement provided by the 16-bit channel counter done in parallel with the ToF measurement provided by the 40-bit global counter presented in figure 8.14.

The measurements demonstrate the linearity of the response for various delay time between the shutter and the laser pulse. The each individual ToA mean value represents the sum of signals from the channel or the global ToA counter caused by 1000 emissions of

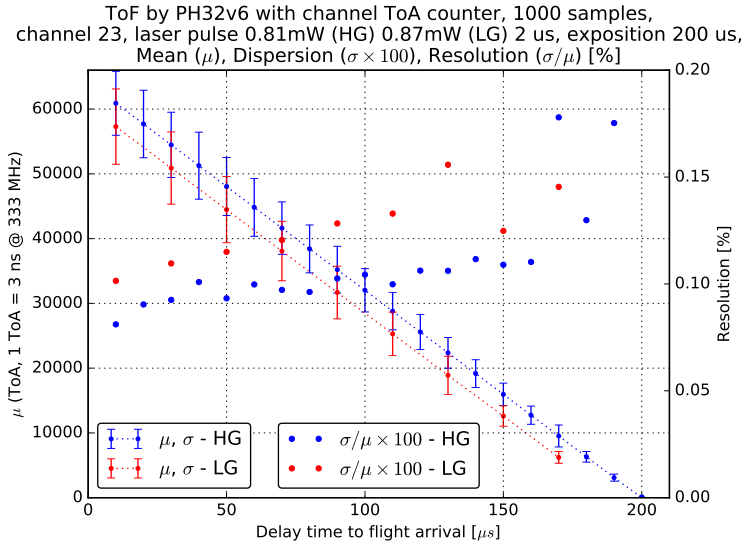

Figure 8.13: ToF measurement provided by one channel counter with various delay time between the shutter and the laser pulse. The linearity is common for both operational modes (HG and LG), together with comparable precision. ToA values response to 1000 emissions of light with laser power of 0.81 mW (HG) and 0.87 mW (LG). The chip was calibrated for a charge of 18.7 ke$^-$, i.e. 67.3 keV (HG) and 1.87 Me$^-$, i.e. 6.7 MeV (LG).

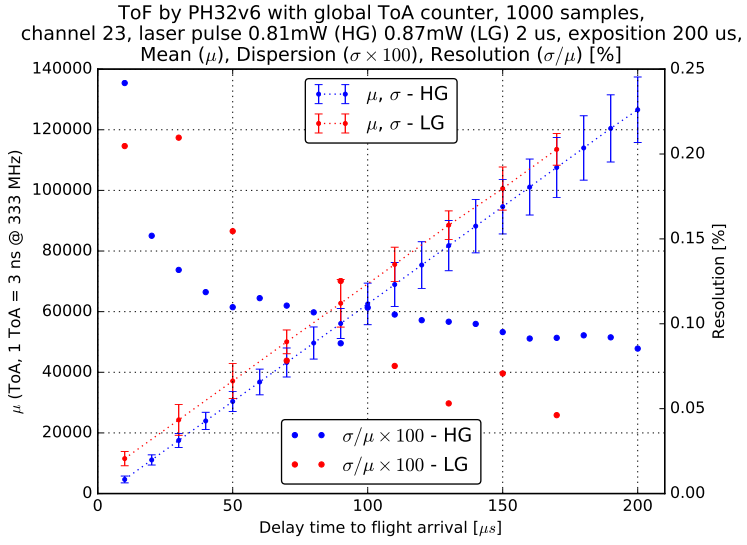

Figure 8.14: ToF measurement provided by global ToA counter with various delay time between the shutter and the laser pulse. The linearity is common for both operational modes (HG and LG), together with comparable precision. ToA values response to 1000 emissions of light with laser power of 0.81 mW (HG) and 0.87 mW (LG). The chip was calibrated for a charge of 18.7 ke$^-$, i.e. 67.3 keV (HG) and 1.87 Me$^-$, i.e. 6.7 MeV (LG).

light with laser power of 0.81 mW (HG) and 0.87 mW (LG). The linearity is common for both operation modes (HG and LG) with comparable precision. Both measurements also demonstrate the inverse ToA functionality of the channel and the global counter because the channel counter measures the time between the hit arrival and the end of the exposition and the global counter measures the time between the start of exposition and the hit arrival. One can observe that the precision is higher for the longer counting time (higher ToA value) for both counters. It is caused by averaging of the sample frequency that fluctuates in time. In this sense longer exposition time is required to obtain more precision results. It is also important to say that the precision for both possibilities of counters is comparable in this context.

8.3.2.2 Various laser power

Fig. 8.15 and Fig. 8.16 represent the ToF measurement with the static exposition time but with the various laser power varying from 0.09 mW to 0.93 mW for both operation modes.

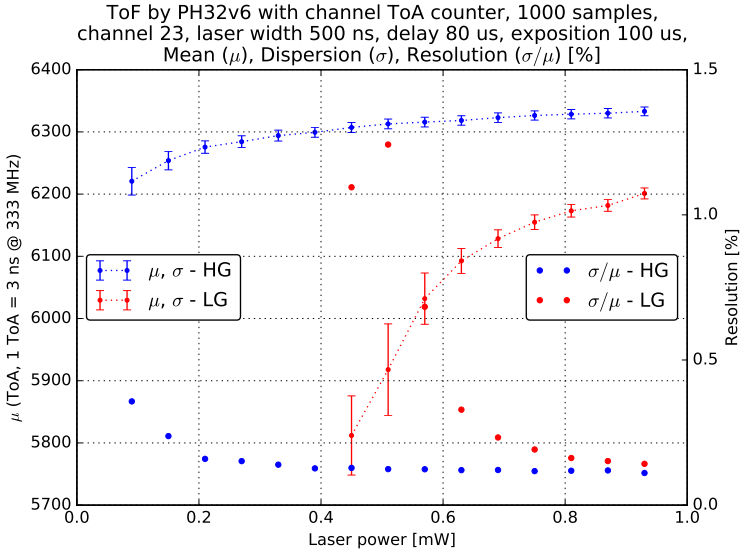

Figure 8.15: ToF measurement provided by one channel counter with various laser power varying from 0.09 mW to 0.93 mW for HG operation mode and from 0.45 mW to 0.93 mW for LG mode. The time-walk is visible for both operational modes. The HG mode provides more precise results and allows to measure lower energies. The chip was calibrated for a charge of 18.7 ke$^-$, i.e. 67.3 keV (HG) and 1.87 Me$^-$, i.e. 6.7 MeV (LG).

The measurement was done in the same conditions as previous one with the channel (Fig. 8.15) and the global ToA counter (Fig. 8.16) in parallel. The each individual ToA mean value represents the sum of signals from the channel or the global ToA counter caused by 1000 emissions of light for every laser power. The predicted time-walk effect is clearly visible for both operation modes (HG and LG) and for both possibilities of counters. There should be correlation because the signals that are triggering these counters are derived from the same source of the CSA output. One can observe that the HG mode provides more precise results in all range of the laser power and is more sensitive to the lower energies than LG mode where the energy was under the threshold of discriminator.

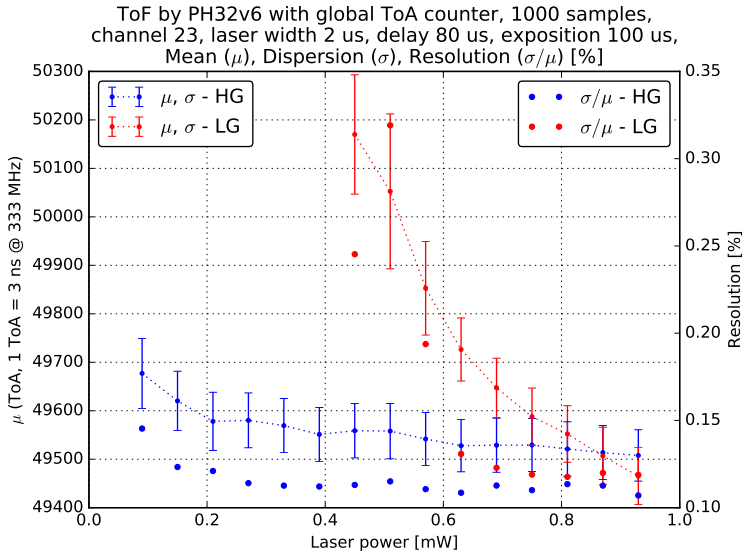

Figure 8.16: ToF measurement provided by global ToA counter with various laser power varying from 0.09 mW to 0.93 mW for HG operation mode and from 0.45 mW to 0.93 mW for LG mode. The time-walk is visible for both operational modes. The HG mode provides more precise results and allows to measure lower energies. The chip was calibrated for a charge of 18.7 ke$^-$, i.e. 67.3 keV (HG) and 1.87 Me$^-$, i.e. 6.7 MeV (LG).

8.3.2.3 Time-walk effect correction

Following example demonstrates one possibility of the time-walk effect correction which may be done by simultaneously measurement of ToF provided by the 40-bit synchronous global STSCL counter in parallel with the ToT energy measurement. The input data are shown in Fig. 8.17 for measurement with only one allowed channel. The measurement is running in LG mode with the laser power varying from 0.57 mW to 0.93 mW. One can observe that the dispersion is much higher than the dispersion measured by the injected charge from measurements in Fig. 8.12 and Fig. 8.11. There are several reasons beside slightly different range of the injected energies. Instead of the injected charge the laser diode for light emitting is used and this contributes to several sources of additional errors. Besides the synchronization uncertainty between the shutter and the laser triggering provided by a wave generator there is the most important source of the error incoming from the silicon strip sensor. The strip has relatively high capacitance which come from the requirement of the dose rate measurement what is the main purpose of the sensor use. Also due to AC coupling the strip contains the metal layer almost over all the strip area what makes the strip not fully open for light emission. This property is significant for determination of an ion penetration to a depleted layer of the sensor for the energy deposition. However, this article is focused on the PH32 chip which can be connected by wire-bonds to the different kinds of the sensor.

Fig. 8.17 represents the mean and the dispersion as sum of the 1000 samples for each laser power during the ToT and the ToF measurement at the same time. In contrast to that, Fig. 8.18 represents the mean and the dispersion of the ToF value which comes from the global ToA counter as sum of all samples belonged to each individual ToT value which comes from the channel counter (In the plot labeled as 'ToA - uncorrected'). From these data the mean value was obtained (In the plot labeled as 'ToA - total mean'). To obtain an interpolation for uncorrected ToA data the cubic spline interpolation (third order) provided

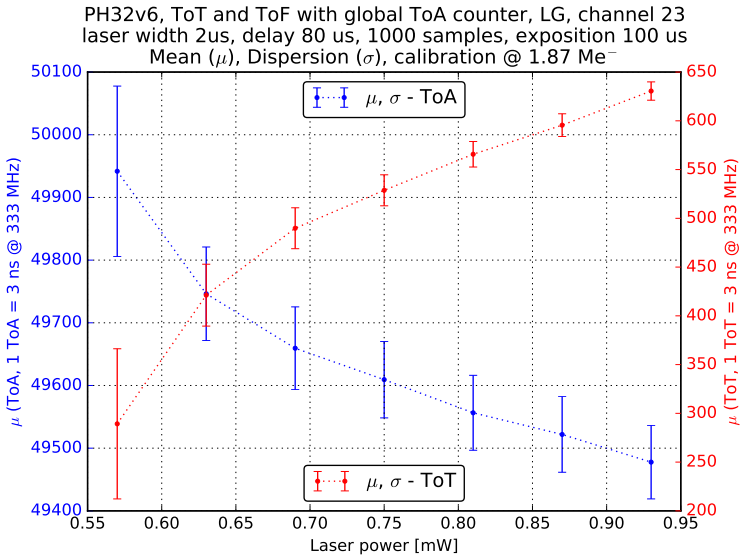

Figure 8.17: Measurement of ToT by one channel counter together with ToF by global ToA counter at the same time with various laser power in LG mode. The mean and the dispersion values represent the sum of the 1000 samples for each laser power. The chip was calibrated for a charge of 1.87 Me-, i.e. 6.7 MeV and operated in LG mode. The measurement represents the input data for time-walk correction.

by *scipy* python package was used (In the plot labeled as 'ToA - interpolation'). Since the interpolation function of the ToA values is known one can calculate corrected data for every ToA value in respect to the total mean of ToA values (In the plot labeled as 'ToA - corrected'). The dispersion is getting higher with lowering the deposited energy what is caused mainly by the sensor performance which was already mentioned. This approach demonstrates one possibility to correct the time-walk effect by measuring the energy of the particle at the same time with the ToF measurement.

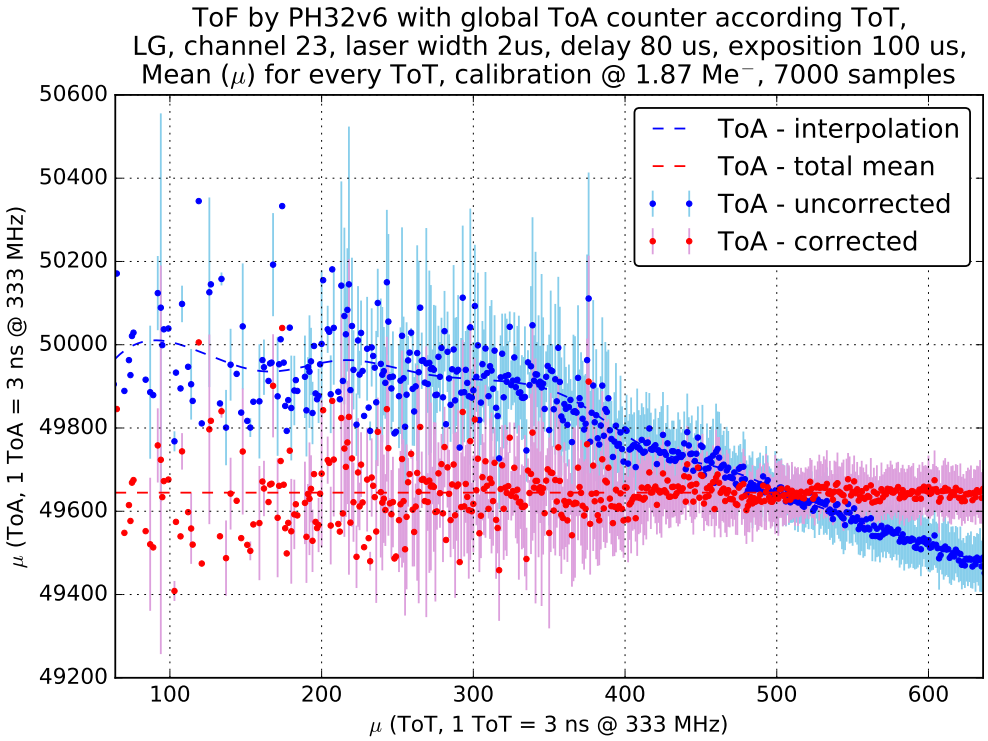

Figure 8.18: The mean and the dispersion values of ToA represent the sum of all samples (derived from Fig. 8.17) belonged to the each individual ToT value. Spline interpolation is calculated to obtain time-walk correction data and followed by the corrected mean values of ToA through all ToT energies.

Chapter 9

Ionizing radiation measurements

9.1 Measurement of energy spectra

The energy spectra measured and described in this section were provided by two versions of the chips, namely PH32v4 and PH32v6. Some of them represents the same spectrum measured during different conditions by different chips for comparison purposes. The more precise results of energy spectra are provided by newer version of the chip PH32v6 which has some improvements against its predecessor. Beside electronic disconnection of the sensor during the calibration process which was not possible by the chip version PH32v3 (the cip PH32v4 contains this feature), the chip PH32v6 provides in addition these improvements important for the measurement of the energy spectra:

- asynchronous counter - to avoid crosstalk between digital power rails and CSA
- delay shutter - to eliminate crosstalk between signal shutter and analog input
- revision of CSA parameters - linearizing the output, lower input noise

The list of improvements features is not listed completely. More about chip versions and its main differences is described in section 6.2.

Has to be mention that the precision of measurements is affected not only by readout chips but also by not-same measurement setups and conditions during measurement and by improving the calibration method as well.

One has to realize other important point that all measurements were made in the air conditions what is significant factor mainly for measuring of alpha spectra or any ions. The specific energy loss and range of heavy ions discussed in section 5.1.2 are very depending on the penetrating environment. Even few millimeters of the air caused significant energy loss. During measurements discussed in this work the radioactive sources are placed very near the sensor but not enough to avoid energy loss. For the spectra measurement the silicon strip sensor with 32 identical strips (more described in section 6.1) were used and the dimensions 8×18 mm^2 are causing really relevant point in discussion about accuracy

of results. The measuring done in the vacuum would provide results closer to the reference one but was not made till now.

Last but not least the relatively high capacitance 4 pF per channel is also important point. The sensor with smaller channel area and lower capacitance would significantly increase accuracy of the measurements of energy spectra. However, other issues would arise as charge sharing or necessity to have long exposition time.

9.1.1 The PH32 chip operated in HG mode

Fig. 9.1 shows energy spectrum of ^{241}Am measured in the HG mode mode for gamma rays by PH32v4 (9.1(a)) and PH32v6 (9.1(b)) chip. The curves represent the sum of data from all 32 channels.

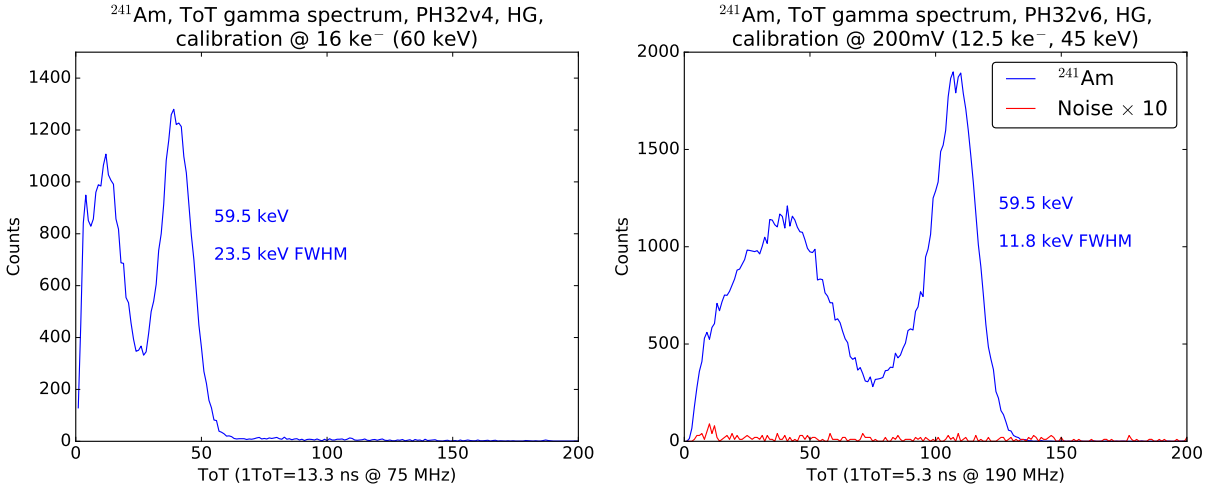

(a) PH32v4 (b) PH32v6 - 10n

Figure 9.1: The energetic spectrum of the ^{241}Am measured by the PH32 chips with the silicon sensor in the air. The chip was operated in HG mode for measurement of the energy spectrum of gamma rays. PH32v4 was calibrated for the charge of 16 ke$^-$, i.e. 60 keV (9.1(a)) and PH32v6 for the charge of 12.5 ke$^-$, i.e. 45 keV (9.1(b)). Two 100 µm slim aluminium foils were used to cover the sensor to avoid α particles produced by ^{241}Am penetrating to the surface of the sensor. The low noise plotted in 9.1(b) is for comparison purposes only.

Laboratory ^{241}Am source is positioned in front of the sensor to its central part with appropriate gap between them. Bias voltage was applied to deplete the sensor and adequate exposure time for one readout period was set. The chip is operated in first hit energy mode 6.2.2.2, therefore each channel collects deposited charge caused by the first arrived particle only during the given exposure time window. After previous data collection the next exposed frame can start. This process was repeated reasonable times to collect data for

overall exposure time. The main measurement conditions are summarized in the following table 9.1:

Measurement conditions	PH32v4	PH32v6
Bias voltage	−100 V	−150 V
Gap between source and sensor	6 mm	1 mm
Exposure time for one readout period	100 ms	100 ms
Overall exposure time	1000 s	10 min
Threshold of discriminator VDISC	550 mV	630 mV
Inject during calibration	250 mV	200 mV

Table 9.1: Measurement of energy spectra in HG mode - measurement conditions.

To collect the energy belonging only to the soft photons the sensor has to be covered by the aluminium foil to avoid the penetration of the alpha particles from the source ^{241}Am. For that purpose two 100 µm slim aluminium foils were used to cover the sensor. The energy of the soft particle is mostly collected into one sensor strip and therefore the detection module with the PH32 chip can easily calculate deposited energy directly from registered data and no additional processing is needed.

For comparison, noise measurements without a radioactive source were made with the same measurement conditions (9.1(b)). It is visible that the noise is minimum and measured spectrum of ^{241}Am was not affected by it.

For a more comprehensive view gamma spectrum of uranium ore and spectrum of X-ray tube with wolfram target is presented in Fig. 9.2. The both measurement were made by the PH32v4 chip with the silicon sensor in the air in HG mode and calibrated for the charge of 30 ke$^-$.

9.1.2 The PH32 chip operated in LG mode

The same concept of the measurement of the deposited energy as in section 9.1.1 is valid for heavy particles but in the LG mode mode only. For the HG mode mode and the collection of the high energy particles the charge from adjacent strips has to be considered.

Fig. 9.3 represents the energy spectra of ^{241}Am and ^{239}Pu for the chip operated in LG mode mode and calibrated for the charge of 1.5 Me$^-$ which is well suited for the measurements of the charge deposition by heavy α particles. The measurement was running in the same or slightly different conditions except the aluminium foils where the sensor is fully open for exposition. The main differences of measurement conditions are summarized in table 9.2. From the plot one can clearly recognize two neighboring energies from two different radiation sources. The curves represent the sum of data from all 32 channels.

All energy spectra measurements presented in this section are done with the silicon sensor with 32 identical strips. The exception is the energy spectra measurement shown in Fig. 9.4 which is mentioned due to integrity of the results. The energy spectra of ^{241}Am and ^{239}Pu is measured by the PH32v5 chip with the silicon sensor which contains 10 wide

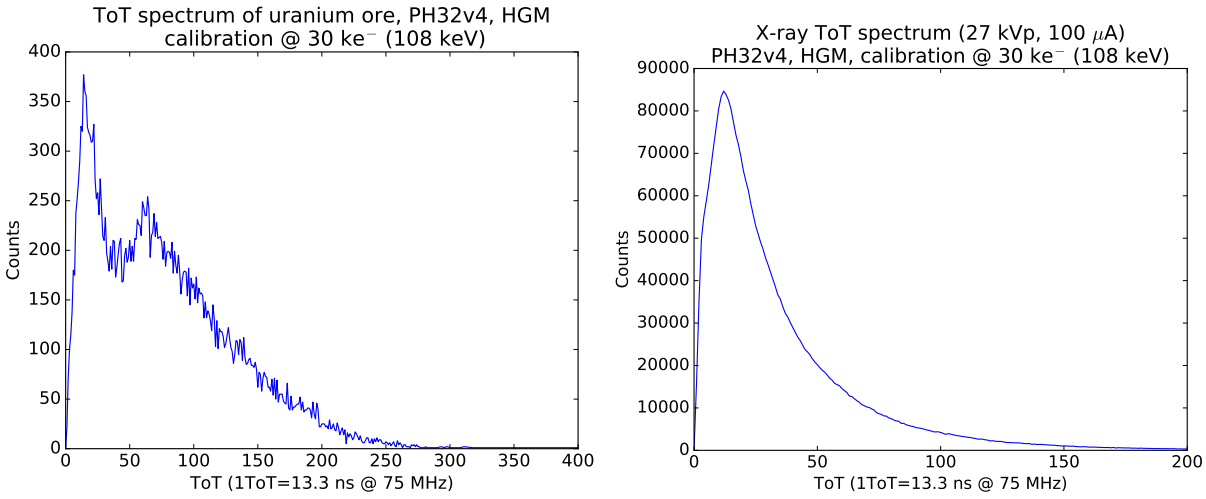

(a) Uranium ore (b) X-ray

Figure 9.2: The gamma spectrum of uranium ore (9.2(a)) and spectrum of X-ray wolfram tube (9.2(b)) measured by the PH32v4 chip with the silicon sensor in the air. The chip was operated in HG mode and calibrated for the charge of 30 ke$^-$, i.e. 108 keV.

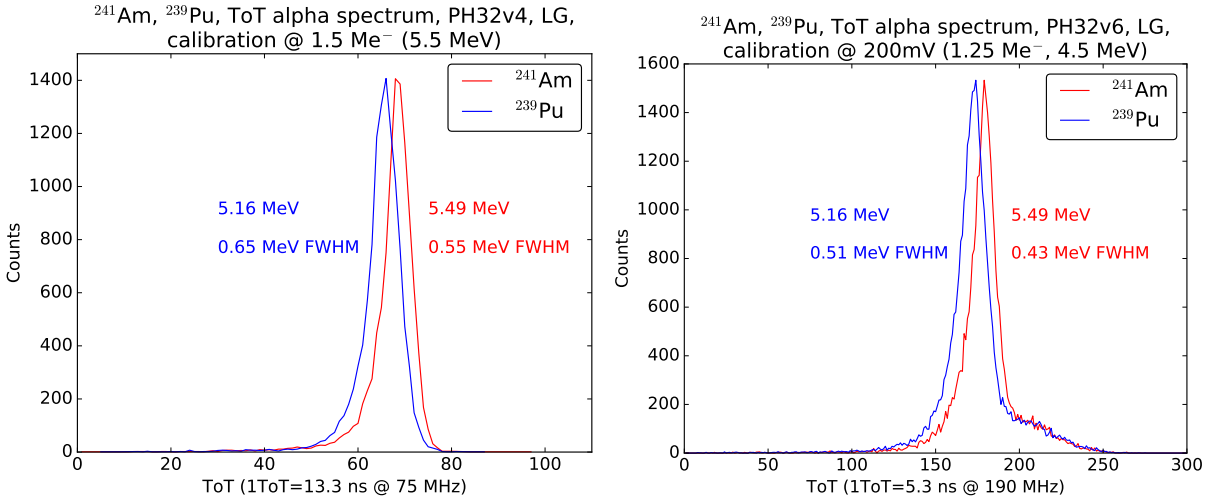

(a) PH32v4 (b) PH32v6 - 10n

Figure 9.3: The energy spectra of ^{241}Am and ^{239}Pu measured by the PH32 chips with the silicon sensor of 32 strips in the air. The chips were operated in LG mode for measurement of the energy spectrum of alpha particles. PH32v4 was calibrated for the charge of 1.5 Me$^-$, i.e. 5.5 MeV (9.3(a)) and PH32v6 for the charge of 1.25 Me$^-$, i.e. 4.5 MeV (9.3(b)). The sensor is fully open for exposition.

strips and 6 narrow strips (see section 6.1). The main purpose of this architecture of the sensor is for the dose rate measurement described in the following section. The stated

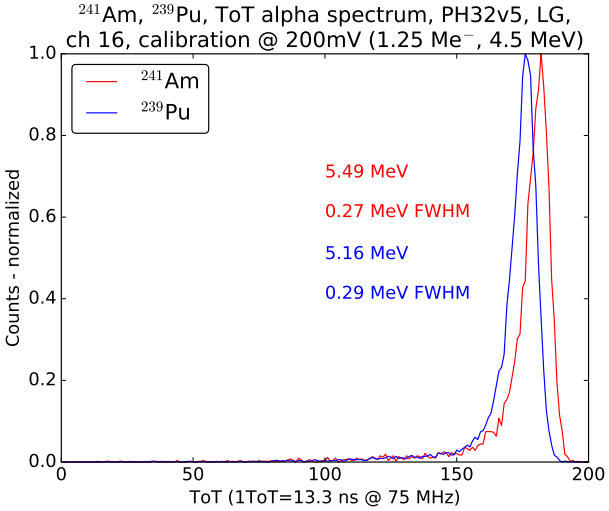

Figure 9.4: The energy spectra of ^{241}Am and ^{239}Pu measured by the PH32v5 chip with the silicon sensor with just one allowed narrow strip in the air. The chip was calibrated for the charge of 1.5 Me$^-$, i.e. 5.5 MeV. Lower FWHM in compare to measurements done by PH32v4 and PH32v6 is due to just one allowed sensor strip.

results demonstrate the ability of the energy spectra measurement by only one allowed channel. The narrow strip is used and the energy spectra precision is much higher in compare to the previous measurements provided by the chip PH32v4 or PH32v6 where the spectra were measured by all sensor strips. Saying more precisely the FWHM value is around half (exact values are shown in the appropriate figures). However, the measurement done with all allowed sensor strips provides the worst results with the FWHM values: 0.58 MeV for ^{241}Am and 0.74 MeV for ^{239}Pu. It is due to different strip geometry mainly which causes besides the different strip capacitance also more complicated equalization and post-processing methods. This disability is, on the contrary, an advantage for the dose rate measurement which allows the measurement of wide range of radiation dose due to different sensitive strip area.

Measurement conditions	PH32v4	PH32v6
Bias voltage	−100 V	−150 V
Gap between source and sensor	6 mm	1 mm
Exposure time for one readout period	100 ms	5 ms
Overall exposure time	1000 s	60 min
Threshold of discriminator VDISC	550 mV	600 mV
Inject during calibration	250 mV	200 mV

Table 9.2: Measurement of energy spectra in LG mode - measurement conditions.

Fig. 9.5 represents the measurement of energy spectra of mixed nuclides ^{241}Am, ^{239}Pu and ^{244}Cm. The measurement was made in the same conditions as for alpha sources ^{241}Am and ^{239}Pu in LG mode (Fig. 9.3).

Has to be mentioned again that non-perfect separated peaks of mixed alpha nuclides as well as individual alpha sources are caused mainly due to high capacitance of the silicon sensor (large sensitive area) and due to energy loss of alpha particle in the air (5.1.2).

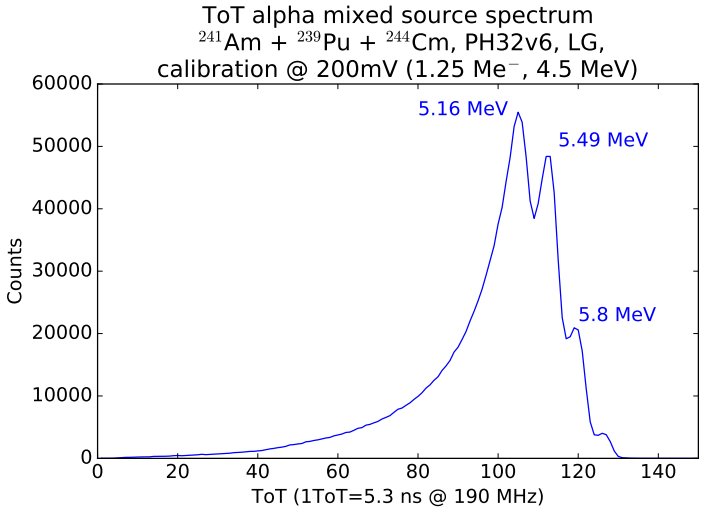

(a) Alpha mixed spectrum ^{241}Am + ^{239}Pu + ^{244}Cm

(b) Alpha mixed source

Figure 9.5: The energy spectrum of mixed nuclides ^{241}Am, ^{239}Pu and ^{244}Cm measured by the PH32 chip with the silicon sensor in the air. The PH32v6 chip was operated in LG mode for measurement of the energy spectrum of alpha particles and calibrated for the charge of 1.25 Me$^-$, i.e. 4.5 MeV. The sensor is fully open for exposition.

Also has to be know, that due to AC coupling the sensor strip contains the metal layer almost over all the strip area what makes the strip not fully open for ions penetration. This property is significant for determination of an ion penetration to a depleted layer of the sensor for the energy deposition.

9.2 Measurement of dose rate

The measurement with the radioactive source ^{137}Cs demonstrates the ability of the detection module to measure the dose rate in the broad range of 8-orders of magnitude as can be seen in the Fig. 9.6.

The radioactive isotope of cesium with the energy of γ photons of 662 keV as the certified laboratory source has been used. The radiation dose is calibrated with the respect to the distance between source and the irradiated sample. Therefore the exact radiation dose absorbed by the sensor is known. The measurement has started with very low radiation dose at 100 nGy·h^{-1} and was increasing in the range of 8 orders of magnitude to 10 Gy·h^{-1}. The exposure time for every exact value of the radiation dose was 10 seconds.

Silicon sensor connected to the PH32 chip has two different strip widths in this case. Narrow strips can measure the dose rate up to 8-times higher range compared to the wide strip design with larger area where high hit-rate saturates the front-end electronics sooner. The both curves show nonlinearity at low dose rate range $\approx$ 100 nGy·h^{-1} due to

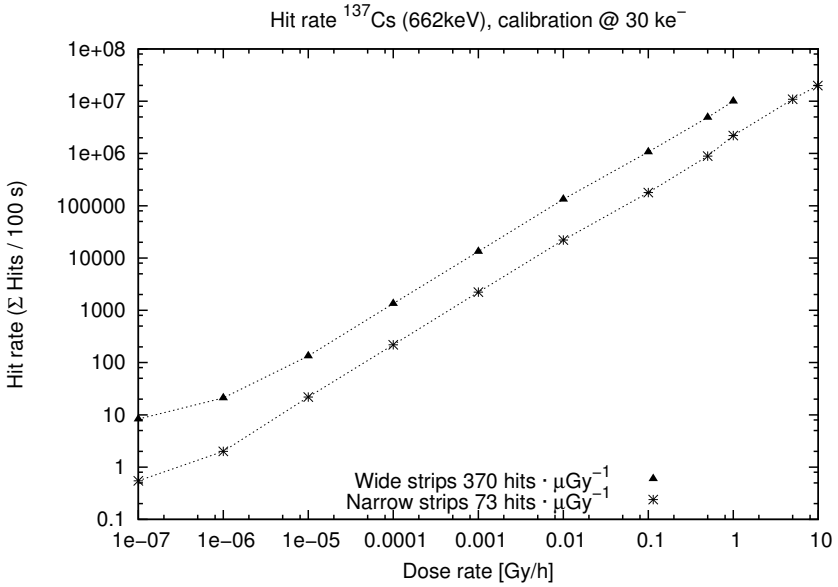

Figure 9.6: Detector response expressed as number of hits vs. dose rate. The gamma isotope ^{137}Cs was used. The energy of gamma photons is 662 keV. Two curves represent hit rates for the narrow and wide strips of the sensor. The curves show non-linearity at low dose rate range $\approx$ 100 nGy·h^{-1} due to the natural background radiation. Hit-rate is linear for dose rate in range of 8 orders of magnitude.

the natural background radiation otherwise the hit-rate is linear for the dose range of 8 orders of magnitude.

9.3 Radiation hardness

This chapter would not be complete unless the radiation hardness measurements were made. Previous measurement related to the dose rate referred to the ability to measure the total radiation dose to 10 Gy/h. The gamma isotope ^{137}Cs was used. The total dose of 20 Mrad was applied without any malfunction or any significant effect on the chip. Therefore, the chip is perfectly suitable for the dose rate measurement and the basic spectroscopy.

Another shown measurement (Fig. 9.7) refers to the power consumption. The TID study was performed using a high flux ^{60}Co source providing 1.17 and 1.33 MeV gamma-rays up to a total absorbed dose of 10 Mrad during a 12 hours period. Two PH32v2 chips were under the irradiation. One was under the ongoing tests, and the second one lay unconnected. The test series were performed repeatedly in order: the I-V characteristics of the transistors in the test structures have been measured ($\approx$20 minutes), DAC scan, digital read/write test of the shift registers ($\approx$10 minutes) and monitoring of digital and analog current of the chip during all the tests. The DAC characteristics did not show

any significant change during the irradiation; the digital part (RW shift register test, chip configuration) also worked without any obvious problems. The results of the transistor test structures measurement is referred in more detail in [A.8].

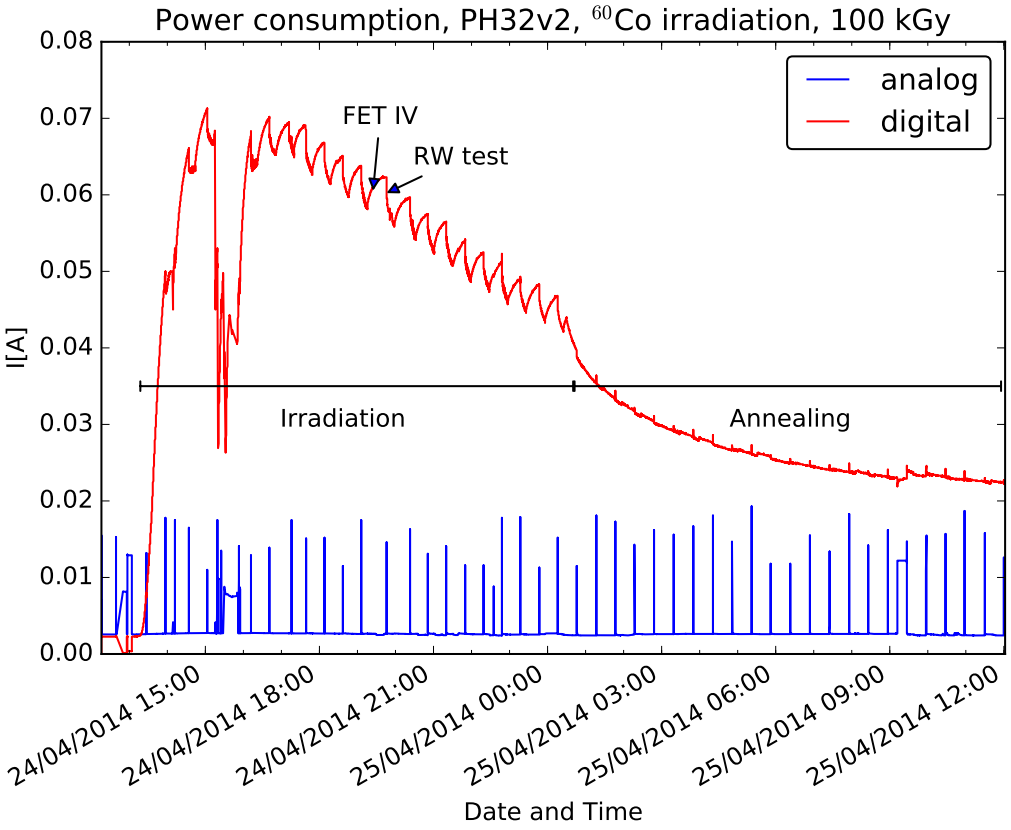

Figure 9.7: The power consumption of the PH32v2 under the ^{60}Co irradiation with total receiving the dose of 100 kGy (10 Mrad) during 12 hours.

Here presented results show that the analog current is not significantly influenced by the irradiation. On the other hand, the digital current shows a significant influence of the irradiation (about 35 times higher power consumption). However, the digital current is saturated and then gradually decreases. It is shown, that the digital activity of the large amount of transistors during the RW tests causes a decrease of TID effect compared to the transistors test where these smallest transistors are left without any flipping. After 12 hours the chip is left for annealing and the chip consumption reports decrease. The power consumption was continuously measured alongside all previous tests during next 4 days where the digital current reports 12 mA. After that period, the tests were not performed any longer. The power consumption was measured continuously further and after 26 days of annealing the digital power reports 7.5 mA (2 mA before irradiation). The inconsistency of the data during the fourth hour is caused by measurement setup issue. The TID study measured by the newer chip versions to a total absorbed dose of 100 Mrad is described in [A.18], [A.21].

Chapter 10

Final modifications and related developments

The last manufactured chip is the version PH32v7. This version has supposed to be the final iteration before ongoing engineering run. However, as I already mentioned in above chapters, the AMS foundry which is responsible for existing MPWs, terminated the possibility of engineering run for our already developed chips. This is one of dark sides of the ASIC designing as it cost besides the high financial costs and long developing process also the risk of the end of process lifetime. One could note that the risk can be avoided by choosing the proper process and foundry before any development but any more safe option would means much higher financial cost. However, we have managed the start of the engineering run of the PH32v8 chip right now under discontinued C18 process still operated by TSI Foundry, what came with necessity of redesign of our chip to the previous C18 process once again.

10.1 Engineering run

As preparation for the engineering run, the chip PH32v7 (Fig. 10.1) came with different layout dimensions for better wafer fabrication yield together with slightly tuned the analog parameters. Besides that the test structures were removed as well as some less important I/O ports.

There is one more possible improvement which could be applied to the chip - to skip the synchronization. This opinion is due to the fact that the PHpix variant (described later on), which is derived from the PH32 chip, is working without any observed metastability. The PHpix chip has no internal oscillator and therefore has no synchronization. However in this state it would be very risky to produce the chips which are not silicon proven. In the same meaning we put to the one reticle (Fig. 10.2) mainly PHpix4 chips which are totally silicon proven and tested as they were fabricated by old process.

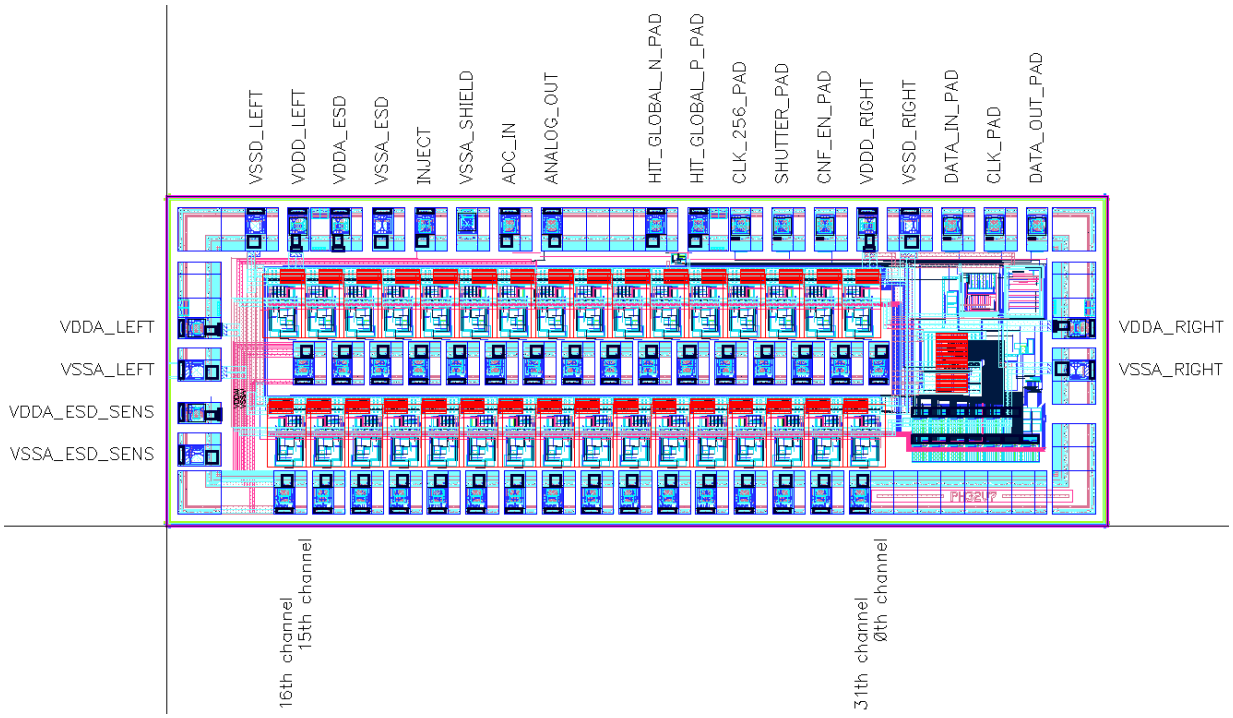

Figure 10.1: PH32v7. Chip dimensions: 1.4×4 mm^2.

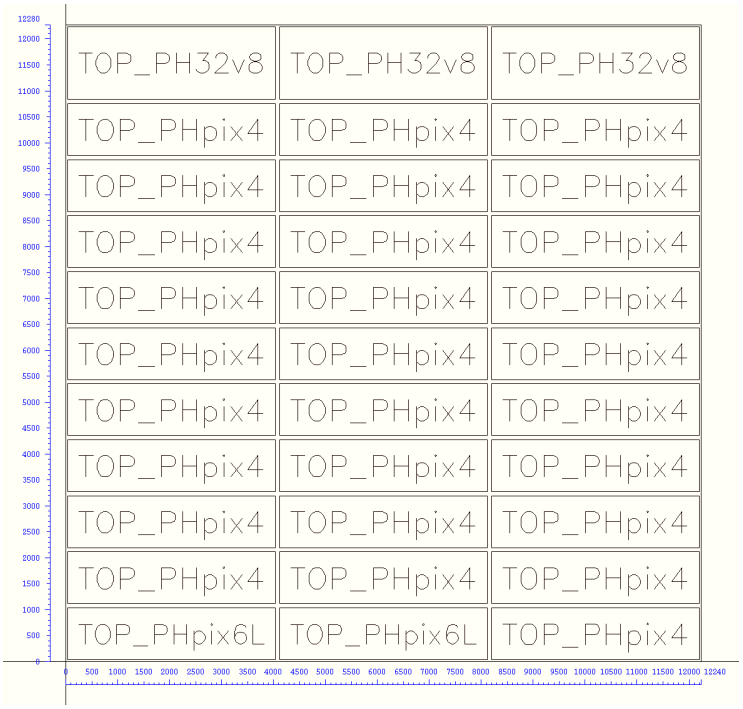

Figure 10.2: One reticle for engineering run with appropriate layout. Reticle dimensions: 12.28×12.24 mm^2.

10.2 The PHpix

The PHpix chip (Fig. 10.3) is derived from the chip PH32 and primarily is dedicated for pixelated gamma-ray camera used in radiation therapy. The chip is working only in hit–counting mode and therefore much more simple design is required in compare to the PH32 chip. This lead to remove the synchronization by internal clock and allows to design the detector module with array of PHpix chips (Fig. 10.4) to make novel pixel detector topology. The novel approach as well as chip performance is described in more details in [A.13].

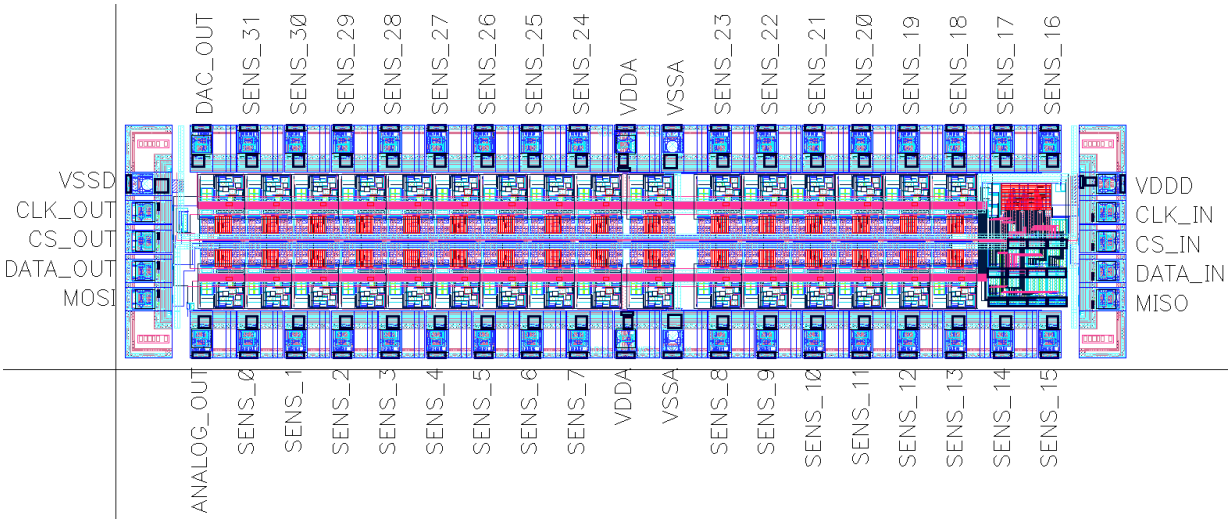

Figure 10.3: PHpix5. Chip dimensions: 1×4 mm^2.

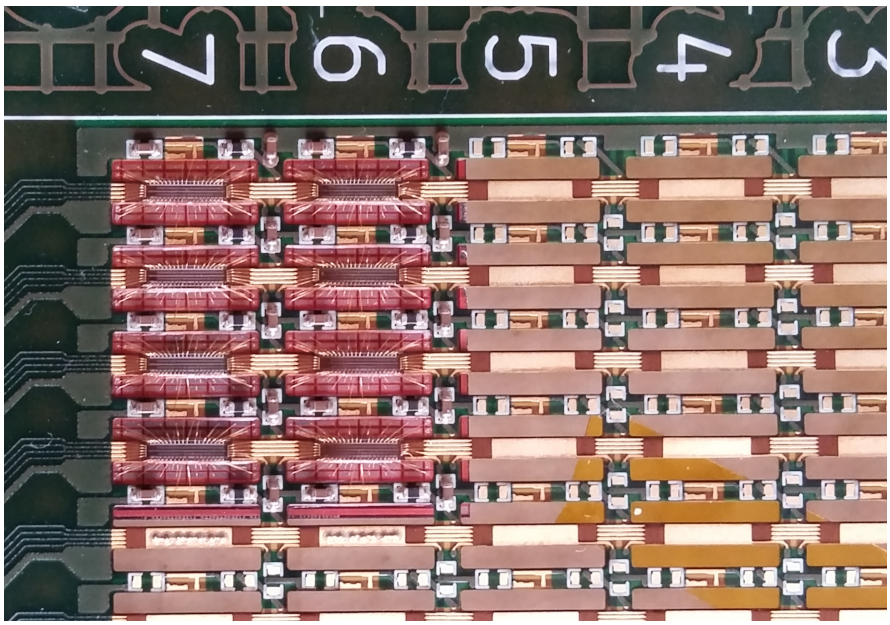

Figure 10.4: The detection module with eight mounted chips (16×16 pixels). The complete detector module contains 50×64 pixels.

The examples of images taken by X-ray tube and Cobalt-60 radiation therapy unit captured by PHpix chip are shown in Fig. 10.5.

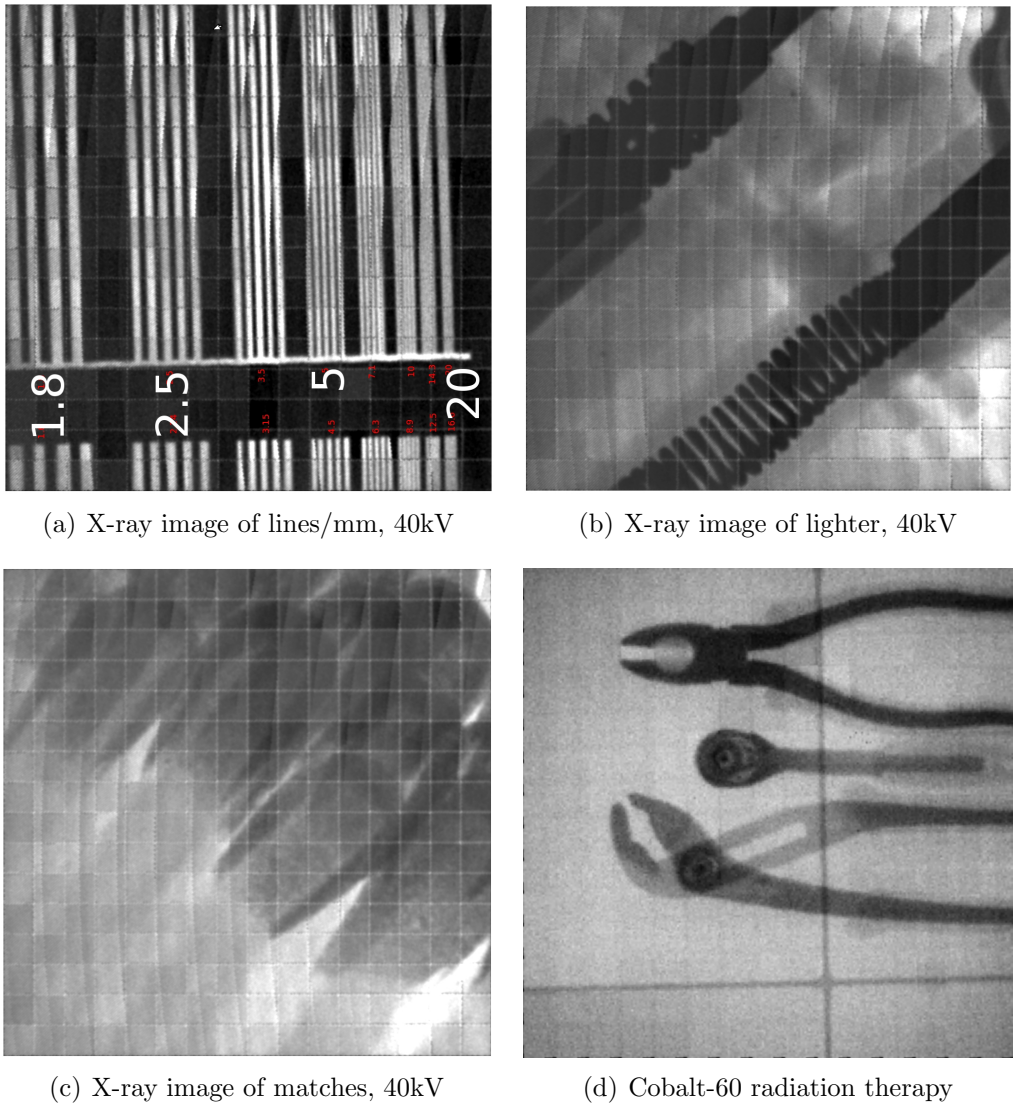

(a) X-ray image of lines/mm, 40kV

(b) X-ray image of lighter, 40kV

(c) X-ray image of matches, 40kV

(d) Cobalt-60 radiation therapy

Figure 10.5: Examples of images taken with X-ray tube and Cobalt-60 radiation therapy unit captured by PHpix chip [A.13].

10.3 The X-CHIP

The new trends in semiconductor detectors of ionization radiation lead to developing the more compact detector systems with limitation of mechanical processes. One approach is to merge the sensor to the single ASIC readout chip itself. This stance leaves the concept of hybrid pixel detectors described above.

The X-CHIP readout chip is Monolithic Active Pixel Sensor (MAPS) designed in a commercially available (without any process changes) 180 nm SOI CMOS technology. The chosen technology features a high voltage devices (sensor diodes) and large scale integration of front-end electronics. Both can be placed into one pixel area what allows to design the monolithic high resolution detector system (Fig. 10.6).

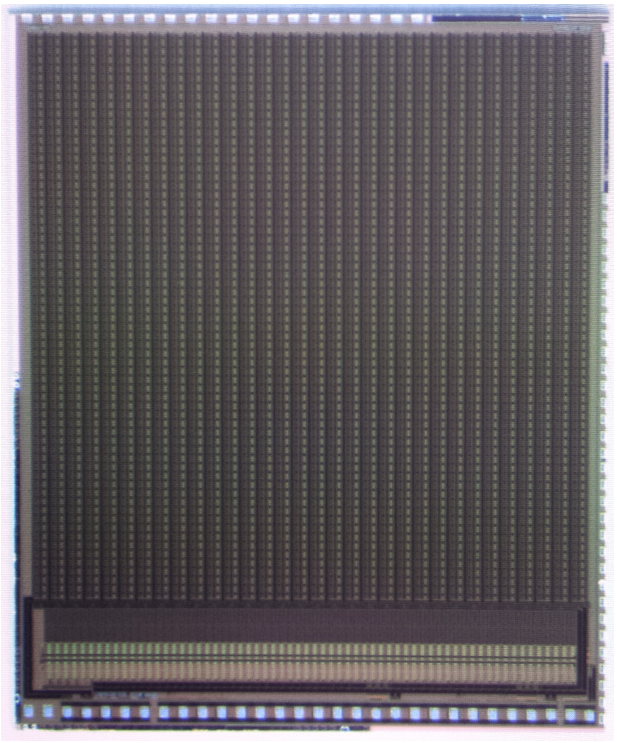

Figure 10.6: The X-CHIP-03 ASIC.

However, for the special circumstances where the low energies are required, the system may indicate low efficiency due to relatively thin depletion layer especially for low X-rays. Nevertheless, the detection concept fits well for radiation imaging (Fig. 10.7). The overall detection performance of the X-CHIP readout ASIC is described in [A.12], [A.14], [A.20].

The last family of our readout chips is called **SpacePix**. The SpacePix is derived from current X-CHIP-03 chip with a logarithmic front-end amplifier response to cover a large required dynamic range for heavy ion detection. The chip contains SEU-hardened digital circuits and is designed primarily for charged particle sensing in the space environment. The SpacePix-D, a battery-operated standalone pixel detector with a X-CHIP-03 chip is described in [A.17].

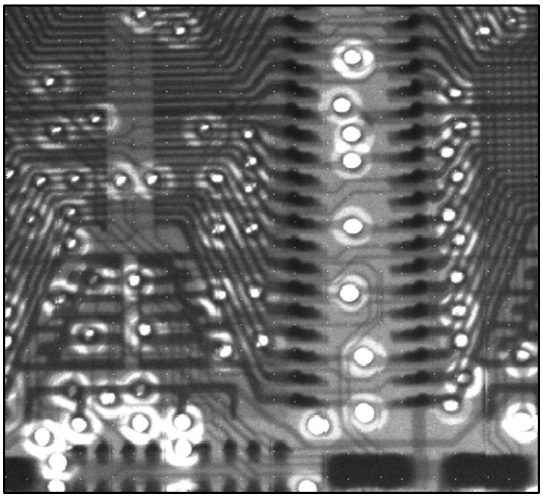

(a) X-ray image of RAM chip, 40kV

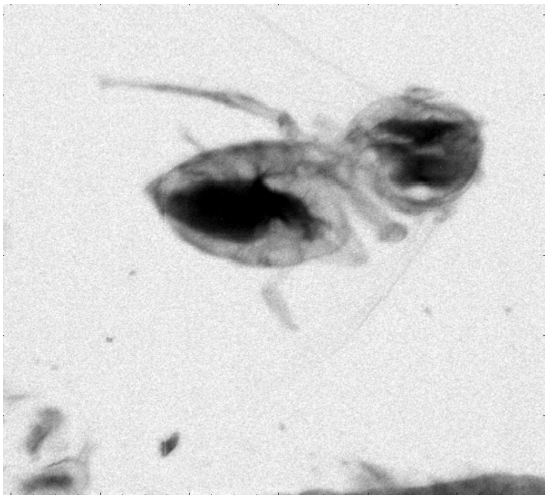

(b) X-ray image of bee, 30kV

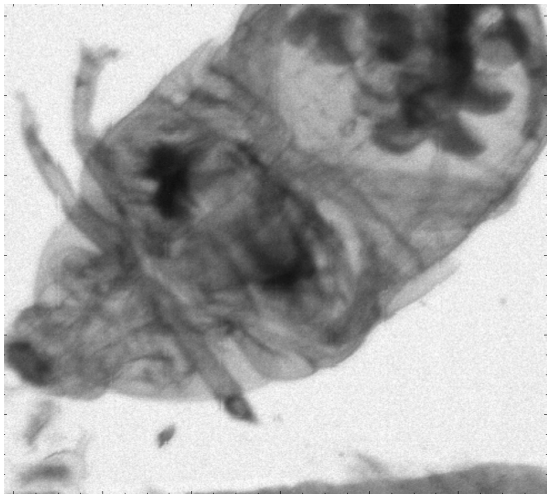

(c) X-ray image of bug, 30kV

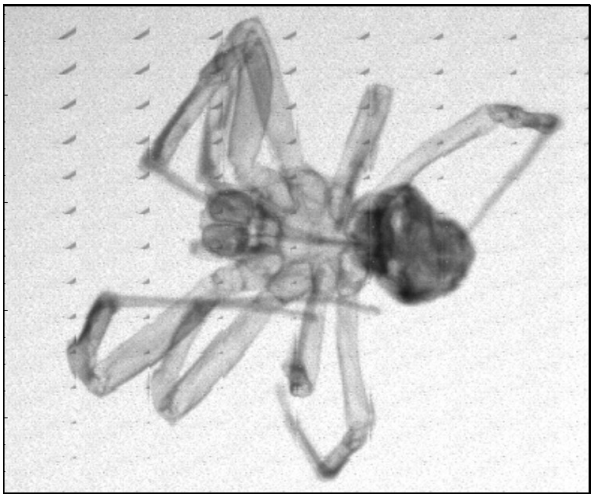

(d) X-ray image of spider, 40kV

Figure 10.7: Examples of X-ray images captured by X-CHIP-02 [A.14].

Chapter 11

Conclusion

This study was created to show the current state of our research in the field of the particle detection and to present the PH32 front-end readout electronics.

Knowledge and experience with the particle detection systems were obtained during the work at the ATLAS particle physics experiment at the Large Hadron Collider at CERN and during solving the research project Competence Centres Programme TE01020069 - Advanced Detection Systems of Ionising Radiation Project. Some radiation measurements were made in cooperation with the companies: UJP PRAHA a.s., VF a.s. and esc Aerospace.

The study is focused on the PH32 front-end readout integrated circuit with specific intention on my own contribution. The main description is orientated on the possibility to use the PH32 chip with the silicon sensor for energy measuring of soft X-rays, beta radiation and charged ions such as alpha particles as well as for the dose rate measurements and the time of arrival of the first hit. Measurements in this study have proved the ability to measure the charge from the silicon sensor in the wide range in two separate operational modes as well as the dose rate measurement in the range of 8–orders of magnitude. Along this, the PH32 chip can be used in the particle tracking or ion mass spectroscopy, which was also proven. Overall, the chip has a relatively high radiation hardness, which was proven to dose rate of 100 Mrad. Among others, the PH32 was successfully tested in the Tokamak COMPASS to monitor the run-away electrons directly inside the tokamak vacuum chamber [A.15], [A.16]. This particular application shows that the PH32 detection capabilities are exceeding those of other contemporary detectors.

Furthermore, the study widely describes the calibration processes using the injected charge from an external source. The proper calibration process is necessary to obtain the relevant data with respect to the channel uniformity, noise, linearity, gain, dispersion between individual channels or appropriate resolution information.

The last but not least, the study describes the major issues that had to be fixed during the development of the PH32 readout chips. This has led to many new approaches to the detection of radiation particles which were described above primarily. Along these issues, during the last years of development, we have had to react dynamically to changes in the production processes or to the problems of the foundry production itself. This

resulted to many iterations of development associated with multiple chip submissions. The PH32v6 chip is the last well tested version. The last version of the produced chip (PH32v7) was supposed to be the last development version before the engineering run. However, the problems coming out from the end of the production process caused the necessity of redesigning the chip into an older technology. Despite all the challenges, the PH32v8 chip is in the fabrication process in ongoing engineering run.

The contribution of the present and the future research supposed to be mainly in determining the radiation hardness ability, improvement of the calibration process and in general, finding the solutions for better energy and time resolution. The first listed includes the measurements aimed on a single event upset inside the configuration registers, changing DAC outputs, threshold levels, feedback currents, voltage gain and in generally all circumstances causing the changes of detection performance. The second listed includes the equalization improvement by using the radiation source with known injected energy or X-ray tube to gain homogeneous radiation over the sensor. The last mentioned option includes among other things the decrease of the noise originate from the sensor by decreasing the sensor strip size or in general to use other type of the sensors (CdTe).

At the end of this study there is a short description of the PHpix chip development, derived from PH32, which is primarily dedicated for pixelated gamma-ray camera used in radiation therapy. This chip arrangement represents the novel pixel detector topology. The last look is dedicated to the new trends in semiconductor detectors of ionization radiation lead to the development of more compact detector systems with limitation of mechanical processes. The result is in the form of a new monolithic chip called the X-chip, which fits well for radiation imaging. The most recently designed and manufactured chip on which I have worked as a digital designer at the time of writing this study is called SpacePix. The chip is designed primarily for charged particle sensing in the space environment and therefore the chip electronics is supposed to be radiation tolerant. In this time, the SpacePix is collecting the data in orbit in the Socrat-R satellite prepared by the Lomonosov Moscow State University [26]. The chip is placed in a module prepared jointly by the Faculty of Nuclear Sciences and Physical Engineering CTU in Prague, the company esc Aerospace and the Nuclear Physics Institute of the CAS.

11.1 Current research

At the present time, many efforts are underway to implement chips in various daughter projects. Potential use of PH32 chips is in many sectors, mainly including: nuclear power plants, waste management, nuclear medicine, industry and manufacturing, research of atmospheric phenomena or space flight missions. From many projects currently underway, below is a list of the most interesting research activities:

Dose rate monitoring – High dose range meter [27] and Smart directional rate meter [28]. The detector itself includes four detection modules (Fig. 11.1).

Air radiation monitoring – Aerosol Sampler [29].

Person and items contamination monitoring – Hand-foot contamination monitor [30].

All these ionizing radiation monitoring systems are developed in cooperation with VF a.s. A miniature detection module has been developed for this purpose (Fig. 11.1). It contains a silicon sensor with 32 channels and encapsulated PH32 chip with the dimensions only 27×10 mm^2. The miniature module allows smart packaging to the multi detectors system.

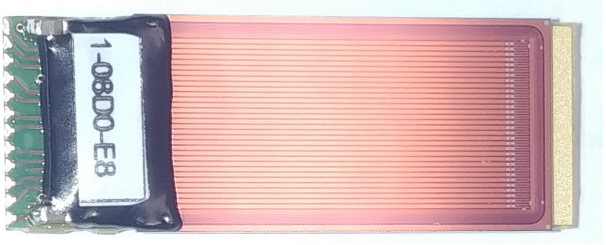

Figure 11.1: Detection module contains silicon sensor with 32 channels and encapsulated PH32 chip. Module dimensions: 27×10 mm^2.

Atmospheric monitoring – The CRREAT project [31]. The detector with PH32 chips which was used as a monitoring system and it was released into the stratosphere by high altitude stratospheric balloon.

This project is carried out in cooperation with the Nuclear Physics Institute of the CAS and the esc Aerospace. The program is involved in the research of atmospheric phenomena. Besides this concept it is also in the process of preparation to use the detector on the base of the PH32 chip for flying by a drone.

Spaceflight mission – Bion-M2 bio-satellite project. The Bion-M2 is focused on the effects that the space radiation may have on a living organism. The animals on board (65 mices) are expected to receive a dose of space radiation comparable to a three-year-long flight aboard the International Space Station. The cosmic ray detector itself includes eight PH32 chips and rocket launch is scheduled for 2022.

This project is carried out in cooperation with the Russian space agency Roscosmos [32] and the FNSPE CTU in Prague which supplies PH32 chips in Bion-M2 project.

Cosmic energy particles monitoring from solar flares – negotiations with the Institute of Experimental Physics SAS are ongoing about the possibility of using the PH32 chips for the monitoring of cosmic rays that come from the Sun. The detector should be placed at the Lomnicky Stit Observatory eventually at Basic Environmental Observatory Moussala [33]. The detector itself includes four detection modules posed one over the other at different angles for measuring dE/dx and the direction of the incoming particle.

Above listed projects are only selection from the ongoing projects. The potential for the use of PH32 chips is wide in many fields of nuclear physics. In order to meet the demand for the chips, the engineering production was managed and dozen wafers were already produced (Fig. 11.2). The engineering run contains approximately 70 000 chips of the PH series. Recent tests with a large area detector based on the PHpix chips show very good yield, which is above 95%. This also ensures the relatively low cost of the produced chips and therefore lowering the overall detector price.

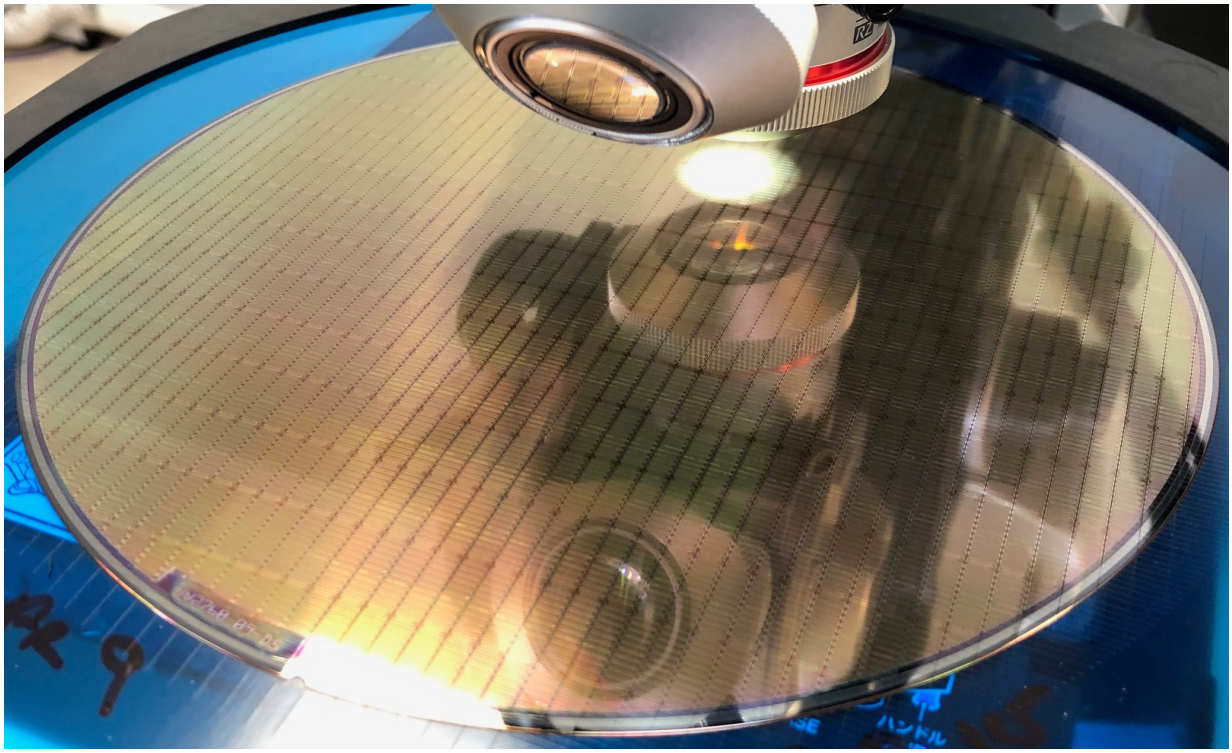

Figure 11.2: A dozen wafers contain approximately 70 000 chips of the PH series.

Bibliography

The list contains only publications devoted to the discussed topic. However, the most relevant publication devoted to my contributions is the article dedicated to the time of flight measurements with the PH32 chip [A.19].

[1] The medipix collaboration. Accessed 21 January 2019, `http://medipix.web.cern.ch`.

[2] Rd50 – radiation hard semiconductor devices for very high luminosity colliders. Accessed 21 January 2019, `https://rd50.web.cern.ch/rd50/`.

[3] G. Aad, M. Ackers, F.A. Alberti, M. Aleppo, G. Alimonti, J. Alonso, E.C. Anderssen, A. Andreani, A. Andreazza, J.F. Arguin, et al. ATLAS pixel detector electronics and sensors. *Journal of Instrumentation*, 3(07):P07007, 2008.

[4] I. Perić, L. Blanquart, G. Comes, P. Denes, K. Einsweiler, P. Fischer, E. Mandelli, and G. Meddeler. The FEI3 readout chip for the ATLAS pixel detector. *Nuclear Instruments and Methods in Physics Research Section A: Accelerators, Spectrometers, Detectors and Associated Equipment*, 565(1):178–187, 2006.

[5] R. Ballabriga, J. Alozy, M. Campbell, E. Frojdh, E.H.M. Heijne, T. Koenig, X. Llopart, J. Marchal, D. Pennicard, T. Poikela, et al. Review of hybrid pixel detector readout ASICs for spectroscopic X-ray imaging. *Journal of Instrumentation*, 11(01):P01007, 2016.

[6] M. Campbell, J. Alozy, R. Ballabriga, E. Frojdh, E. Heijne, X. Llopart, T. Poikela, L. Tlustos, P. Valerio, and W. Wong. Towards a new generation of pixel detector readout chips. *Journal of Instrumentation*, 11(01):C01007, 2016.

[7] X. Llopart, M. Campbell, R. Dinapoli, D. San Segundo, and E. Pernigotti. Medipix2: a 64-k pixel readout chip with 55-μm square elements working in single photon counting mode. *IEEE transactions on nuclear science*, 49(5):2279–2283, 2002.

[8] X. Llopart, R. Ballabriga, M. Campbell, L. Tlustos, and W. Wong. Timepix, a 65k programmable pixel readout chip for arrival time, energy and/or photon counting measurements. *Nuclear Instruments and Methods in Physics Research Section A: Accelerators, Spectrometers, Detectors and Associated Equipment*, 581(1):485–494, 2007.

[9] T. Mukoyama. Range of electrons and positrons. *Nuclear Instruments and Methods*, 134(1):125–127, 1976.

[10] D.J. Skyrme. The passage of charged particles through silicon. *Nuclear Instruments and Methods*, 57:61–73, 1967.

[11] Neutron and X-ray Detectors - Report of the Basic Energy Sciences Workshop on Neutron and X-ray Detectors. Technical report, U.S. Department of Energy, Office of Science, Office of Basic Energy Sciences, 08 2012.

[12] C.S. Wang Chang and D.L. Falkoff. On the continuous gamma-radiation accompanying the beta-decay of nuclei. *Physical Review*, 76(3):365, 1949.

[13] G.J. Neary. The β-ray spectrum of radium e. *Proceedings of the Royal Society of London. Series A, Mathematical and Physical Sciences*, pages 71–87, 1940.

[14] H. Daniel. Das β-spektrum des rae. *Nuclear Physics*, 31:293–307, 1962.

[15] M.M. Bé, V. Chisté, C. Dulieu, E. Browne, C. Baglin, V. Chechev, N. Kuzmenco, R. Helmer, F. Kondev, D. MacMahon, et al. Table of radionuclides (vol. 3–a= 3 to 244). *Monographie BIPM*, 5, 2006.

[16] L. Pages, E. Bertel, H. Joffre, and L. Sklavenitis. Energy loss, range, and bremsstrahlung yield for 10-kev to 100-mev electrons in various elements and chemical compounds. *Atomic Data and Nuclear Data Tables*, 4:1–27, 1972.

[17] T. Tabata, R. Ito, and S. Okabe. An empirical equation for the backscattering coefficient of electrons. *Nuclear instruments and methods*, 94(3):509–513, 1971.

[18] J. Kemmer, P. Burger, R. Henck, and E. Heijne. Performance and applications of passivated ion-implanted silicon detectors. *Nuclear Science, IEEE Transactions on*, 29(1):733–737, 1982.

[19] C.F. Williamson, J.P. Boujot, and J. Picard. Report cea-r3042. *Saclay, France*, 1966.

[20] R. Jenkins. *Quantitative X-ray spectrometry*. CRC Press, 1995.

[21] E.P Bertin. *Principles and practice of X-ray spectrometric analysis*. Springer Science & Business Media, 2012.

[22] J.H. Hubbell and S.M. Seltzer. Tables of x-ray mass attenuation coefficients and mass energy-absorption coefficients 1 kev to 20 mev for elements z= 1 to 92 and 48 additional substances of dosimetric interest. Technical report, National Inst. of Standards and Technology-PL, Gaithersburg, MD (United States). Ionizing Radiation Div., 1995.

[23] Neutron radiography facility (Neutra) at Paul Scherrer Institute (PSI). Accessed 22 February 2019, `https://www.psi.ch/sinq/neutra/neutra`.

[24] J. Jakubek, S. Pospisil, and J. Uher. Neutron detector based on timepix pixel device with micrometer spatial resolution. In *Hard X-Ray, Gamma-Ray, and Neutron Detector Physics XI*, volume 7449, page 744910. International Society for Optics and Photonics, 2009.

[25] M. Fisher-Levine and A. Nomerotski. TimepixCam: a fast optical imager with time-stamping. *Journal of Instrumentation*, 11(03):C03016, 2016.

[26] The Socrat-R satellite. Accessed 14 November 2019, `https://www.avcr.cz/cs/veda-a-vyzkum/matematika-fyzika-a-informatika/Dozimetr-z-UJF-bude-zkoumat-kosmicke-pocasi/`.

[27] High dose range meter. Accessed 14 November 2019, `https://www.vfnuclear.com/en/products/high-dose-range-meter`.

[28] Smart directional rate meter. Accessed 14 November 2019, `https://www.vfnuclear.com/en/products/directional-dose-rate-meters-mdg-12s-13s`.

[29] Aerosol sampler. Accessed 14 November 2019, `https://www.vfnuclear.com/en/products/aerosol-sampler-boa-80`.

[30] Hand-foot contamination monitor. Accessed 14 November 2019, `https://www.vfnuclear.com/en/products/hand-foot-contamination-monitor-hf-series`.

[31] The CRREAT project. Accessed 14 November 2019, `http://www.ujf.cas.cz/en/research-development/large-research-infrastructures-and-centres/crreat/objectives/`.

[32] Roscosmos. Accessed 14 November 2019, `https://www.roscosmos.ru`.

[33] F Spurny, M Gelev, K Turek, I Dimov, and E Hristova. Environmental external radiation at some bulgarian localities. In *International Symposium INSINUME. In situ nuclear metrology as a tool of radioecology. Radioprotection of the environment*, pages 1–8, 2004.

Publications of the author on the discussed topic

The list contains only publications devoted to the discussed topic. However, the most relevant publication devoted to my contributions is the article dedicated to the time of flight measurements with the PH32 chip [A.19].

The publications are sorted according to the importance and method of publication.

Impacted journals:

[A.19] Z. Janoska, T. Benka, M. Havranek, M. Hejtmanek, J. Jakovenko, V. Kafka, M. Kaschner, M. Marcisovska, M. Marcisovsky, G. Neue, P. Svihra, L. Tomasek, P. Vancura, V. Vrba. *Time of flight measurement by the PH32 chip.* Journal of Instrumentation, April 2019, Volume 14, co-authorship: 80%.

[A.8] M. Carna, M. Havranek, M. Hejtmanek, Z. Janoska, M. Marcisovsky, G. Neue, L. Tomasek and V. Vrba. *Radiation hardness evaluation of the commercial 150 nm CMOS process using ^{60}Co source.* Journal of Instrumentation, June 2014, Volume 9, co-authorship: 12.5%.

[A.11] A. Nomerotski, I. Chakaberia, M. Fisher-Levine, Z. Janoska, P. Takacs, T. Tsang. *Characterization of TimepixCam, a fast imager for the time-stamping of optical photons.* Journal of Instrumentation, January 2017, Volume 12, co-authorship: 10%.

[A.18] M. Marcisovska, T. Benka, M. Havranek, M. Hejtmanek, Z. Janoska, V. Kafka, M. Marcisovsky, G. Neue, J. Populе, P. Svihra, L. Tomasek, P. Vancura, V. Vrba. *A Comparative Study of the TID Radiation Effects on ASICs Manufactured in 180 nm Commercial Technologies.* Journal of Instrumentation, December 2018, Volume 13, co-authorship: 7.69%.

[A.17] T. Benka, M. Havranek, Z. Janoska, V. Kafka, M. Marcisovska, M. Marcisovsky, G. Neue, P. Suchanek, P. Svihra, R. Sysala, L. Tomasek, P. Vancura, V. Vrba. *The SpacePix-D Radiaton Monitor Technology demonstrator.* Journal of Instrumentation, December 2018, Volume 13, co-authorship: 7.14%.

[A.14] M. Havranek, T. Benka, M. Hejtmanek, Z. Janoska, V. Kafka, J. Kopecek, M. Kuklova, M. Marcisovska, M. Marcisovsky, G. Neue, P. vihra, L. Tomasek,

P. Vancura, V. Vrba. *MAPS sensor for radiation imaging designed in 180 nm SOI CMOS technology.* Journal of Instrumentation, June 2018, Volume 13, co-authorship: 7.14%.

[A.12] T. Benka, M. Havranek, M. Hejtmanek, Z. Janoska, J. Jakovenko, M. Marcisovska, M. Marcisovsky, G. Neue, L. Tomasek, V. Vrba. *Characterization of pixel sensor designed in 180 nm SOI CMOS technology.* Journal of Instrumentation, January 2018, Volume 13, co-authorship: 10%.

[A.13] G. Neue, T. Benka, M. Havranek, M. Hejtmanek, Z. Janoska, V. Kafka, O. Koncek, O. Korchak, D. Lednicky, M. Marcisovska, M. Marcisovsky, J. Popule, M. Semmler, J. marhak, P. vihra, L. Tomasek, V. Vrba. *PantherPix hybrid pixel γ-ray detector for radio-therapeutic applications.* Journal of Instrumentation, February 2018, Volume 13, co-authorship: 5.88%.

[A.15] P. Svihra, D. Bren, A. Casolari, J. Cerovsky, P. Dhyani, M. Farnik, O. Ficker, M. Havranek, M. Hejtmanek, Z. Janoska, et al. *Runaway electrons diagnostics using segmented semiconductor detectors.* Fusion Engineering and Design, Elsevier, September 2019, co-authorship: 3.85%.

[A.4] J. Weingarten, S. Altenheiner, M. Beimforde, Z. Janoka, et al. *Planar pixel sensors for the ATLAS upgrade: beam tests results.* Journal of Instrumentation, October 2012, Volume 7, co-authorship: 3.23%.

[A.2] L. Gaioni, M. Barbero, D. Fougeron, S. Godiot, M. Menouni, P. Pangaud, A. Rozanov, P. Breugnon, M.Bomben, G. Calderini, Z. Janoska, et al. *Test results and prospects for RD53A, a large scale 65 nm CMOS chip for pixel readout at the HL-LHC.* Nuclear Instruments and Methods in Physics Research Section A: Accelerators, Spectrometers, Detectors and Associated Equipment, August 2019, Volume 936, co-authorship: 0.85%.

[A.1] N. Demaria, M. Barbero, D. Fougeron, F. Gensolen, M. Havranek, Z. Janoska, M. Marcisovsky, G. Neue, et al. *Recent progress of RD53 Collaboration towards next generation Pixel Read-Out Chip for HL-LHC.* Journal of Instrumentation, December 2016, Volume 11, co-authorship: 0.81%.

[A.5] J. Albert, M. Alex, G. Alimonti, Z. Janoska, et al. *Prototype ATLAS IBL modules using the FE-I4A front-end readout chip.* Journal of Instrumentation, November 2012, Volume 7, co-authorship: 0.34%.

[A.6] B. Abbott, J. Albert, F. Alberti, M. Hejtmanek, Z. Janoska, O. Korchak, et al. *Production and integration of the ATLAS Insertable B-Layer.* Journal of Instrumentation, May 2018, Volume 13, co-authorship: 0.27%.

Peer-reviewed journals:

[A.9] Z. Janoska, M. Carna, M. Havranek, M. Hejtmanek, V. Kafka, M. Marcisovsky, G. Neue, L. Tomasek and V. Vrba. *The PH32 readout integrated circuit.* Proceedings

of the 10th International Conference on Measurement, Institute of Measurement Science, Slovak Academy of Sciences, May 2015, pp. 207–211, co-authorship: 80%.

Proceedings:

[A.10] Z. Janoska, M. Carna, M. Havranek, M. Hejtmanek, V. Kafka, M. Marcisovsky, G. Neue, L. Tomasek and V. Vrba. *Measurement of ionizing particles by the PH32 chip.* Nuclear Science Symposium and Medical Imaging Conference (NSS/MIC), 2015 IEEE, IEEE, 2015, co-authorship: 80%.

[A.21] M. Marcisovska, M. Havranek, T. Benka, M. Hejtmanek, Z. Janoska, D. Lednicky, V. Kafka, M. Kuklova, M. Marcisovsky, G. Neue, P. Svihra, L. Tomasek, P. Vancura, V. Vrba. *A comparative study of single event effects induced by heavy charged particles in 180 nm technologies.* Nuclear Science Symposium and Medical Imaging Conference (NSS/MIC), 2018 IEEE, IEEE, 2018, co-authorship: 7.14%.

[A.20] M. Havranek, T. Benka, M. Hejtmanek, Z. Janoska, D. Lednicky, V. Kafka, M. Marcisovska, M. Marcisovsky, G. Neue, P. Svihra, L. Tomasek, P. Vancura, V. Vrba. *X-CHIP-03: SOI MAPS radiation sensor with hit-counting and ADC mode.* Nuclear Science Symposium and Medical Imaging Conference (NSS/MIC), 2018 IEEE, IEEE, 2018, co-authorship: 7.69%.

[A.16] M. Tunkl, D. Bren, J. Cerovsky, P. Dhyani, M. Farnik, O. Ficker, M. Havranek, M. Hejtmanek, Z. Janoska, V. Kafka, S. Kulkov, M. Marcisovska, M. Marcisovsky, J. Mlynar, G. Neue, L. Novotny, P. Svihra, V. Svoboda, L. Tomasek, V. Vrba. *The direct detection of runaway electrons using the semiconductor strip detector.* Proceedings of the 46th EPS Conference on Plasma Physics, EPS 2019, July 2019, P4.1010, co-authorship: 5%.

[A.3] E. Monteil, M. Barbero, D. Fougeron, S. Godiot, M. Havranek, Z. Janoska, M. Marcisovsky, G. Neue, et al. *RD53A: a large scale prototype for HL-LHC silicon pixel detector phase 2 upgrades.* Proceedings of Science, Volume 343, 2018, co-authorship: 0.92%.

[A.7] P. Valerio, M. Barbero, D. Fougeron, F. Gensolen, M. Havranek, Z. Janoska, M. Marcisovsky, G. Neue, et al. *65 nm Technology for HEP: Status and Perspective.* Proceedings of Science, September 2014, co-authorship: 0.81%.

Appendix A

Specification and configuration registers of PH32v6

A.1 Specification of the PH32v6 integrated circuit

Technology	AMS CMOS 180 nm
Chip dimensions	3.5×2 mm^2
Connection to the sensor and PCB	wire-bonding
Number of IO pads	77
Number of channels	32
Injection capacitor (HG)	10 fF
Injection capacitor (LG)	1 pF
Input signal (HG)*	electrons 3-40 ke^-
Input signal (LG)*	electrons 300-4000 ke^-
Optimized to sensor capacitance	4 pF
Sensor coupling	AC
Voltage gain (HG)	7.8 $\mu V/e^-$
Voltage gain (LG)	112.4 nV/e^-
Adjustable threshold (HG)	from -3.1 ke^- to 8.7 ke^-
Adjustable threshold (LG)	from -264 ke^- to 745 ke^-
Local threshold tuning range	±1.1 ke^- (HG), ±100 ke^-
ToT to electrons conversion factor (HG)	620 ns @ 10 ke^-, 2.36 μs @ 40 ke^-
ToT to electrons conversion factor (LG)	860 ns @ 1 Me^-, 2.55 μs @ 4 Me^-
Noise (HG)	1100 e^-
Noise (LG)	2.3 ke^-
Power supply voltage	1.8 V
Static power per channel (analog)	<150 μW
Dynamic power per channel	depends on setting ≈ 100 μW
Total expected power	<15 mW

Operating frequency - data in/out	10s MHz
Operating frequency - ToT (adjustable)	≈ 300 MHz (default)

Table A.1: Parameters of the integrated circuit PH32v6.

A.2 Global configuration

Bit number	functionality	Part	Default value	Description
143	VDISC_EN	analog	1	DAC enable
142	VHYST_EN	analog	1	DAC enable
141	VBP_EN	analog	1	DAC enable
140	VBN_EN	analog	1	DAC enable
139	VCASC_EN	analog	1	DAC enable
138	VTDAC_REF_EN	analog	1	DAC enable
137	VFDAC_REF_EN	analog	1	DAC enable
136	VFB_BASE_EN	analog	1	DAC enable
135	VBIAS_EN	analog	1	DAC enable
134	G1_LVDS_CM_Ref_EN	analog	1	SCL DAC enable
133	G2_LVDS_VBP_EN	analog	1	SCL DAC enable
132	G3_EN	analog	1	SCL DAC enable
131	G4_EN	analog	1	SCL DAC enable
130	Gpart9	digital	1	SCL
129	Gpart8	digital	1	SCL
128	unused			
127	clk_cnt_sel	digital	1	0 - clk_cnt_ext 1 - clk_cnt_int
126:125	clk_cnt_div	digital	0	00 - /1 01 - /2 10 - /4 11 - /8
124	clk_256_en	digital	0	Output enable
123	shift_en	digital	0	Shift enable
122:121	shift_div	digital	0	00 - clk_cnt/2048 01 - clk_cnt/4096 10 - clk_cnt/8192 11 - clk_cnt/16535
120	SHIFT_SEL	digital	0	0 - digital part 1 - scl part
119	SCL_TIME_EN	digital	0	Time measuring
118	hit_trigger_sel	digital	0	0 - hit_accept

				1 - hit_global
117	hit_trigger_en	digital	0	Output enable
116	SCL_CLK_CNT_EN	digital	0	Clk for SCL enable
115:112	DAC_OUT	analog	0	0000 - digital ground 0001 - VHYST 0010 - VBP 0011 - VBN 0100 - VCASC 0101 - VTDAC_REF 0110 - VFDAC_REF 0111 - VFDAC_BASE 1000 - VCO_BIAS 1001 - G1 1010 - G2 1011 - G3 1100 - G4 1101 - UGA_B 1110 - VDISC 1111 - digital power
111	Gpart7	digital	0	
110	Gpart6	digital	0	
109	Gpart5	digital	0	
108	Gpart4	digital	0	
117	Gpart3	digital	0	
106	Gpart2	digital	0	
105	Gpart1	digital	0	
104	Gpart0	digital	0	
103:96	G4	analog	0 V	1111 1111
95:88	G3	analog	0 V	1111 1111
87:80	lvds_range	analog	1.8 V	0000 0000
79:72	lvds_rising	analog	0 V	1111 1111
71:64	VBIAS	analog	900 mV/250 MHz	1000 0000
63:56	VFB_BASE	analog	1 V	0111 0001
55:48	VFDAC_REF	analog	900 mV	1000 0000
47:40	VTDAC_REF	analog	900 mV	1000 0000
39:32	VCASC	analog	800 mV	1000 1110
31:24	VBN	analog	500 mV	1011 1000
23:16	VBP	analog	750 mV	1001 0101
15:8	VHYSC	analog	1.8 V	0000 0000
7:0	VDISC	analog	550 mV	1011 0001

Table A.2: Global configuration bits of the PH32v6 chip.

A.3 Channel configuration

Bit number	Name	Part	Description
23	unused		
22	unused		
21	unused		
20	unused		
19	SENS_EN	analog	Connect sensor
18	accept_out	digital	Send information of accepted hit
17	hit_global_out	digital	Send information of presented hit
16	shutter_wait	digital	Wait for release hit_global to synchronizing shutter
15	out_en	analog	Analog output enable. Can be enabled ONLY IN ONE CHANNEL!!! (default value is therefore LOW)
14	gain	analog	HIGH gain = 0 (default) LOW gain = 1
13	inject_en	analog	Enable inject
12	FDAC[4]	analog	FDAC
11	FDAC[3]		
10	FDAC[2]		
9	FDAC[1]		
8	FDAC[0]		
7	channel_en	analog	Channel enable
6	mode_1	digital	Mode select
5	mode_0		
4	TDAC[4]	analog	TDAC
3	TDAC[3]		
2	TDAC[2]		
1	TDAC[1]		
0	TDAC[0]		

Table A.3: Channel configuration bits of the PH32v6 chip.

Appendix B

The simulation results of pseudo-random versus asynchronous counter

B.1 The simulation results of pseudo-random counter

The simulation of pseudo-random counter which can act as shift register as well with clock frequency 250 MHz is shown in Fig. B.1. The simulation is divided into two modes: *configuration* mode when the signal *shutter* is in a HIGH state and *counting* mode when the signal *shutter* is in a LOW state. The power consumption is very important just for *counting* mode since the *configuration* may run at lower frequency. The average power consumption for *configuration* is 140 uW and for *counting* mode is even slightly higher 170 uW.

B.2 The simulation results of asynchronous counter

The same simulation as in section B.1 but for 13-bit asynchronous counter (Note that 16-bit counter is used in the PH32v5 chip and its followers) which can act as shift register as well has been done (Fig. B.2).

From the simulation is visible that the power consumption is much lower than for pseudo-random counter. The average power consumption for *configuration* is 180 uW which is even higher in compare with pseudo-counter but for our requirement it is not relevant. For *counting* mode the power consumption is 60 uW what is almost one third of the power consumption of the pseudo-counter. This solution solved the issue with cross-talk between digital activity of counter and the output of CSA in the analog part of the chip and has been proven even for higher sampling frequencies.

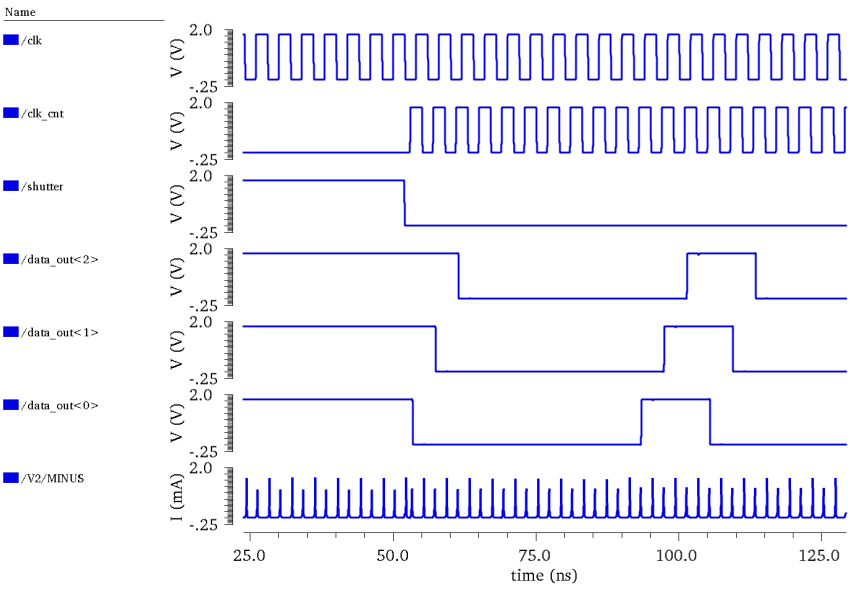

Figure B.1: The simulation of 13-bit pseudo-random counter register which can react as shift register as well with clock frequency 250 MHz. The average power consumption for *configuration* (shutter is in a HIGH state) is 140 uW and for *counting* mode (shutter is in a LOW state) is 170 uW.

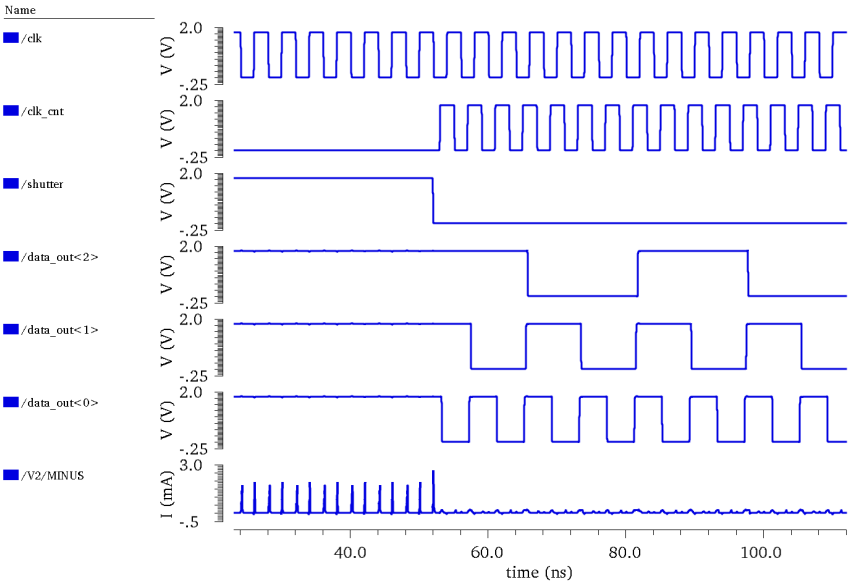

Figure B.2: The simulation of 13-bit asynchronous counter which can react as shift register as well with clock frequency 250 MHz. The average power consumption for *configuration* (shutter is in a HIGH state) is 180 uW and for *counting* mode (shutter is in a LOW state) is 60 uW.